MAGIC-TDAS 05-03
050321

Comparison of Signal Reconstruction Algorithms for the MAGIC Telescope

H. Bartko, M. Gaug, F. Goebel, A. Moralejo,
N. Sidro, W. Wittek

March 21^{st}, 2005

Abstract

Presently, the MAGIC telescope uses a 300 MHz FADC system to sample the transmitted and shaped signals from the captured Cherenkov light of air showers. In this note. different algorithms to reconstruct the signal from the read out samples are described and compared. Criteria for comparison are defined and used to judge the different extractors applied to calibration signals, cosmics and pedestals. At the end, extractors are recommended for the most conservative and the most advanced and demanding analyses. It is shown that the digital filter can be used to extract and fit single photo-electron pulses from the night sky background. The achievable time resolution has been derived as a function of the incident number of photo-electrons. For galactic backgrounds an image cleaning threshold as low as 5 photo-electrons can be achieved without using the timing information and for rejecting 99.7% of noise.

Contents

1 Introduction

The MAGIC telescope aims to study the gamma ray emission from high energy phenomena and the violent physics processes in the universe at the lowest energy threshold possible [1].

Figure 1 shows a sketch of the MAGIC read-out scheme, including the photomultiplier tubes (PMT) camera, the analog-optical link, the majority trigger logic and flash analog-to-digital converters (FADCs). The used PMTs provide a very fast response to the input light signal. The response of the PMTs to sub-ns input light pulses shows a FWHM of 1.0 - 1.2 ns and rise and fall times of 600 and 700 ps correspondingly [2]. By modulating vertical-cavity surface-emitting laser (VCSEL) type laser diodes in amplitude, the fast analog signals from the PMTs are transferred via 162 m long, 50/125 μm diameter optical fibers to the counting house [3]. After transforming the light back to an electrical signal, the original PMT pulse has a FWHM of about 2.2 ns and rise and fall times of about 1 ns.

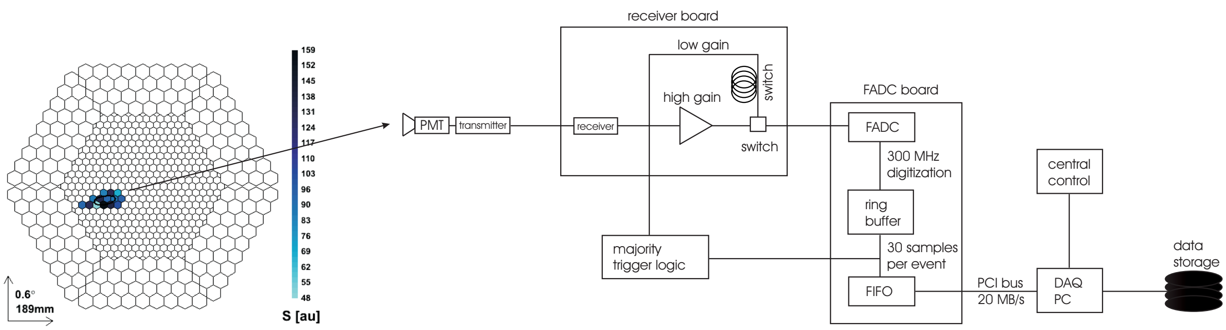

Figure 1: Current MAGIC read-out scheme: the analog PMT signals are transferred via an analog optical link to the counting house – where after the trigger decision – the signals are digitized by a 300 MHz FADCs system and written to the hard disk of a data acquisition PC.

In order to sample this pulse shape with the 300 MSamples/s FADC system, the original pulse is folded with a stretching function of 6ns leading to a FWHM greater than 6 ns. Because the MAGIC FADCs have a resolution of 8 bit only, the signals are split into two branches with gains differing by a factor 10. One branch is delayed by 55 ns and then both branches are multiplexed and consecutively read-out by one FADC. Figure 4 shows a typical average of identical signals. A more detailed overview about the MAGIC read-out and DAQ system is given in [4].

To reach the highest sensitivity and the lowest possible analysis energy threshold the recorded signals from Cherenkov light have to be accurately reconstructed. Therefore the highest possible signal to noise ratio, signal reconstruction resolution and a small bias are important.

Monte Carlo (MC) based simulations predict different time structures for gamma and hadron induced shower images as well as for images of single muons. An accurate arrival time determination may therefore improve the separation power of gamma events from the background events. Moreover, the timing information may be used in the image cleaning to discriminate between pixels which signal belongs to the shower and pixels which are affected by randomly timed background noise.

This note is structured as follows: In section 2 the average pulse shapes are reconstructed from the recorded FADC samples for calibration and cosmics pulses. These pulse shapes are compared with the pulse shape implemented in the MC simulation. In section 3 different signal reconstruction algorithms and their implementation in the common MAGIC software framework **MARS** are reviewed. In section 4 criteria for an optimal signal reconstruction are developed. Thereafter the signal extraction algorithms under study are applied to pedestal, calibration and MC events in sections 6 to 5. The CPU requirements of the different algorithms are compared in section 9. Finally in section 10 the results are summarized and in section 11 a standard signal extraction algorithm for MAGIC is proposed.

1.1 Characteristics of the current read-out system

The following intrinsic characteristics of the current read-out system affect especially the signal reconstruction:

Inner and Outer pixels: The MAGIC camera has two types of pixels which incorporate the following differences:

1. Size: The outer pixels have a factor four bigger area than the inner pixels [5]. Their (quantum-efficiency convoluted) effective area is about a factor 2.6 higher.
2. Gain: The camera is flat-fielded in order to yield a similar reconstructed charge signal for the same photon illumination intensity. In order to achieve this, the gain of the inner pixels has been adjusted to about a factor 2.6 higher than the outer ones [6]. This results in lower effective noise charge from the night sky background for the outer pixels.
3. Delay: The signal of the outer pixels is delayed by about 1.5 ns with respect to the inner ones.

Clock noise: The MAGIC 300 MHz FADCs have an intrinsic clock noise of a few least significant bits (LSBs) occurring with a frequency of 150 MHz. This clock noise results in a superimposed AB-pattern for the read-out pedestals. In the standard analysis, the amplitude of this clock noise gets measured in the pedestal extraction algorithms and further corrected for by all signal extractors.

Trigger Jitter: The FADC clock is not synchronized with the trigger. Therefore, the relative position of the recorded signal samples varies uniformly by one FADC slice with respect to the position of the signal shape by one FADC slice from event to event.

DAQ jumps: Unfortunately, the position of the signal pulse with respect to the first recorded FADC sample is not constant. It varies randomly by an integer number of FADC slices – typically two – in about 1% of the channels per event.

2 Pulse Shape Reconstruction

The FADC clock is not synchronized with the trigger. Therefore, the relative position of the recorded signal samples varies from event to event with respect to the position of the signal shape. The time Δt between the trigger decision and the first read-out sample is uniformly distributed in the range $t_{\text{rel}} \in [0, T_{\text{FADC}}[$, where $T_{\text{FADC}} = 3.33\,\text{ns}$ is the digitization period of the MAGIC 300 MHz FADCs. Δt can be determined using the reconstructed arrival time t_{arrival}.

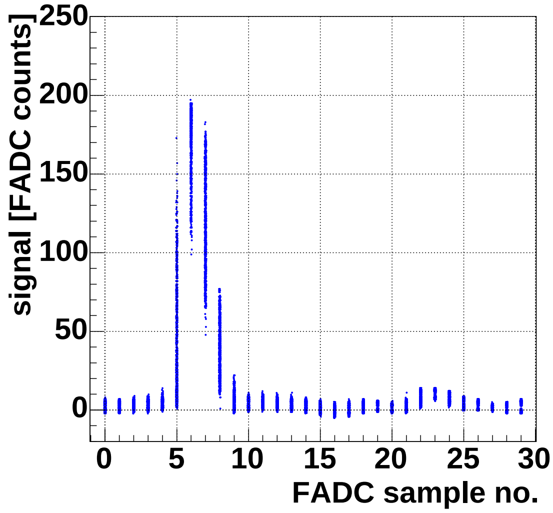

Figure 2: Raw FADC slices of 1000 constant pulse generator pulses overlayed.

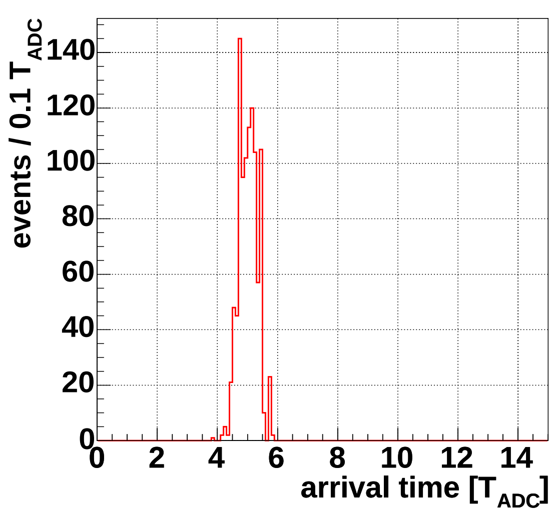

Figure 3: Distribution of the reconstructed time from the raw FADC samples shown in figure 2. The width of the distribution is due to the trigger jitter of 1 FADC period (3.33 ns).

Figure 2 shows the raw FADC values as a function of the slice number for 1000 constant pulse generator pulses overlayed. Figure 3 shows the distribution of the corresponding reconstructed pulse arrival times. The distribution has a width of about 1 FADC period (3.33 ns).

The asynchronous sampling of the pulse shape allows to determine an average pulse shape from the recorded signal samples: The recorded signal samples are shifted in time such that the shifted arrival times of all events are equal. In addition, the signal samples are normalized event by event using the reconstructed charge of the pulse. The accuracy of the signal shape reconstruction depends on the accuracy of the arrival time and charge reconstruction. The relative statistical error of the reconstructed pulse shape is well below 10^{-2} while the systematical error is by definition unknown at first hand.

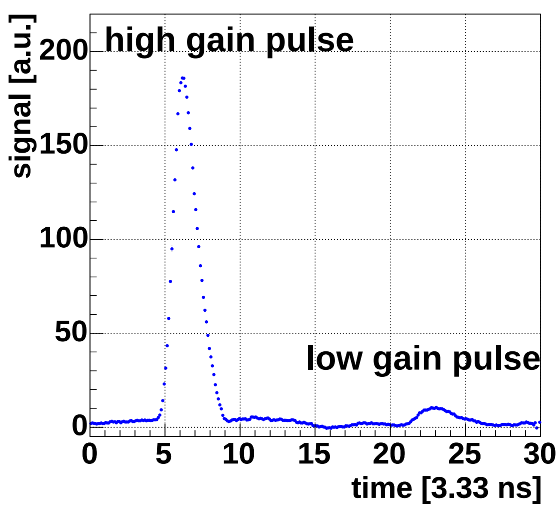

Figure 4: Average reconstructed pulse shape from a pulpo run showing the high-gain and the low gain pulse. The FWHM of the high gain pulse is about 6.3 ns while the FWHM of the low gain pulse is about 10 ns.

Figure 4 shows the averaged and shifted reconstructed signal of a fast pulser in the so called pulse generator ("pulpo") setup. Thereby the response of the photo-multipliers to Cherenkov light is simulated by a fast electrical pulse generator which generates unipolar pulses of about 2.5 ns FWHM and preset amplitude. These electrical pulses are transmitted using the same analog-optical link as the PMT pulses and are fed to the MAGIC receiver board. The pulse generator setup is mainly used for test purposes of the receiver board, trigger logic and FADCs.

In figure 4 the high and the low gain pulses are clearly visible. The low gain pulse is attenuated by a factor of about 10 and delayed by about 55 ns with respect to the high gain pulse.

Figure 5 (left) shows the averaged normalized (to an area of 1FADC count * $T_{FADC} = 3.33$ ns) reconstructed pulse shapes for the "pulpo" pulses in the high and in the low gain, respectively. The input FWHM of the pulse generator pulses is about 2 ns. The FWHM of the average reconstructed high gain pulse shape is about 6.3 ns, while the FWHM of the average reconstructed low gain pulse shape is about 10 ns. The pulse broadening of the low gain pulses with respect to the high gain pulses is due to the limited dynamic range of the passive 55 ns on board delay line of the MAGIC receiver boards. It has a FWHM of about 10 ns.

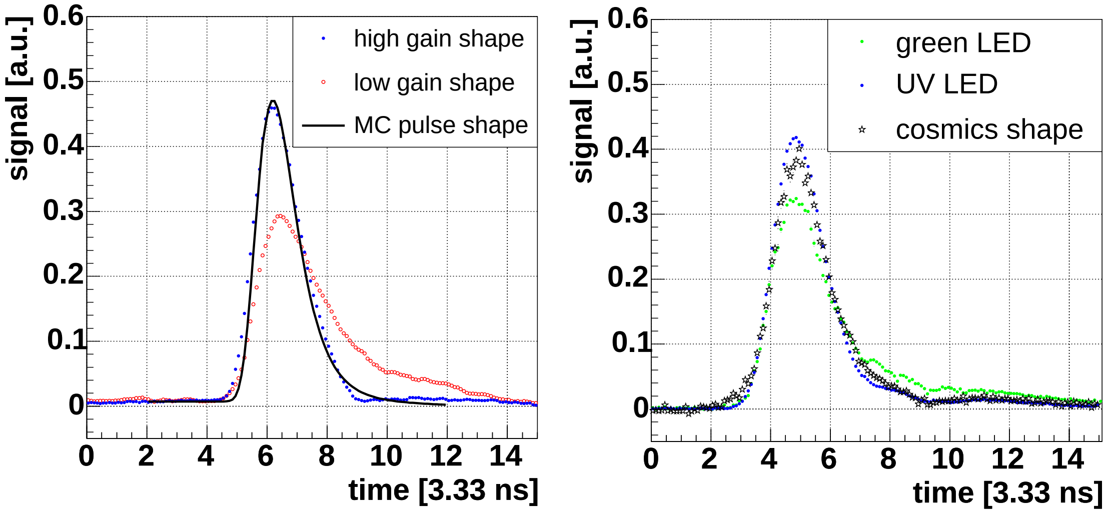

Figure 5: Left: Average normalized reconstructed high gain and low gain pulse shapes from a pulpo run. The FWHM of the low gain pulse is about 10 ns. The black line corresponds to the pulse shape implemented into the MC simulations [7]. Right: Average reconstructed high gain pulse shape for one green LED calibration run. The FWHM is about 6.5 ns.

Figure 5 (right) shows the normalized average reconstructed pulse shapes for green and UV calibration LED pulses [8] as well as the normalized average reconstructed pulse shape for cosmics events. The pulse shape of the UV calibration pulses is quite similar to the reconstructed pulse shape for cosmics events, both have a FWHM of about 6.3 ns. As air showers due to hadronic cosmic rays trigger the telescope much more frequently than gamma showers the reconstructed pulse shape of the cosmics events corresponds mainly to hadron induced showers. The pulse shape due to electromagnetic air showers might be slightly different as indicated by MC simulations [9]. The pulse shape for green calibration LED pulses is wider and has a pronounced tail.

3 Signal Reconstruction Algorithms

3.1 Implementation of Signal Extractors in MARS

We performed all studies presented in this note using and developing the common MAGIC software framework MARS [10].

All signal extractor classes are stored in the MARS-directory **msignal/**. There, the base classes **MExtractor**, **MExtractTime**, **MExtractTimeAndCharge** and all individual extractors can be found. Figure 6 gives a sketch of the inheritances and tasks of each class.

The following base classes for the extractor tasks are used:

MExtractor: This class provides the basic data members, equal for all extractors, which are:

1. Global extraction ranges, defined by the variables **fHiGainFirst, fHiGainLast, fLoGainFirst, fLoGainLast** and the function **SetRange()**. The ranges always **include** the edge slices.
2. An internal variable **fHiLoLast** regulating the overlap of the desired high-gain extraction range into the low-gain array.
3. The maximum possible FADC value, before the slice is declared as saturated, defined by the variable **fSaturationLimit** (default: 254).
4. The typical delay between high-gain and low-gain slices, expressed in FADC slices and parameterized by the variable **fOffsetLoGain** (default: 1.51)
5. Pointers to the storage containers **MRawEvtData, MRawRunHeader, MPedestalCam** and **MExtractedSignalCam**, defined by the variables **fRawEvt, fRunHeader, fPedestals** and **fSignals**.
6. Names of the storage containers to be searched for in the parameter list, parameterized by the variables **fNamePedestalCam** and **fNameSignalCam** (default: "MPedestalCam" and "MExtractedSignalCam").
7. The equivalent number of FADC samples, used for the calculation of the pedestal RMS and then the number of photo-electrons with the F-Factor method (see eq. 31 and section 8.2). This number is parameterized by the variables **fNumHiGainSamples** and **fNumLoGainSamples**.

MExtractor is able to loop over all events, if the **Process()**-function is not overwritten. It uses the following (virtual) functions, to be overwritten by the derived extractor class:

1. void **FindSignalHiGain**(Byte_t* firstused, Byte_t* logain, Float_t& sum, Byte_t& sat) const
2. void **FindSignalLoGain**(Byte_t* firstused, Float_t& sum, Byte_t& sat) const

where the pointers "firstused" point to the first used FADC slice declared by the extraction ranges, the pointer "logain" points to the beginning of the "low-gain" FADC slices array (to be used for pulses reaching into the low-gain array) and the variables "sum" and "sat" get filled with the extracted signal and the number of saturating FADC slices, respectively.

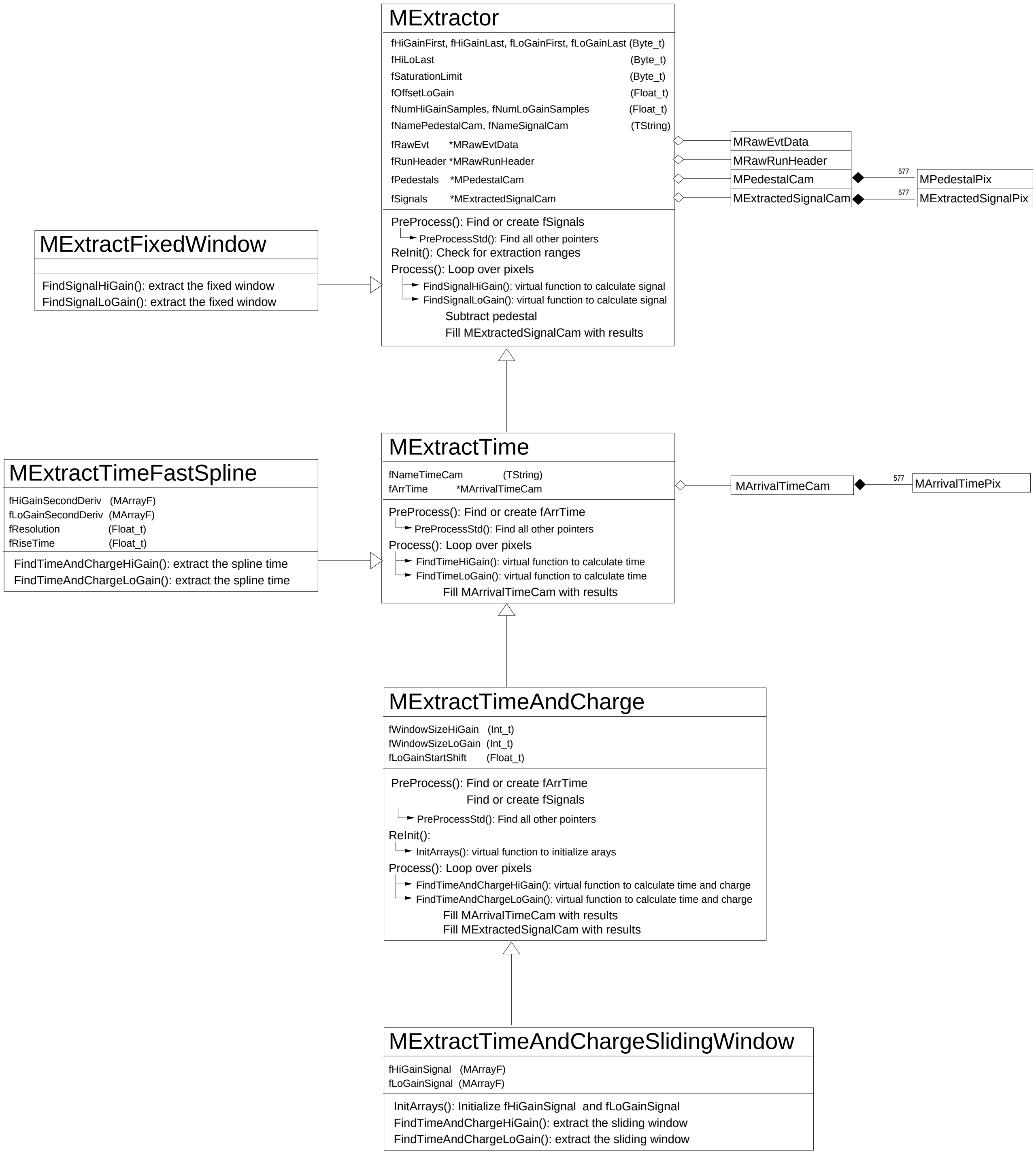

Figure 6: Sketch of the inheritances of three typical MARS signal extractor classes: MExtractFixed-Window, MExtractTimeFastSpline and MExtractTimeAndChargeDigitalFilter

The pedestals get subtracted automatically **after** execution of these two functions.

MExtractTime: This class provides - additionally to those already declared in **MExtractor** - the basic data members, equal for all time extractors, which are:

1. Pointer to the storage container **MArrivalTimeCam** parameterized by the variable **fArrTime**.
2. The name of the "MArrivalTimeCam"-container to be searched for in the parameter list, parameterized by the variables **fNameTimeCam** (default: "MArrivalTime-Cam").

MExtractTime is able to loop over all events, if the **Process()**-function is not overwritten. It uses the following (virtual) functions, to be overwritten by the derived extractor class:

1. void **FindTimeHiGain**(Byte_t* firstused, Float_t& time, Float_t& dtime, Byte_t& sat, const MPedestlPix &ped) const
2. void **FindTimeLoGain**(Byte_t* firstused, Float_t& time, Float_t& dtime, Byte_t& sat, const MPedestalPix &ped) const

where the pointers "firstused" point to the first used FADC slice declared by the extraction ranges, and the variables "time", "dtime" and "sat" get filled with the extracted arrival time, its error and the number of saturating FADC slices, respectively.

The pedestals can be used for the arrival time extraction via the reference "ped".

MExtractTimeAndCharge: This class provides - additionally to those already declared in **MExtractor** and **MExtractTime** - the basic data members, equal for all time and charge extractors, which are:

1. The actual extraction window sizes, parameterized by the variables **fWindowSize-HiGain** and **fWindowSizeLoGain**.
2. The shift of the low-gain extraction range start w.r.t. to the found high-gain arrival time, parameterized by the variable **fLoGainStartShift** (default: -2.8)

MExtractTimeAndCharge is able to loop over all events, if the **Process()**-function is not overwritten. It uses the following (virtual) functions, to be overwritten by the derived extractor class:

1. void **FindTimeAndChargeHiGain**(Byte_t* firstused, Byte_t* logain, Float_t& sum, Float_t& dsum, Float_t& time, Float_t& dtime, Byte_t& sat, const MPedestlPix &ped, const Bool_t abflag) const
2. void **FindTimeAndChargeLoGain**(Byte_t* firstused, Float_t& sum, Float_t& dsum, Float_t& time, Float_t& dtime, Byte_t& sat, const MPedestalPix &ped, const Bool_t abflag) const

where the pointers "firstused" point to the first used FADC slice declared by the extraction ranges, the pointer "logain" point to the beginning of the low-gain FADC slices array (to be used for pulses reaching into the "low-gain" array), the variables "sum", "dsum" get filled with the extracted signal and its error. The variables "time", "dtime" and "sat" get filled with the extracted arrival time, its error and the number of saturating FADC slices, respectively.

The pedestals can be used for the extraction via the reference "ped", also the "AB-flag" is given for clock noise correction.

3.2 Pure Signal Extractors

The pure signal extractors have in common that they reconstruct only the charge, but not the arrival time. All extractors treated here derive from the MARS-base class **MExtractor** which provides the following facilities:

- The global extraction limits can be set from outside
- FADC saturation is kept track of

The following adjustable parameters have to be set from outside:

Global extraction limits: Limits in between which the extractor is allowed to extract the signal, for high gain and low gain, respectively.

As the pulses jitter by about one FADC slice, not every pulse lies exactly within the optimal limits, especially if one chooses small extraction windows. Moreover, the readout position with respect to the trigger position has changed a couple of times during last year, therefore a very careful adjustment of the extraction limits is mandatory before using these extractors.

3.2.1 Fixed Window

This extractor is implemented in the MARS-class **MExtractFixedWindow**. It simply adds the FADC slice contents in the assigned ranges. As it does not correct for the clock-noise, only an even number of samples is allowed. Figure 7 gives a sketch of the extraction ranges used in this paper and for two typical calibration pulses.

3.2.2 Fixed Window with Integrated Cubic Spline

This extractor is implemented in the MARS-class **MExtractFixedWindowSpline**. It uses a cubic spline algorithm, adapted from [11] and integrates the spline interpolated FADC slice values from a fixed extraction range. The edge slices are counted as half. As it does not correct for the clock-noise, only an odd number of samples is allowed. Figure 8 gives a sketch of the extraction ranges used in this paper and for typical calibration pulses.

3.2.3 Fixed Window with Global Peak Search

This extractor is implemented in the MARS-class **MExtractFixedWindowPeakSearch**. The basic idea of this extractor is to correct for coherent movements in arrival time for all

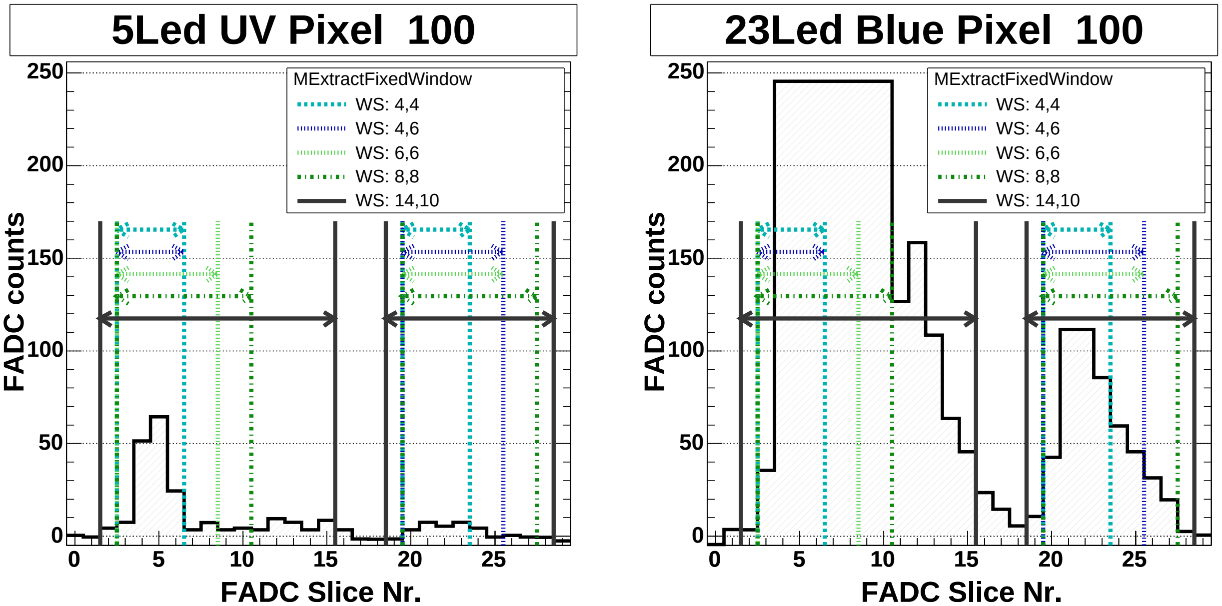

Figure 7: Sketch of the extraction ranges for the extractor **MExtractFixedWindow** *for two typical calibration pulses (pedestals have been subtracted) and a typical inner pixel. The pulse would be shifted half a slice to the right for an outer pixel.*

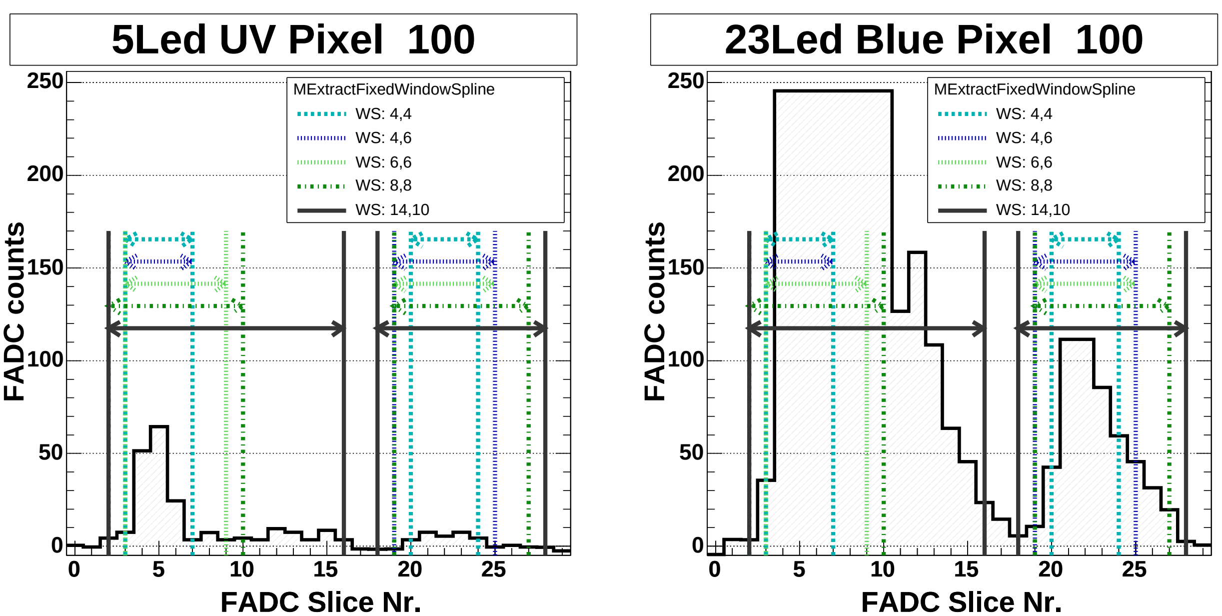

Figure 8: Sketch of the extraction ranges for the extractor **MExtractFixedWindowSpline** *for two typical calibration pulses (pedestals have been subtracted) and a typical inner pixel. The pulse would be shifted half a slice to the right for an outer pixel.*

pixels, as e.g. caused by the trigger jitter. In a first loop over the pixels, it determined a reference point slices number defined by the highest sum of consecutive non-saturating FADC slices in a (smaller) peak-search window.

In a second loop over the pixels, it adds the contents of the FADC slices starting from the reference point over an extraction window of a pre-defined window size. It loops twice over all pixels in every event, because it has to find the reference point, first. As it does not correct for the clock-noise, only extraction windows with an even number of samples are allowed. For a high intensity calibration run causing high-gain saturation in the whole camera, this extractor apparently fails since only dead pixels are taken into account in the peak search which cannot produce a saturated signal. For this special case, we modified **MExtractFixedWindowPeak-Search** such to define the peak search window as the one starting from the mean position of the first saturating slice.

The following adjustable parameters have to be set from outside:

Peak Search Window: Defines the "sliding window" size within which the peaking sum is searched for (default: 4 slices)

Offset from Window: Defines the offset of the start of the extraction window w.r.t. the starting point of the obtained peak search window (default: 1 slice)

Low-Gain Peak shift: Defines the shift in the low-gain with respect to the peak found in the high-gain (default: 1 slice)

Figure 9 gives a sketch of the possible peak-search and extraction window positions in two typical calibration pulses.

3.3 Combined Extractors

The combined extractors have in common that for a given pulse, they reconstruct both the arrival time and the charge. All combined extractors described here derive from the MARS-base class **MExtractTimeAndCharge** which itself derives from MExtractor and MExtractTime. It provides the following facilities:

- Only one loop over all pixels is performed.
- The individual FADC slice values get the clock-noise-corrected pedestals immediately subtracted.
- The low-gain extraction range is adapted dynamically, based on the arrival time computed from the high-gain samples.
- Arrival times extracted from the low-gain samples get corrected for the intrinsic time delay of the low-gain pulse.
- The global extraction limits can be set from outside.
- FADC saturation is kept track of.

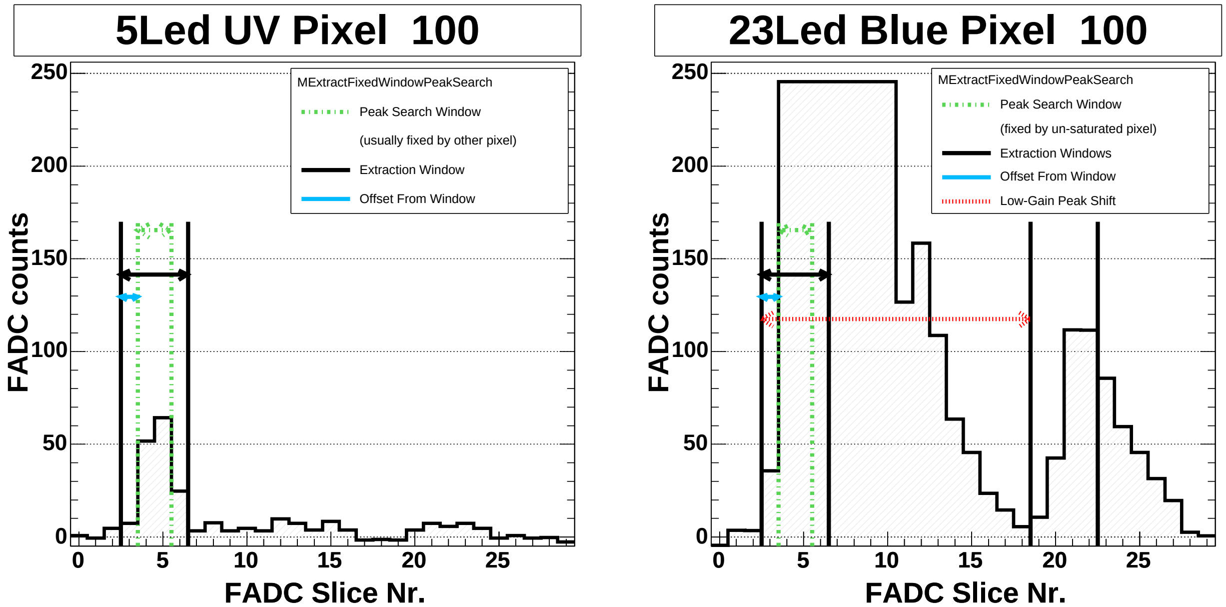

Figure 9: Sketch of the extraction ranges for the extractor **MExtractFixedWindowPeakSearch** *for two typical calibration pulses (pedestals have been subtracted) and a typical inner pixel. The pulse would be shifted half a slice to the right for an outer pixel.*

The following adjustable parameters have to be set from outside, additionally to those declared in the base classes MExtractor and MExtractTime:

Global extraction limits: Limits in between which the extractor is allowed to search. They are fixed by the extractor for the high-gain, but re-adjusted for every event in the low-gain, depending on the arrival time found in the low-gain. However, the dynamically adjusted window is not allowed to pass beyond the global limits.

Low-gain start shift: Global shift between the computed high-gain arrival time and the start of the low-gain extraction limit (corrected for the intrinsic time offset). This variable tells where the extractor is allowed to start searching for the low-gain signal if the high-gain arrival time is known. It avoids that the extractor gets confused by possible high-gain signals leaking into the "low-gain" region (default: -2.8).

3.3.1 Sliding Window with Amplitude-Weighted Time

This extractor is implemented in the MARS-class **MExtractTimeAndChargeSlidingWindow**. It extracts the signal from a sliding window of an adjustable size, for high-gain and low-gain individually (default: 6 and 6). The signal is the one which maximizes the summed (clock-noise and pedestal-corrected) consecutive FADC slice contents.

The amplitude-weighted arrival time is calculated from the window with the highest FADC slice contents integral using the following formula:

$$t = \frac{\sum_{i=i_0}^{i_0+ws-1} s_i \cdot i}{\sum_{i=i_0}^{i_0+ws-1} i} \tag{1}$$

where i denotes the FADC slice index, starting from slice i_0 and running over a window of size ws. s_i the clock-noise and pedestal-corrected FADC slice contents at slice position i.
The following adjustable parameters have to be set from outside:

Window sizes: Independently for high-gain and low-gain (default: 6,6)

Figure 10 gives a sketch of the reconstructed arrival time of the possible extraction window positions in two typical calibration pulses.

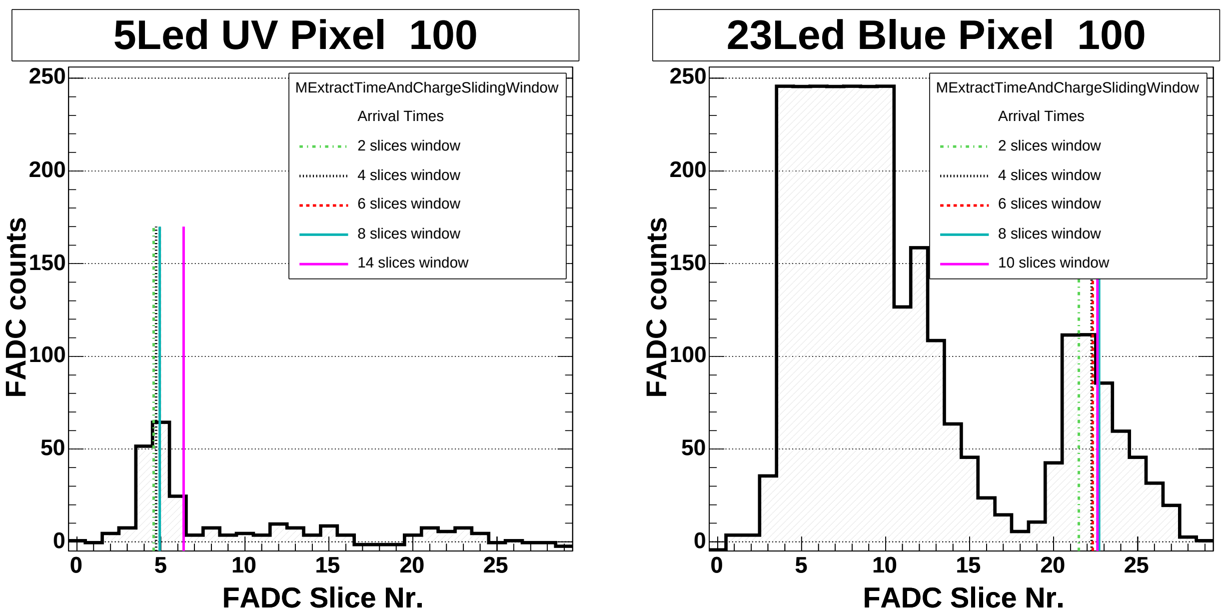

Figure 10: Sketch of the calculated arrival times for the extractor **MExtractTimeAndChargeSlidingWindow** *for two typical calibration pulses (pedestals have been subtracted) and a typical inner pixel. The extraction window sizes modify the position of the (amplitude-weighted) mean FADC-slices slightly. The pulse would be shifted half a slice to the right for an outer pixel.*

3.3.2 Cubic Spline with Sliding Window or Amplitude Extraction

This extractor is implemented in the MARS-class **MExtractTimeAndChargeSpline**. It interpolates the FADC contents using a cubic spline algorithm, adapted from [11]. In a second step, it searches for the position of the spline maximum. From then on, two possibilities are offered:

Extraction Type Amplitude: The amplitude of the spline maximum is taken as charge signal and the (precise) position of the maximum is returned as arrival time. This type is faster, since a spline integration is not performed.

Extraction Type Integral: The integrated spline between maximum position minus rise time (default: 1.5 slices) and maximum position plus fall time (default: 4.5 slices) is taken as charge signal and the position of the half maximum left from the position of the maximum is returned as arrival time (default). The low-gain signal stretches the rise and fall time by a stretch factor (default: 1.5). This type is slower, but yields more precise results (see section **??**) . The charge integration resolution is set to 0.1 FADC slices.

The following adjustable parameters have to be set from outside:

Charge Extraction Type: The amplitude of the spline maximum can be chosen while the position of the maximum is returned as arrival time. This type is fast.
Otherwise, the integrated spline between maximum position minus rise time (default: 1.5 slices) and maximum position plus fall time (default: 4.5 slices) is taken as signal and the position of the half maximum is returned as arrival time (default). The low-gain signal stretches the rise and fall time by a stretch factor (default: 1.5). This type is slower, but more precise. The charge integration resolution is 0.1 FADC slices.

Rise Time and Fall Time: Can be adjusted for the integration charge extraction type.

Resolution: Defined as the maximum allowed difference between the calculated half maximum value and the computed spline value at the arrival time position. Can be adjusted for the half-maximum time extraction type.

Low Gain Stretch: Can be adjusted to account for the larger rise and fall times in the low-gain as compared to the high gain pulses (default: 1.5)

Figure 11 gives a sketch of the reconstructed arrival time for possible extraction window positions in two typical calibration pulses.

3.3.3 Digital Filter

This extractor is implemented in the MARS-class **MExtractTimeAndChargeDigitalFilter**.

The goal of the digital filtering method [12, 13] is to optimally reconstruct the amplitude and time origin of a signal with a known signal shape from discrete measurements of the signal. Thereby, the noise contribution to the amplitude reconstruction is minimized.

For the digital filtering method, three assumptions have to be made:

- The normalized signal shape has to be always constant, especially independent of the signal amplitude and in time.
- The noise properties have to be independent of the signal amplitude.
- The noise auto-correlation matrix does not change its form significantly with time and operation conditions.

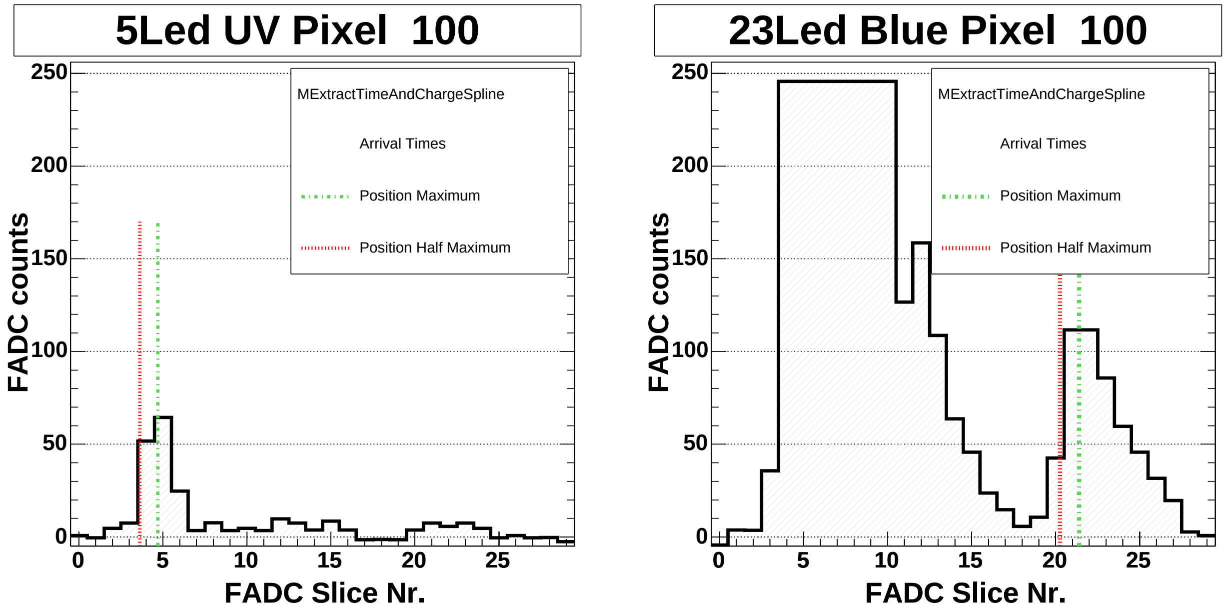

Figure 11: Sketch of the calculated arrival times for the extractor **MExtractTimeAndChargeSpline** *for two typical calibration pulses (pedestals have been subtracted) and a typical inner pixel. The extraction window sizes modify the position of the (amplitude-weighted) mean FADC-slices slightly. The pulse would be shifted half a slice to the right for an outer pixel.*

The pulse shape is mainly determined by the artificial pulse stretching by about 6 ns on the receiver board. Thus the first assumption holds to a good approximation for all pulses with intrinsic signal widths much smaller than the shaping constant. Also the second assumption is fulfilled: Signal and noise are independent and the measured pulse is the linear superposition of the signal and noise. The validity of the third assumption is discussed below, especially for different night sky background conditions.

Let $g(t)$ be the normalized signal shape, E the signal amplitude and τ the time shift of the physical signal from the predicted signal shape. Then the time dependence of the signal, $y(t)$, is given by:

$$y(t) = E \cdot g(t-\tau) + b(t) \ , \tag{2}$$

where $b(t)$ is the time-dependent noise contribution. For small time shifts τ (usually smaller than one FADC slice width), the time dependence can be linearized:

$$y(t) = E \cdot g(t) - E\tau \cdot \dot{g}(t) + b(t) \ , \tag{3}$$

where $\dot{g}(t)$ is the time derivative of the signal shape. Discrete measurements y_i of the signal at times t_i $(i = 1, ..., n)$ have the form:

$$y_i = E \cdot g_i - E\tau \cdot \dot{g}_i + b_i \ . \tag{4}$$

The correlation of the noise contributions at times t_i and t_j can be expressed in the noise autocorrelation matrix $\boldsymbol{B}$:

$$B_{ij} = \langle b_i b_j \rangle - \langle b_i \rangle \langle b_j \rangle \ . \tag{5}$$

The signal amplitude E, and the product $E\tau$ of amplitude and time shift, can be estimated from the given set of measurements $\boldsymbol{y} = (y_1, ..., y_n)$ by minimizing the deviation of the measured FADC slice contents from the known pulse shape with respect to the known noise autocorrelation:

$$\begin{aligned}
\chi^2(E, E\tau) &= \sum_{i,j} (y_i - E g_i - E\tau \dot{g}_i)(\boldsymbol{B}^{-1})_{ij}(y_j - E g_j - E\tau \dot{g}_j) && (6)\\
&= (\boldsymbol{y} - E\boldsymbol{g} - E\tau\dot{\boldsymbol{g}})^T \boldsymbol{B}^{-1}(\boldsymbol{y} - E\boldsymbol{g} - E\tau\dot{\boldsymbol{g}}) \ , && (7)
\end{aligned}$$

where the last expression uses the matrix formalism. χ^2 is a continuous function of τ and will have to be discretized itself for numerical computation applications. χ^2 is in principle independent of the noise level if always the appropriate noise autocorrelation matrix is used. In our case however, we decided to use one matrix $\boldsymbol{B}$ for all levels of night-sky background. Changes in the noise level lead only to a multiplicative factor for all matrix elements and thus do not affect the position of the minimum of χ^2. The minimum of χ^2 is obtained for:

$$\frac{\partial \chi^2(E, E\tau)}{\partial E} = 0 \qquad \text{and} \qquad \frac{\partial \chi^2(E, E\tau)}{\partial (E\tau)} = 0 \ . \tag{8}$$

Taking into account that $\boldsymbol{B}$ is a symmetric matrix, this leads to the following two equations for the estimated amplitude $\overline{E}$ and the estimation for the product of amplitude and time offset $\overline{E\tau}$:

$$\begin{aligned}
0 &= -\boldsymbol{g}^T\boldsymbol{B}^{-1}\boldsymbol{y} + \boldsymbol{g}^T\boldsymbol{B}^{-1}\boldsymbol{g}\overline{E} + \boldsymbol{g}^T\boldsymbol{B}^{-1}\dot{\boldsymbol{g}}\overline{E\tau} && (9)\\
0 &= -\dot{\boldsymbol{g}}^T\boldsymbol{B}^{-1}\boldsymbol{y} + \dot{\boldsymbol{g}}^T\boldsymbol{B}^{-1}\boldsymbol{g}\overline{E} + \dot{\boldsymbol{g}}^T\boldsymbol{B}^{-1}\dot{\boldsymbol{g}}\overline{E\tau} \ . && (10)
\end{aligned}$$

Solving these equations one gets the following solutions:

$$\overline{E}(\tau) = \boldsymbol{w}_{\text{amp}}^T(\tau)\boldsymbol{y} \quad \text{with} \quad \boldsymbol{w}_{\text{amp}} = \frac{(\dot{\boldsymbol{g}}^T\boldsymbol{B}^{-1}\dot{\boldsymbol{g}})\boldsymbol{B}^{-1}\boldsymbol{g} - (\boldsymbol{g}^T\boldsymbol{B}^{-1}\dot{\boldsymbol{g}})\boldsymbol{B}^{-1}\dot{\boldsymbol{g}}}{(\boldsymbol{g}^T\boldsymbol{B}^{-1}\boldsymbol{g})(\dot{\boldsymbol{g}}^T\boldsymbol{B}^{-1}\dot{\boldsymbol{g}}) - (\dot{\boldsymbol{g}}^T\boldsymbol{B}^{-1}\boldsymbol{g})^2} \ , \tag{11}$$

$$\overline{E\tau}(\tau) = \boldsymbol{w}_{\text{time}}^T(\tau)\boldsymbol{y} \quad \text{with} \quad \boldsymbol{w}_{\text{time}} = \frac{(\boldsymbol{g}^T\boldsymbol{B}^{-1}\boldsymbol{g})\boldsymbol{B}^{-1}\dot{\boldsymbol{g}} - (\boldsymbol{g}^T\boldsymbol{B}^{-1}\dot{\boldsymbol{g}})\boldsymbol{B}^{-1}\boldsymbol{g}}{(\boldsymbol{g}^T\boldsymbol{B}^{-1}\boldsymbol{g})(\dot{\boldsymbol{g}}^T\boldsymbol{B}^{-1}\dot{\boldsymbol{g}}) - (\dot{\boldsymbol{g}}^T\boldsymbol{B}^{-1}\boldsymbol{g})^2} \ . \tag{12}$$

Thus $\overline{E}$ and $\overline{E\tau}$ are given by a weighted sum of the discrete measurements y_i with the weights for the amplitude, $w_{\mathrm{amp}}(\tau)$, and time shift, $w_{\mathrm{time}}(\tau)$.

The time dependence gets discretized once again leading to a set of weight samples which themselves depend on the discretized time τ.

Note the remaining time dependency of the two weight samples. This follows from the dependence of $\boldsymbol{g}$ and $\dot{\boldsymbol{g}}$ on the relative position of the signal pulse with respect to FADC slices positions.

Because of the truncation of the Taylor series in equation (3) the above results are only valid for vanishing time offsets τ. For larger time offsets, one has to iterate the problem using the time shifted signal shape $g(t-\tau)$.

The covariance matrix $\boldsymbol{V}$ of $\overline{E}$ and $\overline{E\tau}$ is given by:

$$\left(\boldsymbol{V}^{-1}\right)_{ij} = \frac{1}{2}\left(\frac{\partial^2\chi^2(E,E\tau)}{\partial\alpha_i\partial\alpha_j}\right) \quad \text{with} \quad \alpha_i,\alpha_j \in \{E, E\tau\} \ . \tag{13}$$

The expected contribution of the noise to the estimated amplitude, σ_E, is:

$$\sigma_E^2 = \boldsymbol{V}_{E,E} = \frac{\dot{\boldsymbol{g}}^T\boldsymbol{B}^{-1}\dot{\boldsymbol{g}}}{(\boldsymbol{g}^T\boldsymbol{B}^{-1}\boldsymbol{g})(\dot{\boldsymbol{g}}^T\boldsymbol{B}^{-1}\dot{\boldsymbol{g}}) - (\dot{\boldsymbol{g}}^T\boldsymbol{B}^{-1}\boldsymbol{g})^2} \ . \tag{14}$$

The expected contribution of the noise to the estimated timing, σ_τ, is:

$$E^2 \cdot \sigma_\tau^2 < \sigma_{E\tau}^2 = \boldsymbol{V}_{E\tau,E\tau} = \frac{\boldsymbol{g}^T\boldsymbol{B}^{-1}\boldsymbol{g}}{(\boldsymbol{g}^T\boldsymbol{B}^{-1}\boldsymbol{g})(\dot{\boldsymbol{g}}^T\boldsymbol{B}^{-1}\dot{\boldsymbol{g}}) - (\dot{\boldsymbol{g}}^T\boldsymbol{B}^{-1}\boldsymbol{g})^2} \ . \tag{15}$$

Both equations 14 and 15 are independent of the signal amplitude.

In the MAGIC MC simulations [7], a night-sky background rate of 0.13 photoelectrons per ns, an FADC gain of 7.8 FADC counts per photo-electron and an intrinsic FADC noise of 1.3 FADC counts per FADC slice is implemented. These numbers simulate the night sky background conditions for an extragalactic source and result in a noise contribution of about 4 FADC counts per single FADC slice: $\sqrt{B_{ii}} \approx 4$ FADC counts. Using the digital filter with weights determined for 6 FADC slices ($i = 0...5$) the errors of the reconstructed signal and time amount to:

$$\sigma_E \approx 8.3 \text{ FADC counts } (\approx 1.1\,\text{phe}) \qquad \sigma_\tau \approx \frac{6.5\ \Delta T_{\mathrm{FADC}}}{(E\ /\ \text{FADC counts})}\ (\approx \frac{2.8\,\text{ns}}{E\ /\ \mathrm{N_{phe}}})\ , \tag{16}$$

where $\Delta T_{\mathrm{FADC}} = 3.33$ ns is the sampling interval of the MAGIC FADCs. The error in the reconstructed signal corresponds to about one photo electron. For signals of the size of two photo electrons, the timing error is about 1.4 ns.

An IACT has typically two types of background noise: On the one hand, there is the constantly present electronics noise, while on the other hand, the light of the night sky introduces a sizeable background to the measurement of the Cherenkov photons from air showers.

The electronics noise is largely white, i.e. uncorrelated in time. The noise from the night sky background photons is the superposition of the detector response to single photo electrons following a Poisson distribution in time. Figure 12 shows the noise autocorrelation matrix for an open camera. The large noise autocorrelation of the current FADC system is due to the pulse shaping (with the shaping constant equivalent to about two FADC slices).

In general, the amplitude and time weights, $\boldsymbol{w}_{\mathrm{amp}}$ and $\boldsymbol{w}_{\mathrm{time}}$, depend on the pulse shape, the derivative of the pulse shape and the noise autocorrelation. In the high gain samples, the correlated night sky background noise dominates over the white electronics noise. As a consequence, different noise levels cause the elements of the noise autocorrelation matrix to change by the same factor, which cancels out in the weights calculation. Figure 12 shows the noise autocorrelation matrix for two different levels of night sky background (top) and the ratio between the corresponding elements of both (bottom). The central regions of ± 3 FADC slices around the diagonal (which is used to calculate the weights) deviate by less than 10%. Thus, the weights are to a reasonable approximation independent of the night sky background noise level in the high gain.

In the low gain samples the correlated noise of the LONS is in the same order of magnitude as the white electronics and digitization noise. Moreover, the noise autocorrelation for the low gain samples cannot be determined directly from the data. The low gain is only switched on if the pulse exceeds a preset threshold. There are no pedestals in the low gain available. Thus the noise auto-correlation determined from MC simulations for an extragalactic background is also used to compute the weights for cosmics and calibration pulses.

Using the average reconstructed pulpo pulse shapes, as shown in figure 5, and the reconstructed noise autocorrelation matrices from pedestal runs with random triggers, the digital filter weights are computed. As the pulse shapes in the high and low gain and for cosmics, calibration and pulpo events are somewhat different, dedicated digital filter weights are computed for these event classes. Also filter weights optimized for MC simulations are calculated. High/low gain filter weights are computed for the following event classes:

1. cosmics weights: for cosmics events
2. calibration weights UV: for UV calibration pulses
3. calibration weights blue: for blue and green calibration pulses
4. MC weights: for MC simulations
5. pulpo weights: for pulpo runs.

Figures 13 and 14 show the amplitude and timing weights for the MC pulse shape. The first weight $w_{\mathrm{amp/time}}(t_0)$ is plotted as a function of the relative time t_{rel} between the trigger and the FADC clock in the range $[-0.5, 0.5[\ T_{\mathrm{ADC}}$, the second weight in the range $[0.5, 1.5[\ T_{\mathrm{ADC}}$ and so on. A binning resolution of $0.1\,T_{\mathrm{ADC}}$ has been chosen.

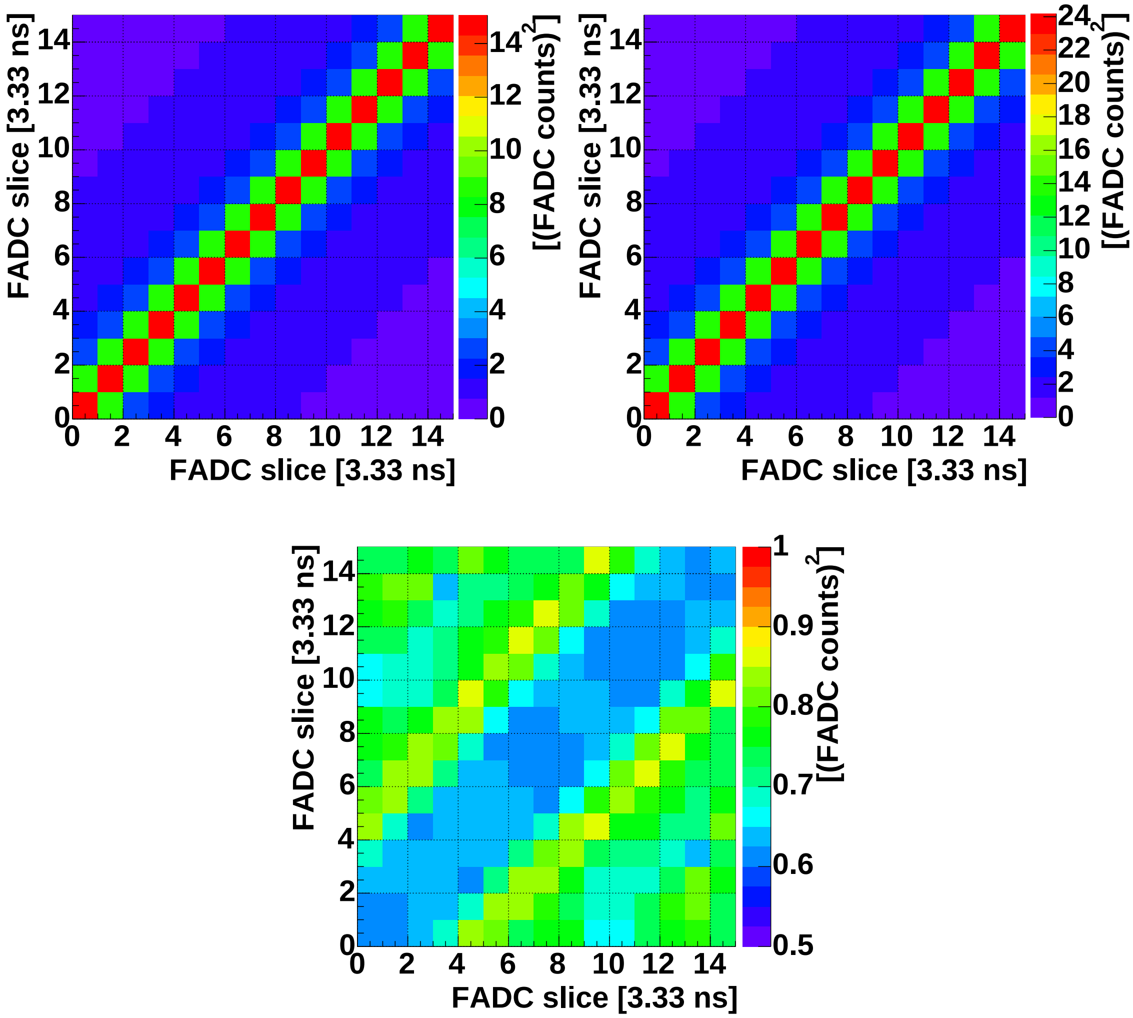

*Figure 12: Noise autocorrelation matrix **B** for open camera and averaged over all pixels. The top figure shows **B** obtained with camera pointing off the galactic plane (and low night sky background fluctuations). The central figure shows **B** with the camera pointing into the galactic plane (high night sky background) and the bottom plot shows the ratio between both. One can see that the entries of **B** do not simply scale with the amount of night sky background.*

	high gain shape	high gain noise	low gain shape	low gain noise
cosmics	25945 (pulpo)	38995 (extragal.)	44461 (pulpo)	MC low
UV	36040 (UV)	38995 (extragal.)	44461 (pulpo)	MC low
blue	31762 (blue)	38995 (extragal.)	31742 (blue)	MC low
MC	MC	MC high	MC	MC low
pulpo	25945 (pulpo)	38993 (no LONS)	44461 (pulpo)	MC low

Table 1: The used runs for the pulse shapes and noise auto-correlations for the digital filter weights of the different event types.

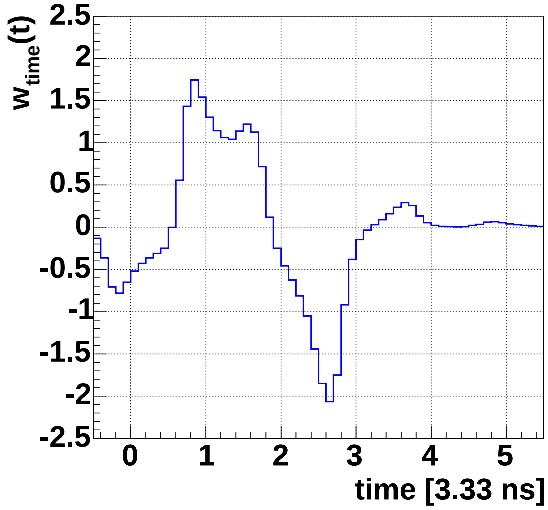

Figure 13: Time weights $w_{\mathrm{time}}(t_0)\dots w_{\mathrm{time}}(t_5)$ for a window size of 6 FADC slices for the pulse shape used in the MC simulations. The first weight $w_{\mathrm{time}}(t_0)$ is plotted as a function of the relative time t_{rel} the trigger and the FADC clock in the range $[-0.5, 0.5[\ T_{ADC}$, the second weight in the range $[0.5, 1.5[\ T_{ADC}$ and so on. A binning resolution of $0.1\,T_{ADC}$ has been chosen.

In the current implementation a two step procedure is applied to reconstruct the signal. The weight functions $w_{\mathrm{amp}}(t)$ and $w_{\mathrm{time}}(t)$ are computed numerically with a resolution of 1/10 of an FADC slice. In the first step the quantities e_{i_0} and $(e\tau)_{i_0}$ are computed using a window of n slices:

$$e_{i_0} = \sum_{i=i_0}^{i_0+n-1} w_{\mathrm{amp}}(t_i)y(t_{i+i_0}) \qquad (e\tau)_{i_0} = \sum_{i=i_0}^{i_0+n-1} w_{\mathrm{time}}(t_i)y(t_{i+i_0}) \tag{17}$$

for all possible signal start slices i_0. Let i_0^* be the signal start slice yielding the largest e_{i_0}. Then in a second step the timing offset τ is calculated:

$$\tau = \frac{(e\tau)_{i_0^*}}{e_{i_0^*}} \tag{18}$$

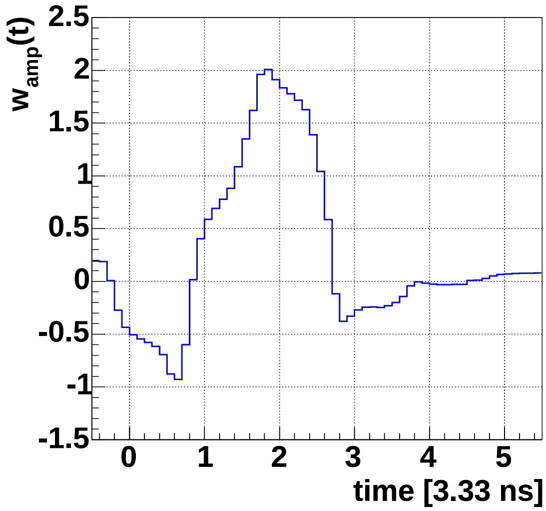

Figure 14: Amplitude weights $w_{\mathrm{amp}}(t_0)\ldots w_{\mathrm{amp}}(t_5)$ for a window size of 6 FADC slices for the pulse shape used in the MC simulations. The first weight $w_{\mathrm{amp}}(t_0)$ is plotted as a function of the relative time t_{rel} the trigger and the FADC clock in the range $[-0.5, 0.5[$ T_{ADC}, the second weight in the range $[0.5, 1.5[$ T_{ADC} and so on. A binning resolution of $0.1\,T_{ADC}$ has been chosen.

Using this value of τ, another iteration is performed:

$$E = \sum_{i=i_0^*}^{i_0^*+n-1} w_{\mathrm{amp}}(t_i - \tau) y(t_{i+i_0^*}) \qquad E\theta = \sum_{i=i_0^*}^{i_0^*+n-1} w_{\mathrm{time}}(t_i - \tau) y(t_{i+i_0^*}) \ . \tag{19}$$

The reconstructed signal is then taken to be E and the reconstructed arrival time t_{arrival} is

$$t_{\mathrm{arrival}} = i_0^* + \tau + \theta \ . \tag{20}$$

Figure 15 shows the result of the applied amplitude and time weights to the recorded FADC time slices of one simulated MC pulse. The left plot displays the result of the applied amplitude weights $e(t_0) = \sum_{i=0}^{i=n-1} w_{\mathrm{amp}}(t_0 + i \cdot T_{\mathrm{ADC}}) y(t_0 + i \cdot T_{\mathrm{ADC}})$ and the right plot shows the result of the applied timing weights $e\tau(t_0) = \sum_{i=0}^{i=n-1} w_{\mathrm{time}}(t_0 + i \cdot T_{\mathrm{ADC}}) y(t_0 + i \cdot T_{\mathrm{ADC}})$ as a function of the time shift t_0.

Figure 16 shows the signal pulse shape of a typical MC event together with the simulated FADC slices of the signal pulse plus noise. The digital filter has been applied to reconstruct the signal size and timing. Using this information together with the average normalized MC pulse shape the simulated signal pulse shape is reconstructed and shown as well.

The following free adjustable parameters have to be set from outside:

Weights File: An ascii-file containing the weights, the binning resolution and the window size. Currently, the following weight files have been created:

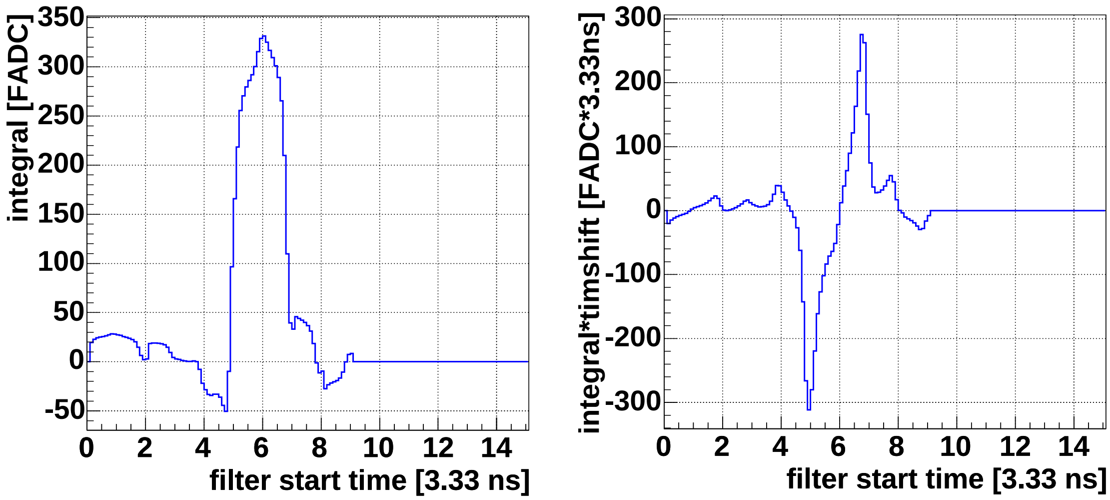

Figure 15: Digital filter weights applied to the recorded FADC time slices of one simulated MC pulse. The left plot shows the result of the applied amplitude weights $e(t_0) = \sum_{i=0}^{i=n-1} w_{\mathrm{amp}}(t_0+i\cdot T_{ADC})y(t_0+i\cdot T_{ADC})$ and the right plot displays the result of the applied timing weights $e\tau(t_0) = \sum_{i=0}^{i=n-1} w_{\mathrm{time}}(t_0+i\cdot T_{ADC})y(t_0+i\cdot T_{ADC})$ as a function of the time shift t_0.

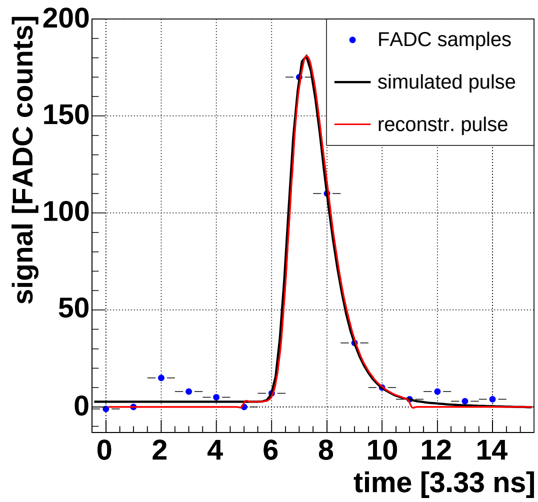

Figure 16: Simulated signal pulse shape and FADC slices for a typical MC event. The FADC measurements are affected by noise. Using the digital filter and the average MC pulse shape the signal shape is reconstructed. The event shown is the same as in figure 15.

- "cosmics_weights.dat" with a window size of 6 FADC slices
- "cosmics_weights4.dat" with a window size of 4 FADC slices
- "calibration_weights_blue.dat" with a window size of 6 FADC slices
- "calibration_weights4_blue.dat" with a window size of 4 FADC slices

- "calibration_weights_UV.dat" with a window size of 6 FADC slices and in the low-gain the calibration weights obtained from blue pulses[1].
- "calibration_weights4_UV.dat" with a window size of 4 FADC slices and in the low-gain the calibration weights obtained from blue pulses[2].

Figure 17 gives a sketch of the reconstructed arrival time of the possible extraction window positions in two typical calibration pulses.

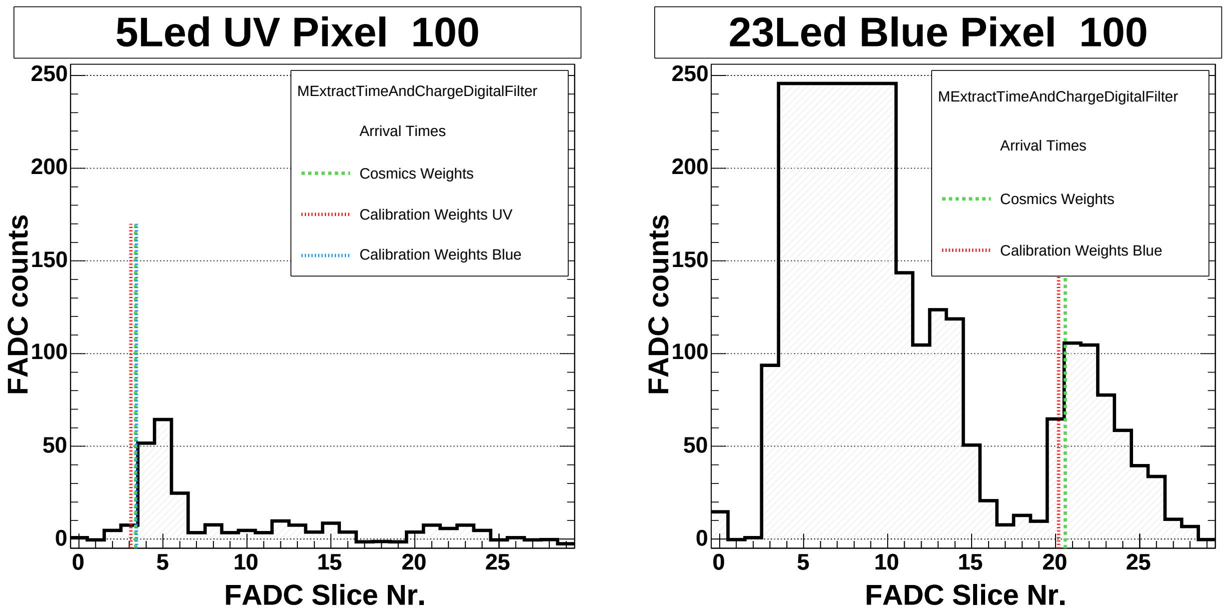

Figure 17: Sketch of the calculated arrival times for the extractor MExtractTimeAndChargeDigitalFilter for two typical calibration pulses (pedestals have been subtracted) and a typical inner pixel. The extraction window sizes modify the position of the (amplitude-weighted) mean FADC-slices slightly. The pulse would be shifted half a slice to the right for an outer pixels.

3.3.4 Digital Filter with Global Peak Search

This extractor is implemented in the MARS-class **MExtractTimeAndChargeDigitalFilterPeakSearch**.

The idea of this extractor is to combine **MExtractFixedWindowPeakSearch** (the same reference point for all pixels) and **MExtractTimeAndChargeDigitalFilter**, where the reference point is determined pixel by pixel, in order to correct for coherent movements in arrival time for all pixels and still use the digital filter fit capabilities.

In a first loop over the pixels, it fixes a reference point (slice number) defined by the highest sum of consecutive non-saturating FADC slices in a (smaller) peak-search window.

In a second loop over the pixels, it uses the digital filter algorithm within a reduced extraction window. It loops twice over all pixels in every event, because it has to find the reference point, first.

[1]UV-pulses saturating the high-gain are not yet available.
[2]UV-pulses saturating the high-gain are not yet available.

As in the case of **MExtractFixedWindowPeakSearch**, for a high intensity calibration run causing high-gain saturation in the whole camera, this extractor apparently fails since only dead pixels are taken into account in the peak search which cannot produce a saturated signal.

For this special case, the extractor then defines the peak search window as the one starting from the mean position of the first saturating slice.

The following adjustable parameters have to be set from outside, additionally to the ones to be set in **MExtractTimeAndChargeDigitalFilter**:

Peak Search Window: Defines the "sliding window" size within which the peaking sum is searched for (default: 2 slices)

Offset left from Peak: Defines the left offset of the start of the extraction window w.r.t. the starting point of the obtained peak search window (default: 3 slices)

Offset right from Peak: Defines the right offset of the of the extraction window w.r.t. the starting point of the obtained peak search window (default: 3 slices)

Limit for high gain failure events: Defines the limit of the number of events which failed to be in the high-gain window before the run is rejected.

Limit for low gain failure events: Defines the limit of the number of events which failed to be in the low-gain window before the run is rejected.

In principle, the "offsets" can be chosen very small, because both showers and calibration pulses spread over a very small time interval, typically less than one FADC slice. However, the MAGIC DAQ produces artificial jumps of two FADC slices from time to time[3], so the 3 slices are made in order not to reject these pixels already with the extractor.

3.3.5 Real Fit to the Expected Pulse Shape

The digital filter is a sophisticated numerical tool to fit the read-out FADC samples with the expected wave form taking the autocorrelation of the noise into account. In order to cross-check the results a pulse shape fit has been implemented using the root TH1::Fit routine. For each event the FADC samples of each pixel are filled into a histogram and fit by the expected wave form having the time shift and the area of the fit pulse as free parameters. The results are in very good agreement with the results of the digital filter.

Figure 18 shows the distribution of the fit probability for simulated MC pulses. Both electronics and NSB noise are simulated. The distribution is mainly flat with a slight excess in the very lowest probability bins.

This extractor is not (yet) implemented as a MARS-class.

3.4 Used Extractors for this Analysis

We tested in this TDAS the following parameterized extractors:

[3] in 5% of the events per pixel in December 2004

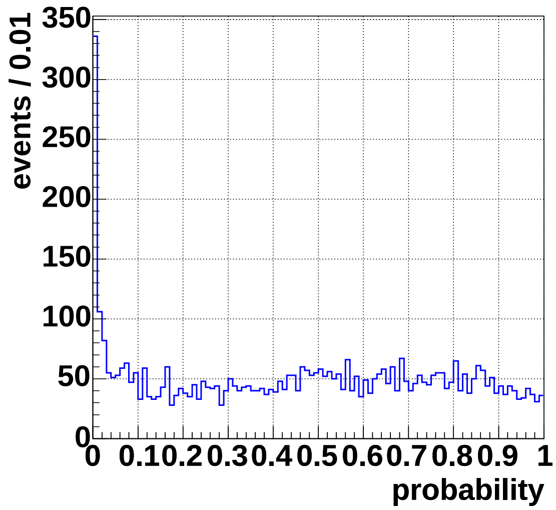

Figure 18: Probability of the fit with the input signal shape to the simulated FADC samples including electronics and NSB noise.

MExtractFixedWindow : with the following initialization, if *maxbin* defines the mean position of the high-gain FADC slice which carries the pulse maximum [4] :

1. SetRange(*maxbin*-1,*maxbin*+2,*maxbin*+0.5,*maxbin*+3.5);
2. SetRange(*maxbin*-1,*maxbin*+2,*maxbin*-0.5,*maxbin*+4.5);
3. SetRange(*maxbin*-2,*maxbin*+3,*maxbin*-0.5,*maxbin*+4.5);
4. SetRange(*maxbin*-2,*maxbin*+5,*maxbin*-0.5,*maxbin*+6.5);
5. SetRange(*maxbin*-3,*maxbin*+10,*maxbin*-1.5,*maxbin*+7.5);

MExtractFixedWindowSpline : with the following initialization, if *maxbin* defines the mean position of the high-gain FADC slice carrying the pulse maximum [5]:

6. SetRange(*maxbin*-1,*maxbin*+3,*maxbin*+0.5,*maxbin*+4.5);
7. SetRange(*maxbin*-1,*maxbin*+3,*maxbin*-0.5,*maxbin*+5.5);
8. SetRange(*maxbin*-2,*maxbin*+4,*maxbin*-0.5,*maxbin*+5.5);
9. SetRange(*maxbin*-2,*maxbin*+6,*maxbin*-0.5,*maxbin*+7.5);
10. SetRange(*maxbin*-3,*maxbin*+11,*maxbin*-1.5,*maxbin*+8.5);

[4] The function *MExtractor::SetRange(higain first, higain last, logain first, logain last)* sets the extraction range with the high gain start bin *higain first* to (including) the last bin *higain last*. Analog for the low gain extraction range. Note that in MARS, the low-gain FADC samples start with the index 0 again, thus *maxbin+0.5* means in reality *maxbin+15+0.5*.

[5] The function *MExtractor::SetRange(higain first, higain last, logain first, logain last)* sets the extraction range with the high gain start bin *higain first* to (including) the last bin *higain last*. Analog for the low gain extraction range. Note that in MARS, the low-gain FADC samples start with the index 0 again, thus *maxbin+0.5* means in reality *maxbin+15+0.5*.

MExtractFixedWindowPeakSearch : with the following initialization:
SetRange(0,18,2,14); and:

11. SetWindows(2,2,2); SetOffsetFromWindow(0);
12. SetWindows(4,4,2); SetOffsetFromWindow(1);
13. SetWindows(4,6,4); SetOffsetFromWindow(0);
14. SetWindows(6,6,4); SetOffsetFromWindow(1);
15. SetWindows(8,8,4); SetOffsetFromWindow(1);
16. SetWindows(14,10,4); SetOffsetFromWindow(2);

MExtractTimeAndChargeSlidingWindow : with the following initialization:

17. SetWindowSize(2,2); SetRange(5,11,7,11);
18. SetWindowSize(4,4); SetRange(5,13,6,12);
19. SetWindowSize(4,6); SetRange(5,13,5,13);
20. SetWindowSize(6,6); SetRange(4,14,5,13);
21. SetWindowSize(8,8); SetRange(4,16,4,14);
22. SetWindowSize(14,10); SetRange(5,10,7,11);

MExtractTimeAndChargeSpline : with the following initialization:

23. SetChargeType(MExtractTimeAndChargeSpline::kAmplitude); SetRange(5,10,7,10);

SetChargeType(MExtractTimeAndChargeSpline::kIntegral);
and:

24. SetRiseTime(0.5); SetFallTime(0.5); SetRange(5,10,7,11);
25. SetRiseTime(0.5); SetFallTime(1.5); SetRange(5,11,7,12);
26. SetRiseTime(1.0); SetFallTime(3.0); SetRange(4,12,5,13);
27. SetRiseTime(1.5); SetFallTime(4.5); SetRange(4,14,3,13);

MExtractTimeAndChargeDigitalFilter : with the following initialization:

28. SetWeightsFile("cosmics_weights.dat"); SetRange(4,14,5,13);
29. SetWeightsFile("cosmics_weights4.dat"); SetRange(5,13,6,12);
30. SetWeightsFile("calibration_weights_UV.dat");
31. SetWeightsFile("calibration_weights4_UV.dat");
32. SetWeightsFile("calibration_weights_blue.dat");
33. SetWeightsFile("calibration_weights4_blue.dat");

References: [13, 12].

4 Criteria for the Optimal Signal Extraction

The goal for the optimal signal reconstruction algorithm is to compute an unbiased estimate of the strength and arrival time of the Cherenkov signal with the highest possible resolution for all signal intensities. The MAGIC telescope has been optimized to lower the energy threshold of observation in any respect. Particularly the choice for an FADC system has been made with an eye on the possibility to extract the smallest possible signals from air showers. It would be inconsequent not to continue the optimization procedure in the signal extraction algorithms and the subsequent image cleaning.

In the traditional image analysis, one takes the decision whether the extracted signal of a certain pixel is considered as signal or background. Those considered as signal are further used to compute the image parameters while the background ones are simply rejected. The calculation of the second moments of the image "ellipse" usually fails when applied to uncleaned images, therefore the decision is yes or no[6]. Moreover, already low contributions of mis-estimated background can degrade the resolution of the image parameters considerably. If one wants to lower the threshold for signal recognition, it is therefore mandatory to increase the efficiency with which the background is recognized as such. If the background resolution is bad, the signal threshold goes up and vice versa.

Also an accurate determination of the signal arrival time may help to distinguish between signal and background. The signal arrival times vary smoothly from pixel to pixel while the background noise is randomly distributed in time. Therefore it must be insured that the reconstructed arrival time corresponds to the same reconstructed pulse as the reconstructed charge.

One cuts on the probability that the reconstructed charge is due to background. This yields a lower reconstructed signal limit for an event being considered as signal at all. The lower the limit (keeping constant the background probability), the lower the analyzed energy threshold.

Furthermore, the algorithm must be stable with respect to changes in observation conditions and background levels and between signals obtained from gamma or hadronic showers or from muons.

Also the needed computing time is of concern.

4.1 Bias and Mean-squared Error

Consider a large number of identical signals S, corresponding to a fixed number of photo-electrons. By applying a signal extractor we obtain a distribution of estimated signals $\widehat{S}$ (for fixed S and fixed background fluctuations BG). The distribution of the quantity

$$X = \widehat{S} - S \tag{21}$$

has the mean B and the resolution R defined as:

[6]This restriction is not necessary any more in all advanced analyses using likelihood fits to the images or fourier transforms. Thereby any bias of the reconstructed signal leads to potentially wrong results.

$$B \quad = \quad < X > \quad = \quad < \widehat{S} > - S \tag{22}$$
$$R^2 \quad = < (X-B)^2 > \quad = \quad Var[\widehat{S}] \tag{23}$$
$$MSE \quad = \quad < X^2 > \quad = \quad Var[\widehat{S}] + B^2 \tag{24}$$

The parameter B is also called the **BIAS** of the estimator and MSE the **MEAN-SQUARED ERROR** which combines the variance of $\widehat{S}$ and the bias. Both depend generally on the size of S and the background fluctuations BG, thus: $B = B(S, BG)$ and $MSE = MSE(S, BG)$.

Usually, one measures easily the parameter R, but needs the MSE for statistical analysis (e.g. in the image cleaning). However, only in case of a vanishing bias B, the two numbers are equal. Otherwise, the bias B has to be known beforehand.

In the case of MAGIC the background fluctuations are due to electronics noise and the PMT response to LONS. The signals from the latter background are not distinguishable from the Cherenkov signals. Thus each algorithm which searches for the signals inside the recorded FADC time slices will have a bias. In case of no Cherenkov signal it will reconstruct the largest noise pulse.

Note that every sliding window extractor, the digital filter and the spline extractor have a bias, especially at low or vanishing signals S, but usually a much smaller R and in many cases a smaller MSE than the fixed window extractors.

4.2 Linearity

The reconstructed signal should be proportional to the total integrated charge in the FADCs due to the PMT pulse from the Cherenkov signal. A deviation from linearity is usually obtained in the following cases:

- At very low signals, the bias causes as too high reconstructed signal (positive X).
- At very high signals, the FADC system goes into saturation and the reconstructed signal becomes too low (negative X).
- Any error in the inter-calibration between the high- and low-gain acquisition channels yield an effective deviation from linearity.

The linearity is very important for the reconstruction of the shower energy and further the obtained energy spectra from the observed sources.

4.3 Low Gain Extraction

Because of the peculiarities of the MAGIC data acquisition system, the extraction of the low-gain pulse is somewhat critical: The low-gain pulse shape differs significantly from the high-gain shape. Due to the analog delay line, the low-gain pulse is wider and the integral charge is distributed over a longer time window.

The time delay between high-gain and low-gain pulse is small, thus for large pulses, misinterpretations between the tails of the high-gain pulse and the low-gain pulse might occur. Moreover, the total recorded time window is relatively small and for late high-gain pulses, parts of the low-gain pulse might already reach out of the recorded FADC window. A good extractor must be stably extracting the low-gain pulse without being confused by the above points. This is especially important since the low-gain pulses are due to the large signals with a big impact on the image parameters, especially the size parameter.

4.4 Stability

The signal extraction algorithms has to reconstruct stably the charge for different types of pulses with different intrinsic pulse shapes and backgrounds:

- cosmics signals from gammas, hadrons and muons
- calibration pulses from different LED color pulsers
- pulse generator pulses in the pulpo setup

An important point is the difference between the pulse shapes of the calibration and Cherenkov signals. It has to be ensured that the computed calibration factor between the reconstructed charge in FADC counts and photo electrons for calibration events is valid for signals from Cherenkov photons.

4.5 Intrinsic Differences between Calibration and Cosmics Pulses

The calibration pulse reconstruction sets two important constraints to the signal extractor:

1. As the standard calibration uses the F-Factor method in order to reconstruct the number of impinging photo-electrons, the resolution of the extractor must be constant for different signal heights, especially between the case: $S = 0$ and $S = 40 \pm 7$ photo-electrons which is the default intensity of the current calibration pulses. This constraint is especially non-trivial for extractors searching the signal in a sliding window.

2. As the calibration pulses are slightly wider than the cosmics pulses, the obtained conversion factors must not be affected by the difference in pulse shape. This puts severe constraints on all extractors which do not integrate the whole pulse or take the pulse shape into account.

4.6 Reconstruction Speed

Depending on the reconstruction algorithm the signal reconstruction can take a significant amount of CPU time. Especially the more sophisticated signal extractors can be time consuming which search for the position of the Cherenkov signals in the recorded FADC time slices and perform a fit to these samples. At any case, the extractor should not be significantly slower than the reading and writing routines of the MARS software.

Thus, for an online-analysis a different extraction algorithm might be chosen as for the final most accurate reconstruction of the signals offline.

4.7 Applicability for Different Sampling Speeds / No Pulse Shaping.

The current read-out system of the MAGIC telescope [4] with 300 MSamples/s is relatively slow compared to the fast pulses of about 2 ns FWHM of Cherenkov pulses. To acquire the pulse shape an artificial pulse shaping to about 6.5 ns FWHM is used. Thereby also more night sky background light is integrated which acts as noise.

For 2 ns FWHM fast pulses a 2 GSamples/s FADC provides at least 4 sampling points. This permits a reasonable reconstruction of the pulse shape. First prototype tests with fast digitization systems for MAGIC have been successfully conducted [14]. The signals have been reconstructed within the common MAGIC Mars software framework.

5 Monte Carlo

5.1 Introduction

Many characteristics of the extractor can only be investigated with the use of Monte-Carlo simulations [7] of signal pulses and noise for the following reasons:

- While in real conditions, the signal can only be obtained in a Poisson distribution, simulated pulses of a specific number of photo-electrons can be generated.
- The intrinsic arrival time spread can be chosen within the simulation.
- The same pulse can be studied with and without added noise, where the noise level can be deliberately adjusted.
- The photo-multiplier and optical link gain fluctuations can be tuned or switched off completely.

Nevertheless, there are always systematic differences between the simulation and the real detector. In our case, especially the following short-comings are of concern:

- No switching noise due to the low-gain switch has been simulated.
- The intrinsic transit time spread of the photo-multipliers has not been simulated.
- The pulses have been simulated in steps of 0.2 ns before digitization. There is thus an artificial numerical time resolution limit of $0.2\,\mathrm{ns}/\sqrt{12} \approx 0.06\,\mathrm{ns}$.
- The total dynamic range of the entire signal transmission chain was set to infinite, thus the detector has been simulated to be completely linear.
- The noise auto-correlation in the low-gain channel cannot be determined from data, but instead has to be retrieved from Monte-Carlo studies.

For the subsequent studies, the following settings have been used:

- The gain fluctuations for signal pulses were switched off.
- The gain fluctuations for the background noise of the light of night sky were instead fully simulated, i.e. very close to real conditions.
- The intrinsic arrival time spread of the photons was set to be 1 ns, as expected for gamma showers.
- The conversion of total integrated charge to photo-electrons was set to be 7.8 FADC counts per photo-electron, independent of the signal strength.
- The trigger jitter was set to be uniformly distributed over 1 FADC slice only.

- Only one inner pixel has been simulated.
- The night sky background was simulated about 20% lower than in extra-galactic source observation conditions.

The last point had the consequence that the extractor **MExtractFixedWindowPeakSearch** could not be tested since it was equivalent to the sliding window. In the following, we used the Monte-Carlo to determine especially the following quantities for each of the tested extractors:

- The charge resolution as a function of the input signal strength.
- The charge extraction bias as a function of the input signal strength.
- The time resolution as a function of the input signal strength.
- The effect of adding or removing noise for the above quantities.

5.2 Conversion Factors

The following figures 19 through 21 show the conversion factors between reconstructed charge and the number of input photo-electrons for each of the tested extractors, with and without added noise and for the high-gain and low-gain channels, respectively. One can see that the conversion factors depend on the extraction window size and that the addition of noise raises the conversion factors uniformly for all fixed window extractors in the high-gain channel, while all extractors using a sliding window show a bias at low signal intensities.

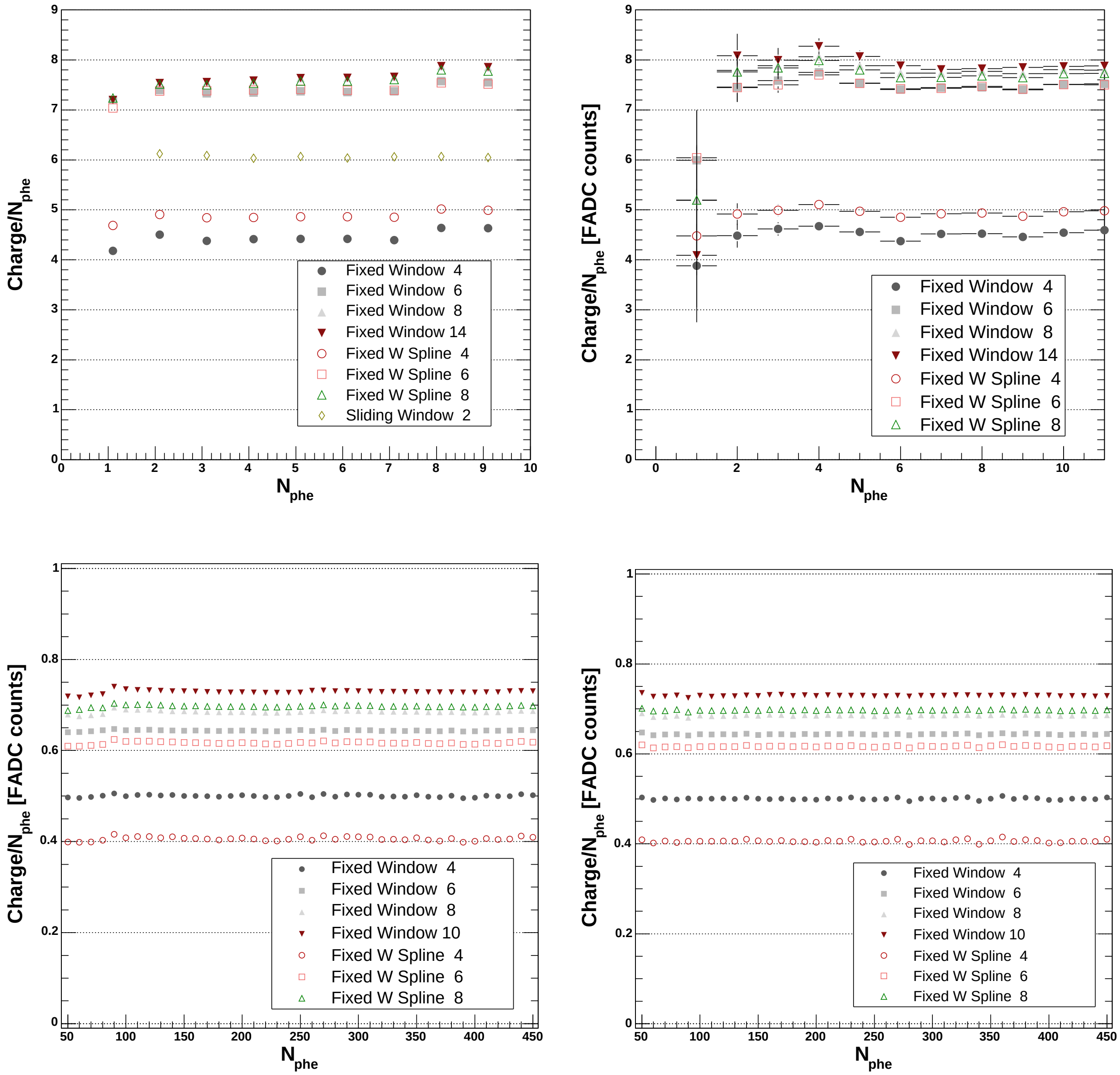

Figure 19: Extracted charge per photoelectron versus number of photoelectrons, for fixed window extractors in different window sizes. The top plots show the high-gain and the bottom ones low-gain regions. Left: without noise, right: with simulated noise.

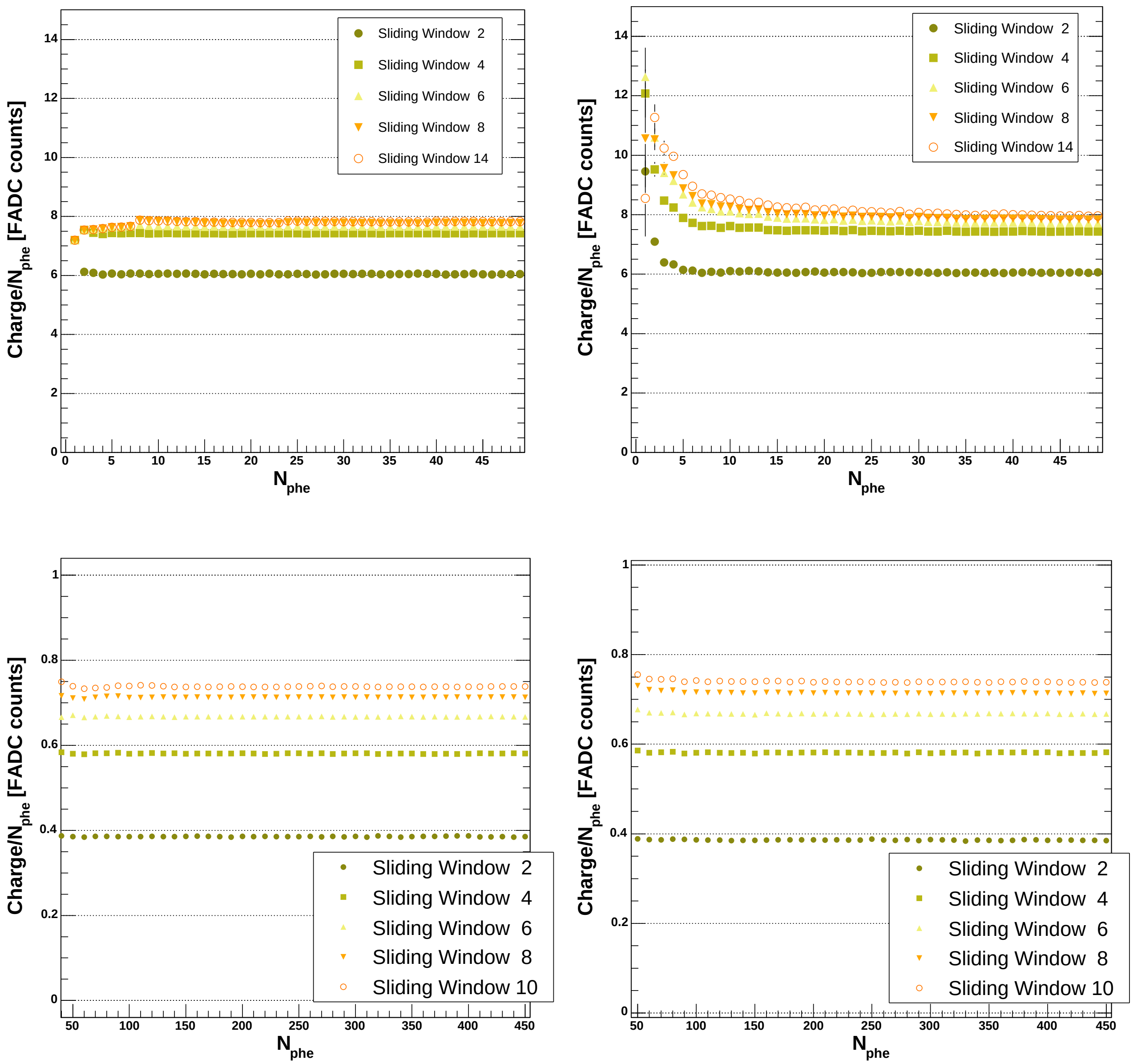

Figure 20: Extracted charge per photoelectron versus number of photoelectrons, for sliding window extractors in different window sizes. The top plots show the high-gain and the bottom ones low-gain regions. Left: without noise, right: with simulated noise.

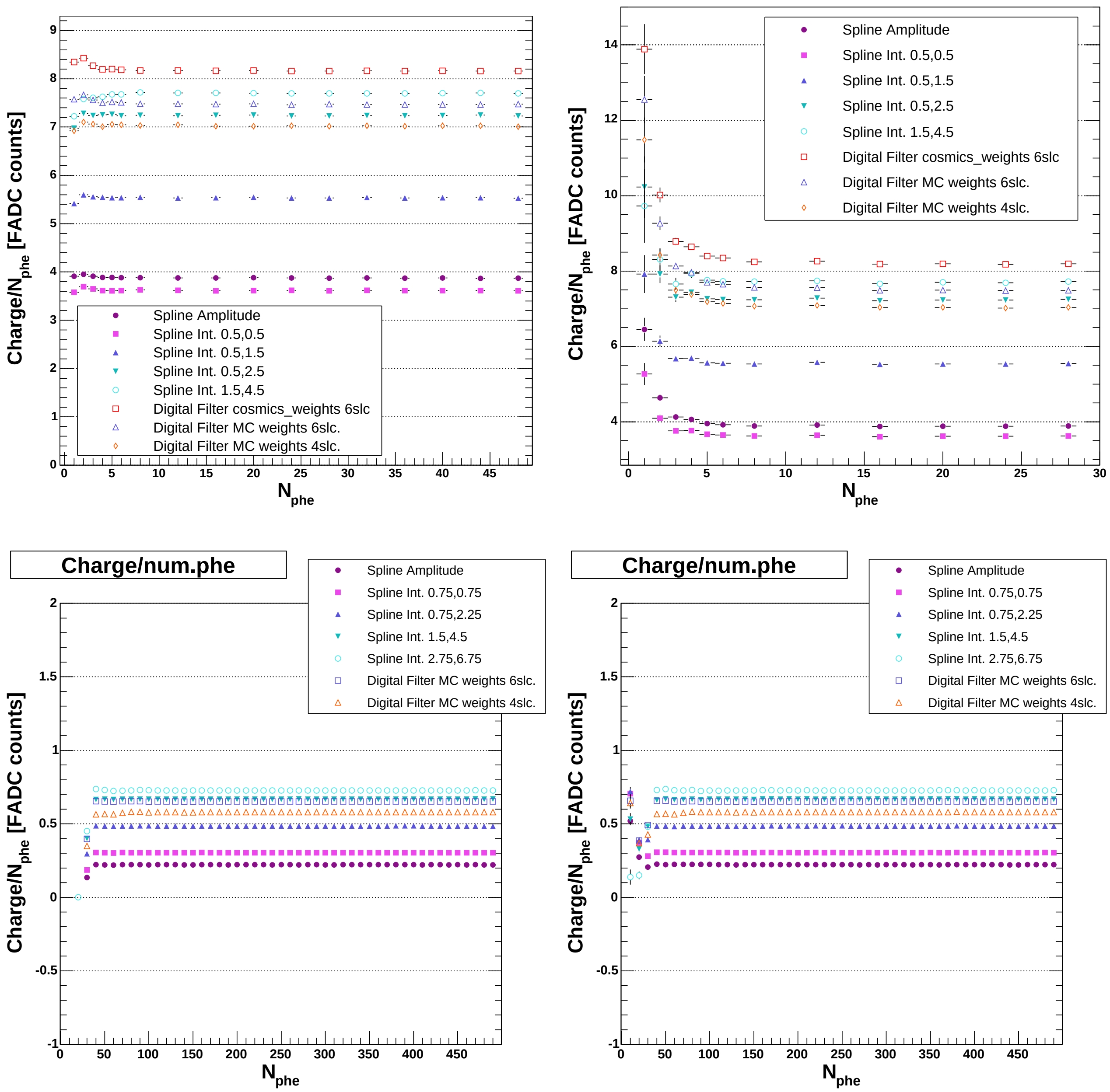

Figure 21: Extracted charge per photoelectron versus number of photoelectrons, for spline and digital filter extractors in different window sizes. The top plots show the high-gain and the bottom ones low-gain regions. Left: without noise, right: with simulated noise.

5.3 Measurement of the Biases

We fitted the conversion factors obtained from the previous section in the constant region (above 10 phe) and used them to convert the extracted charge back to equivalent photo-electrons. After subtracting the simulated number of photo-electrons, the bias (in units of photo-electrons) is obtained.

Figure 22 through 27 show the results for the tested extractors, with and without added noise and for the high and low-gain regions separately.

As expected, the fixed window extractor do not show any bias up to statistical precision. All sliding window extractor, however, do show a bias. Usually, the bias vanishes for signals above 5–10 photo-electrons, except for the sliding windows with window sizes above 8 FADC slices. There, the bias only vanishes for signals above 20 photo-electrons. The size of the bias as well as the minimum signal strength above which the bias vanishes are clearly correlated with the extraction window size. Therefore, smaller window sizes yield smaller biases and extend their linear range further downwards. The best extractors have a negligible bias above about 5 photo-electrons. This corresponds to the results found in section 6 where the lowest image cleaning threshold for extra-galactic noise levels yields about 5 photo-electrons as well.

All integrating spline extractors and all sliding window extractors with extraction windows above or equal 6 FADC slices yield the comparably smallest biases. The spline and digital filter biases fall down very steeply and have a bias only below 7 photo-electrons.

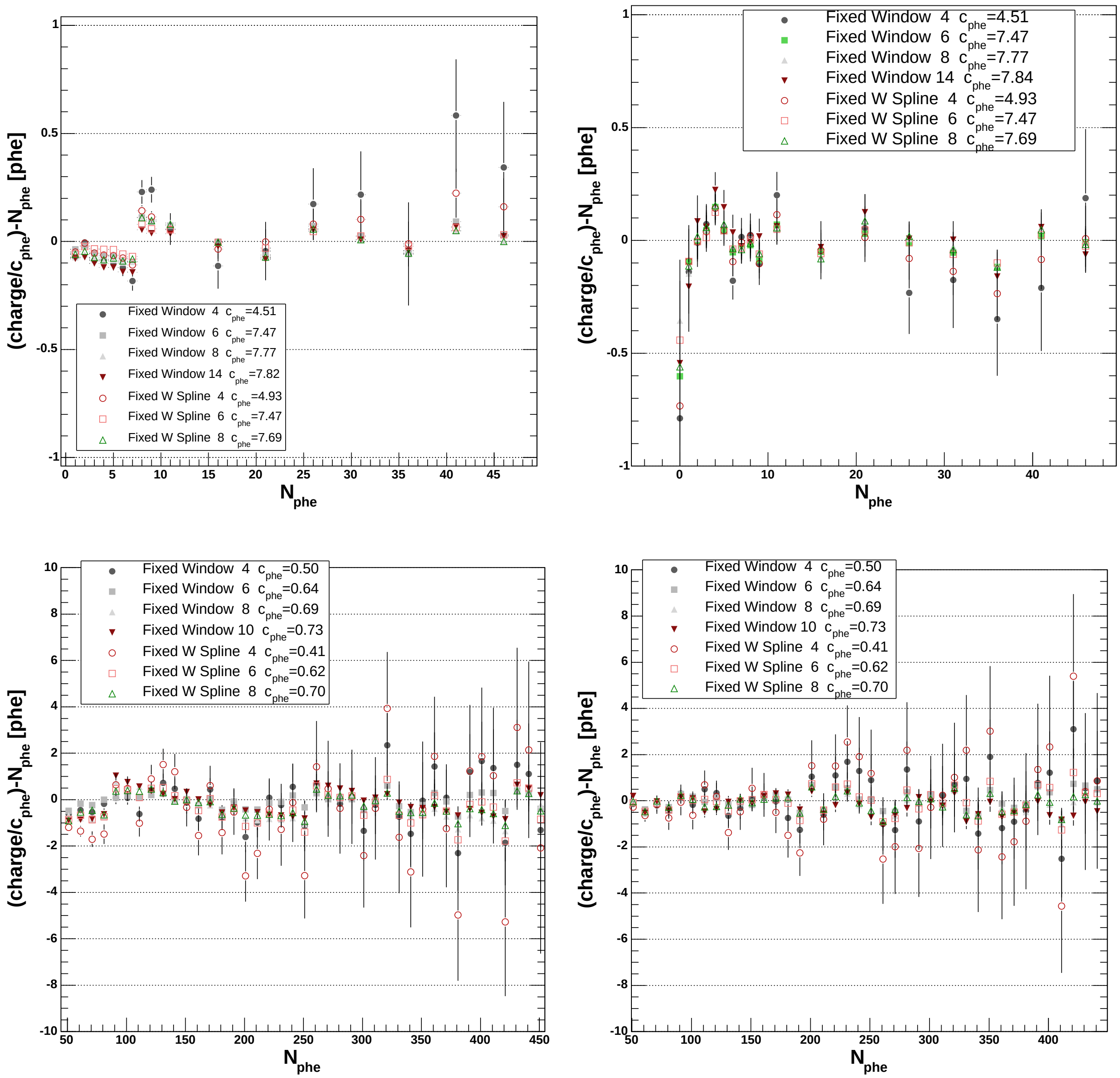

Figure 22: The measured bias (extracted charge divided by the conversion factor minus the number of photoelectrons) versus number of photoelectrons, for fixed window extractors in different window sizes. The top plots show the high-gain and the bottom ones low-gain regions. Left: without noise, right: with simulated noise.

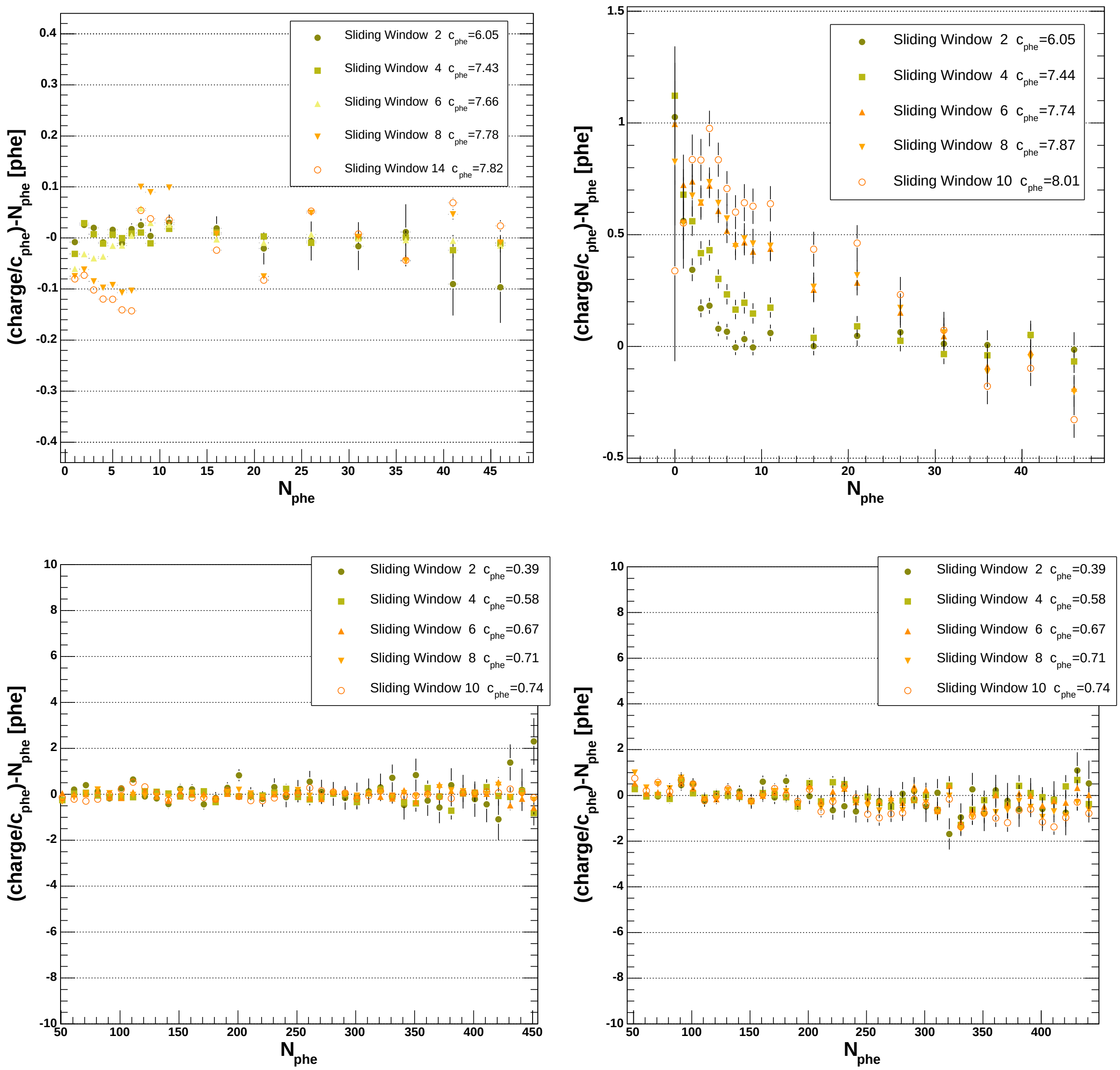

Figure 23: The measured bias (extracted charge divided by the conversion factor minus the number of photoelectrons) versus number of photoelectrons, for sliding window extractors in different window sizes. The top plots show the high-gain and the bottom ones low-gain regions. Left: without noise, right: with simulated noise.

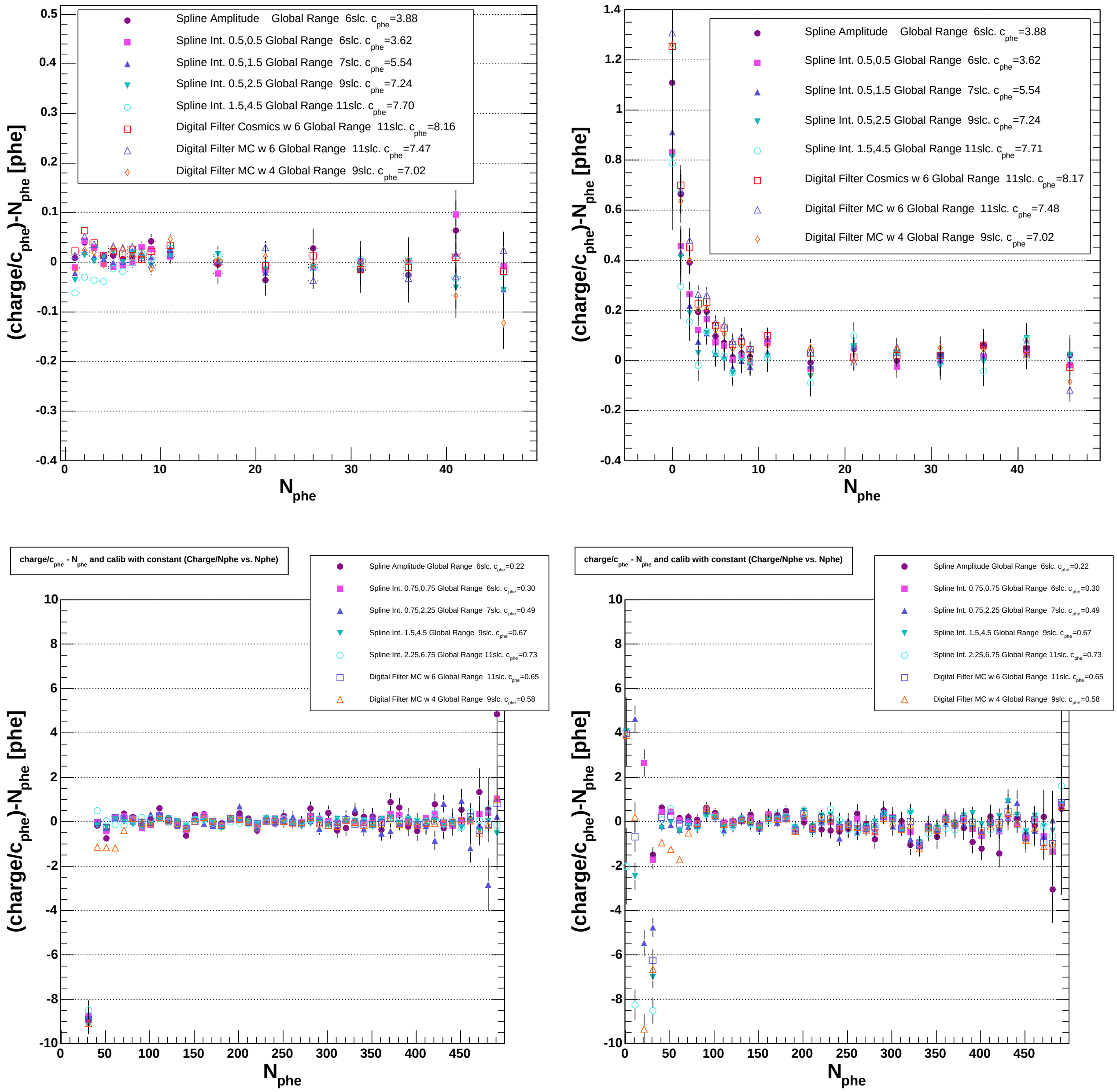

Figure 24: The measured bias (extracted charge divided by the conversion factor minus the number of photoelectrons) versus number of photoelectrons, for spline and digital filter extractors in different window sizes. The top plots show the high-gain and the bottom ones low-gain regions. Left: without noise, right: with simulated noise.

5.4 Measurement of the Resolutions

In order to obtain the resolution of a given extractor, we calculated the RMS of the distribution:

$$R_{\mathrm{MC}} \approx RMS(\widehat{Q}_{rec} - Q_{sim}) \tag{25}$$

where $\widehat{Q}_{rec}$ is the reconstructed charge, calibrated to photo-electrons with the conversion factors obtained in section 5.2.

One can see that for small signals, small extraction windows yield better resolutions, but extractors which do not entirely cover the whole pulse, show a clear dependency of the resolution with the signal strength. In the high-gain region, this is valid for all fixed window extractors up to 6 FADC slices integration region, all sliding window extractors up to 4 FADC slices and for all spline extractors and the digital filter. Among those extractors with a signal dependent resolution, the digital filter with 6 FADC slices extraction window shows the smallest dependency: It raises by about 80% between zero and 50 photo-electrons, but remains constant over the entire low-gain range.

The digital filter over 4 FADC slices shows a good resolution only in the high-gain region. In the low-gain region, it grows even above the intrinsic Poissonian photo-electron fluctuation above 400 photo-electrons.

The dependency of the charge resolution from the signal intensity is at first sight in contradiction with eq. 14 where the (theoretical) resolution depends only on the noise intensity. Probably, the input light distribution of the simulated light pulse introduces the amplitude dependency (the constancy is recovered for photon signals with no intrinsic input time spread).

Note that at all intensities, but especially low intensities, the resolution of the digital filter with 6 FADC slices is better than the one for any of the spline extractors.

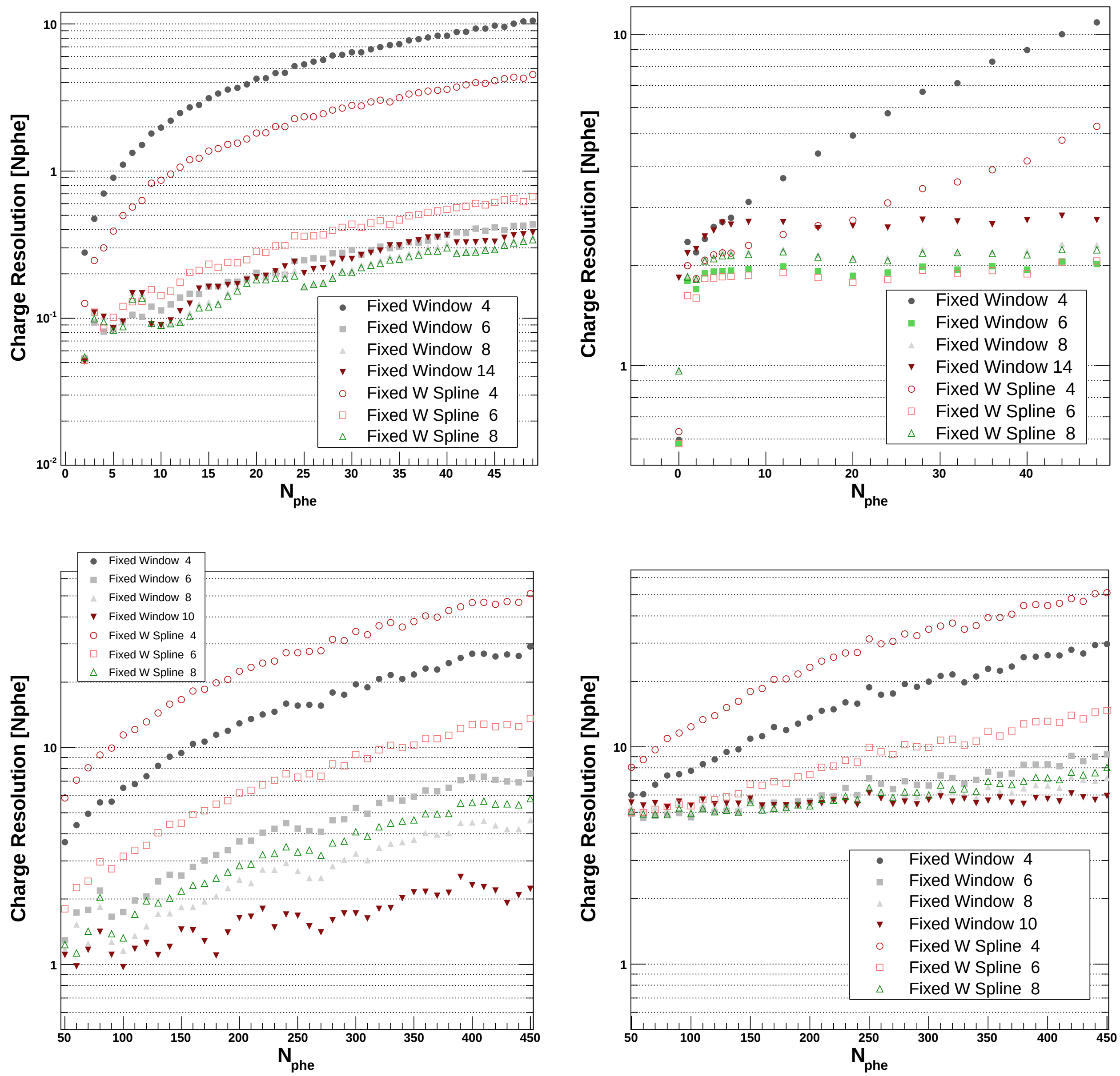

Figure 25: The measured resolution (RMS of extracted charge divided by the conversion factor minus the number of photoelectrons) versus number of photoelectrons, for fixed window extractors in different window sizes. The top plots show the high-gain and the bottom ones low-gain regions. Left: without noise, right: with simulated noise.

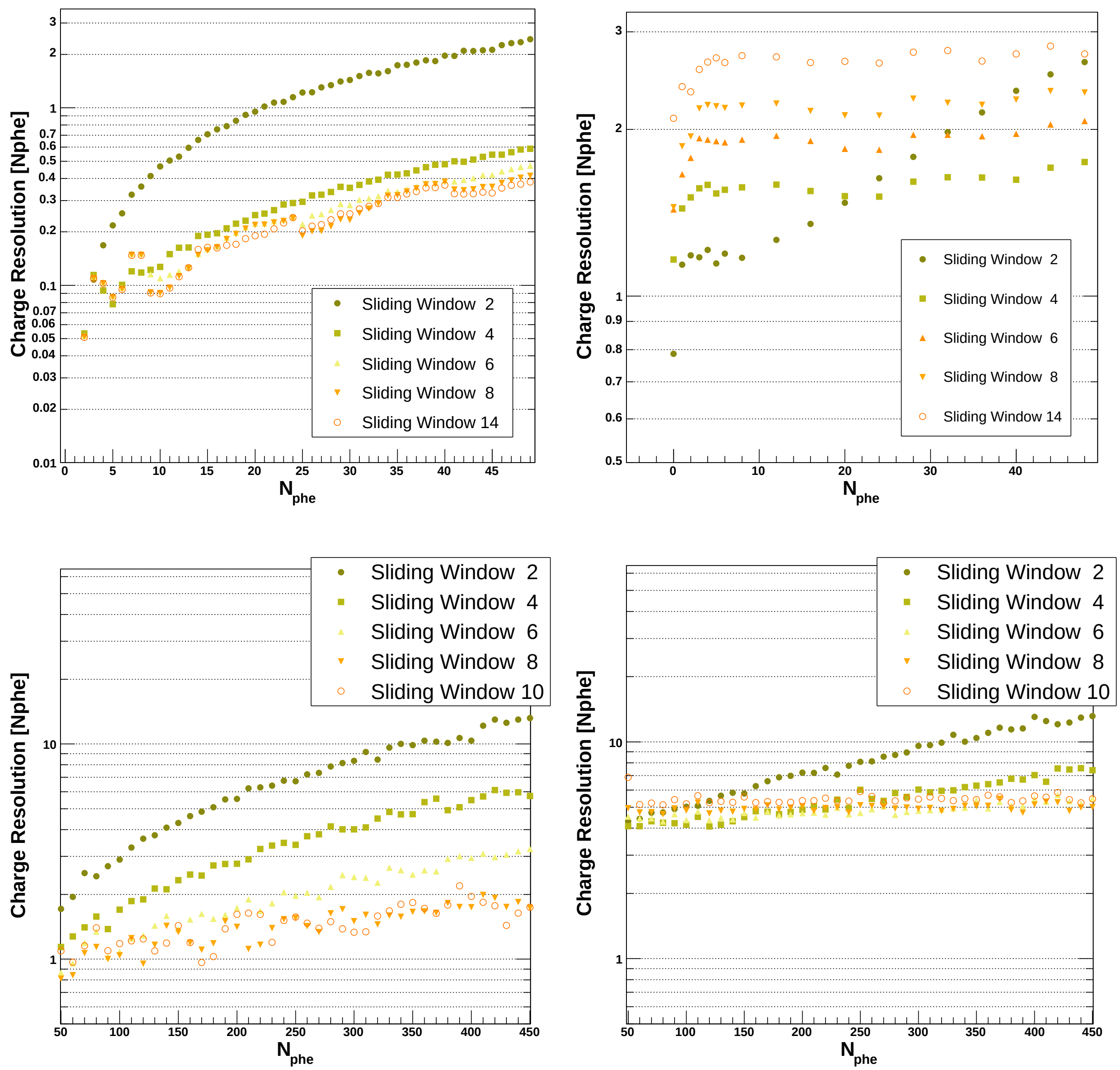

Figure 26: The measured resolution (RMS of extracted charge divided by the conversion factor minus the number of photoelectrons) versus number of photoelectrons, for sliding window extractors in different window sizes. The top plots show the high-gain and the bottom ones low-gain regions. Left: without noise, right: with simulated noise.

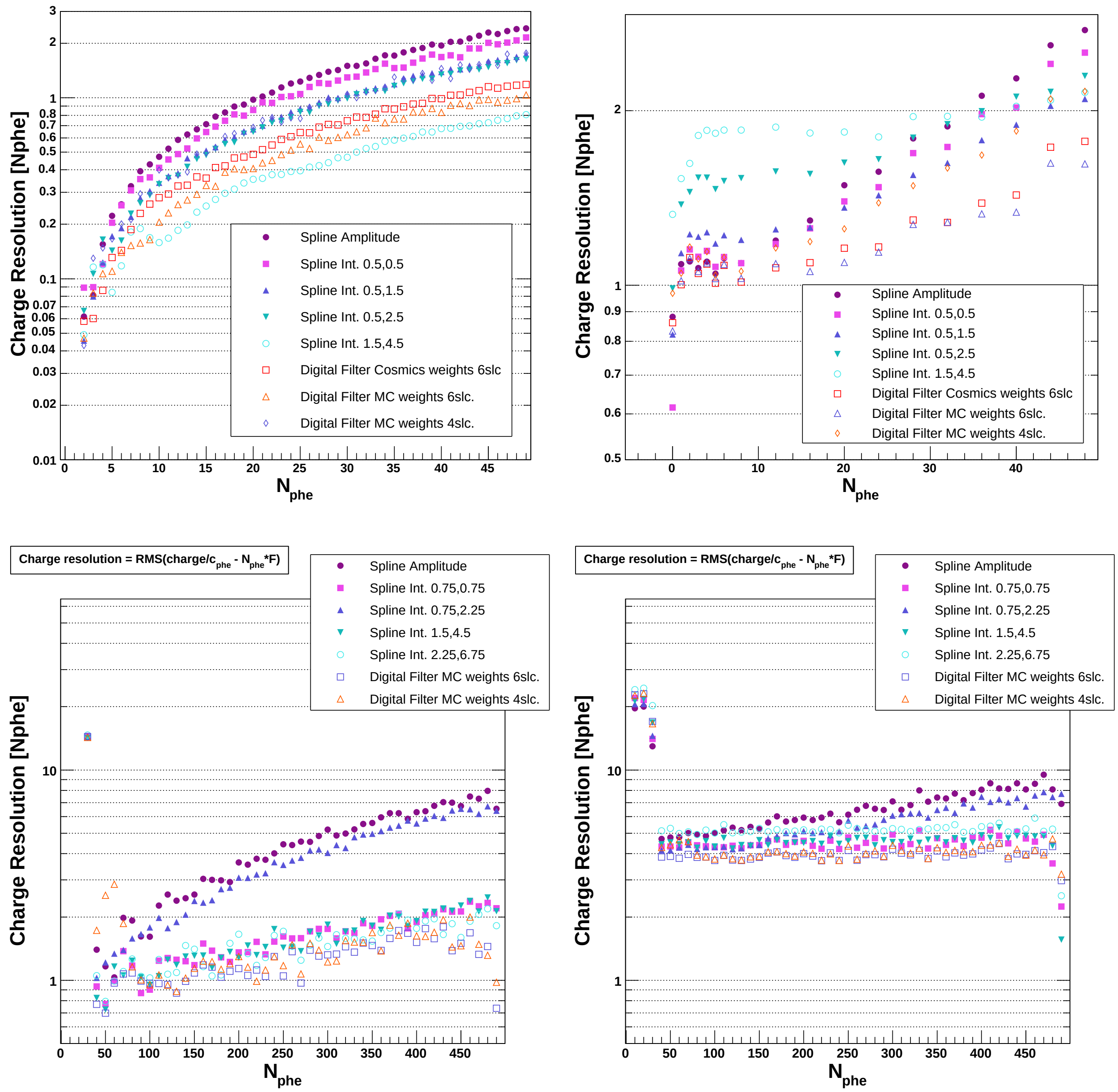

Figure 27: The measured resolution (RMS of extracted charge divided by the conversion factor minus the number of photoelectrons) versus number of photoelectrons, for spline and digital filter extractors in different window sizes. The top plots show the high-gain and the bottom ones low-gain regions. Left: without noise, right: with simulated noise.

5.5 Arrival Times

Like in the case of the charge resolution, we calculated the RMS of the distribution of the deviation of the reconstructed arrival time with respect to the simulated time:

$$\Delta T_{\mathrm{MC}} \approx RMS(\widehat{T}_{rec} - T_{sim}) \tag{26}$$

where $\widehat{T}_{rec}$ is the reconstructed arrival time and T_{sim} the simulated one.

Generally, the time resolutions ΔT_{MC} are about a factor 1.5 better than those obtained from the calibration (section 8.6, figure 79). This is understandable since the Monte-Carlo pulses are smaller and further the intrinsic time spread of the photo-multiplier has not been simulated. Moreover, no time resolution offset was simulated, thus the reconstructed time resolutions follow about a $1/\sqrt{N_{\mathrm{phe}}}$ – behaviour over the whole low-gain range. The spline extractors level off in contradiction to what has been found with the calibration pulses.

In figure 28, one can see nicely the effect of the addition of noise to the reconstructed time resolution: While without noise all sliding window extractors with a window size of at least 4 FADC slices show the same time resolution, with added noise, the resolution degrades with larger extraction window sizes. This can be understood by the fact that an extractor covers the whole pulse if integrating at least 4 FADC slices and each additional slice can only be affected by the noise.

In the high-gain, only the small sliding windows below or equal 4 FADC slices yield a good time resolution, as well as the spline and the digital filters. In the low-gain, only sliding windows larger than 4 FADC slices, the half-maximum searching spline and the digital filter with 6 FADC slices improve the time resolutions with respect to the high-gain pulses. Note that the digital filter with 4 FADC slices yields a rather poor resolution in the low-gain, just as the poor charge resolution found in the previous section.

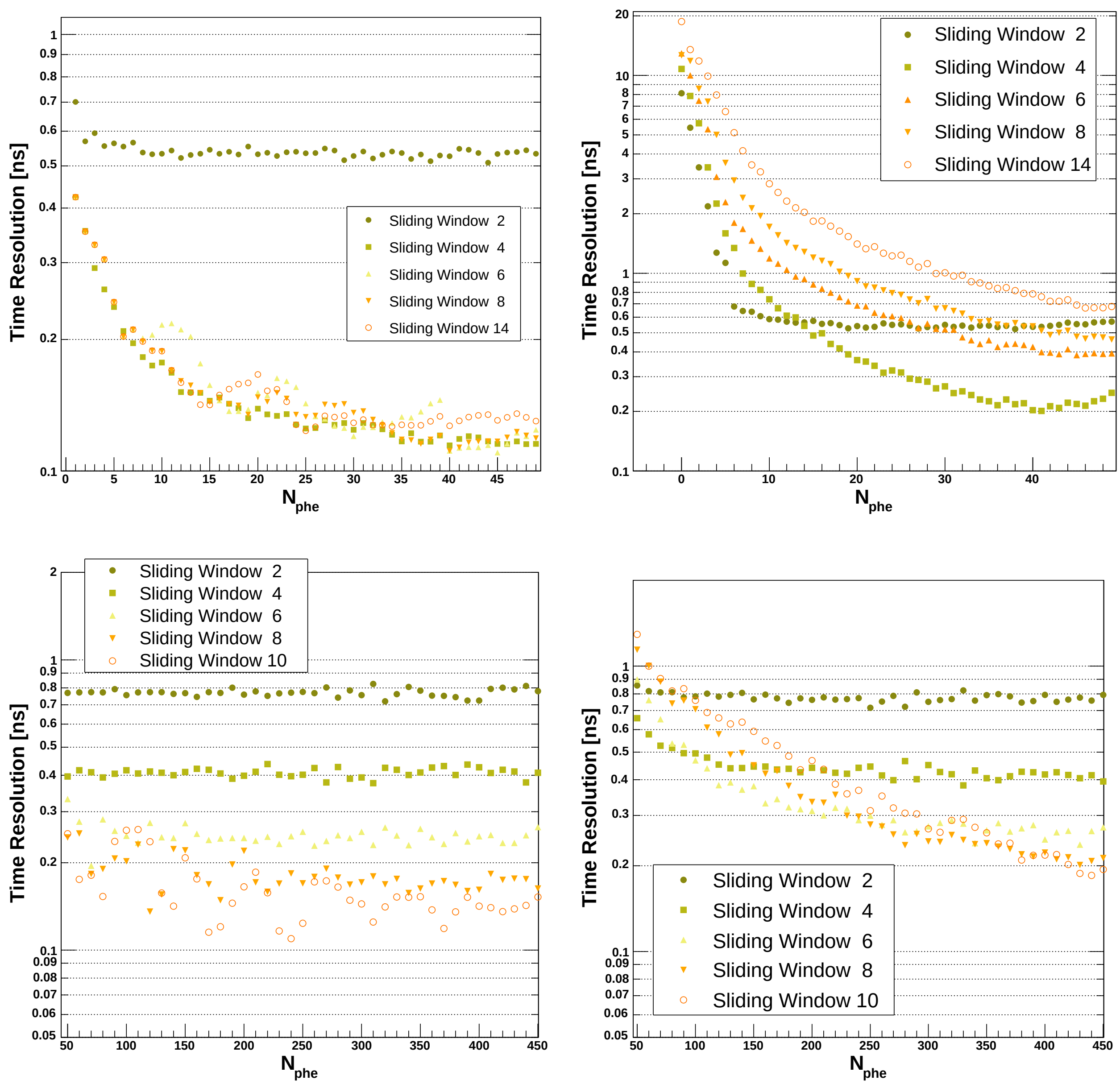

Figure 28: The measured time resolution (RMS of extracted time minus simulated time) versus number of photoelectrons, for sliding window extractors in different window sizes. The top plots show the high-gain and the bottom ones low-gain regions. Left: without noise, right: with simulated noise.

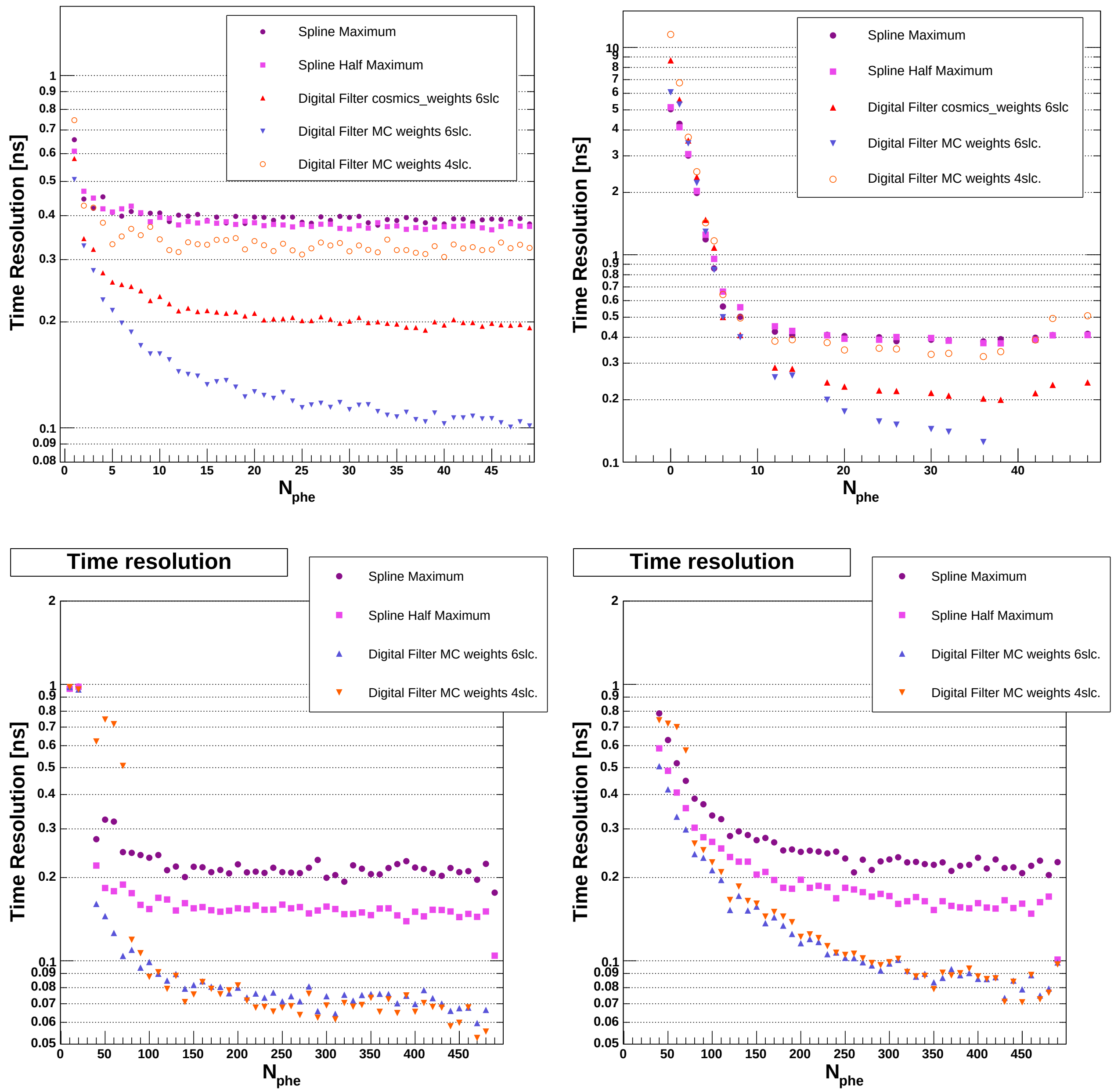

Figure 29: The measured time resolution (RMS of extracted time minus simulated time) versus number of photoelectrons, for spline and digital filter window extractors in different window sizes. The top plots show the high-gain and the bottom ones low-gain regions. Left: without noise, right: with simulated noise.

6 Pedestal Extraction

6.1 Pedestal RMS

The background BG (Pedestal) can be completely described by the noise-autocorrelation matrix $\boldsymbol{B}$ (eq. 5), where the square root of the diagonal elements give what is usually denoted as the "pedestal RMS".

By definition, $\boldsymbol{B}$ and thus the "pedestal RMS" is independent of the signal extractor.

6.2 Pedestal Fluctuations as Contribution to the Signal Fluctuations

A photo-multiplier signal yields, to a very good approximation, the following relation:

$$\frac{Var[Q]}{<Q>^2} = \frac{1}{<n_{\mathrm{phe}}>} * F^2 \tag{27}$$

Here, Q is the signal due to a number n_{phe} of signal photo-electrons (equiv. to the signal S) after subtraction of the pedestal. $Var[Q]$ is the fluctuation of the true signal Q due to the Poisson fluctuations of the number of photo-electrons. Because of:

$$\widehat{Q} = Q + X \tag{28}$$

$$Var[\widehat{Q}] = Var[Q] + Var[X] \tag{29}$$

$$Var[Q] = Var[\widehat{Q}] - Var[X] \tag{30}$$

Here, $Var[X]$ is the fluctuation due to the signal extraction, mainly as a result of the background fluctuations and the numerical precision of the extraction algorithm.

Only in the case that the intrinsic extractor resolution R at fixed background BG does not depend on the signal intensity[7], $Var[Q]$ can be obtained from:

$$Var[Q] \approx Var[\widehat{Q}] - Var[\widehat{Q}]\big|_{Q=0} \tag{31}$$

One can determine R by applying the signal extractor with a **fixed window** to pedestal events, where the bias vanishes and measure $Var(\widehat{Q})\big|_{Q=0}$.

6.3 Methods to Retrieve Bias and Mean-Squared Error

In general, the extracted signal variance R is different from the pedestal RMS. It can be obtained by applying the signal extractor to pedestal events yielding the bias and the resolution R.

In the case of the digital filter, R is expected to be independent of the signal amplitude S and dependent only on the background BG (eq. 14).

In order to calculate the statistical parameters, we proceed in the following ways:

[7] Theoretically, this is the case for the digital filter, eq. 14.

1. Determine R by applying the signal extractor to a fixed window of pedestal events. The background fluctuations can be simulated with different levels of night sky background and the continuous light source, but no signal size dependence can be retrieved by this method.

2. Determine B and MSE from MC events with added noise. With this method, one can get a dependence of both values on the size of the signal, although the MC might contain systematic differences with respect to the real data.

3. Determine MSE from the error retrieved from the fit results of $\widehat{S}$, which is possible for the fit and the digital filter (eq. 14). In principle, all dependencies can be retrieved with this method, although some systematic errors are not taken into account with this method: Deviations of the real pulse from the fitted one, errors in the noise auto-correlation matrix and numerical precision issues. All these systematic effects add an additional contribution to the true resolution proportional to the signal strength.

6.3.1 Application of the Signal Extractor to a Fixed Window of Pedestal Events

By applying the signal extractor with a fixed window to pedestal events, we determine the parameter R for the case of no signal ($Q = 0$)[8].

In MARS, this functionality is implemented with a function-call to:

MJPedestal::SetExtractionWithExtractorRndm() including
MExtractPedestal::SetRandomCalculation()

Besides fixing the global extraction window, additionally the following steps are undertaken in order to assure an un-biased resolution.

***MExtractTimeAndChargeSpline*:** The spline maximum position – which determines the exact extraction window – is placed at a random place within the digitizing binning resolution of one central FADC slice.

***MExtractTimeAndChargeDigitalFilter*:** The second step timing offset τ (eq. 18) is chosen randomly for each event.

The calculated biases obtained with this method for all pixels in the camera and for the different levels of (night-sky) background applied vanish to an accuracy of better than 2% of a photo-electron for the extractors which are used in this TDAS.

Table **??** shows the resolutions R obtained by applying an extractor to a fixed extraction window, for the inner and outer pixels, respectively, for four different camera illumination conditions: Closed camera (run #38993), star-field of an extra-galactic source observation (run #38995), star-field of the Crab-Nebula observation (run #39258) and observation with the

[8] In the case of extractors using a fixed window (extractors nr. #1 to #22 in section 3), the results are the same by construction as calculating the RMS of the sum of a fixed number of FADC slice, traditionally named "pedestal RMS" in MARS.

almost fully illuminated moon at an angular distance of about 60° from the telescope pointing position (run #46471). In the first three cases, the RMS of the values has been calculated while in the fourth case, the high-end side of the signal distributions have been fitted to a Gaussian.

The entries belonging to the rows denoted as "Slid. Win." are by construction identical to those obtained by simply summing up the FADC slices (the "fundamental Pedestal RMS"). Note that the digital filter yields much smaller values of R than the "sliding windows" of a same window size. This characteristic shows the "filter"–capacity of that algorithm. It "filters out" up to 50% of the night sky background photo-electrons.

One can see that the ratio between the pedestal RMS of outer and inner pixels is around a factor 3 for the closed camera and then 1.6–1.9 for the other conditions.

Resolution for $S = 0$ and fixed window (units in N_{phe})									
		Closed camera		Extra-gal. NSB		Galactic NSB		Moon	
Nr.	Name	R inner	R outer	R inner	R outer	R inner	R outer	R inner	R outer
17	Slid. Win. 2	0.3	0.9	1.2	2.0	1.5	2.4	3.0	5.3
18	Slid. Win. 4	0.4	1.2	1.6	2.7	2.0	3.3	3.9	7.3
20	Slid. Win. 6	0.5	1.6	2.0	3.5	2.4	4.3	4.7	9.0
21	Slid. Win. 8	0.6	2.0	2.3	4.1	2.9	5.0	5.3	10.1
23	Spline Amp.	0.3	0.8	1.0	1.8	1.2	2.2	2.5	4.9
24	Spline Int. 1	0.3	0.7	0.9	1.6	1.1	1.9	2.5	4.6
25	Spline Int. 2	0.3	0.9	1.2	2.0	1.5	2.4	3.0	5.3
26	Spline Int. 4	0.4	1.2	1.6	2.8	1.9	3.4	3.6	7.1
27	Spline Int. 6	0.5	1.6	1.9	3.6	2.4	4.2	4.3	8.7
28	Dig. Filt. 6	0.3	0.8	1.0	1.6	1.2	1.9	2.8	4.3
29	Dig. Filt. 4	0.3	0.7	0.9	1.6	1.1	1.9	2.5	4.3

Table 2: The mean resolution R for different extractors applied to a fixed window of pedestal events. Four different conditions of night sky background are shown: Closed camera, extra-galactic star-field, galactic star-field and almost full moon at 60° angular distance from the pointing position. With the first three conditions, a simple RMS of the extracted signals has been calculated while in the fourth case, a Gauss fit to the high part of the distribution has been made. The obtained values can typically vary by up to 10% for different channels of the camera readout.

6.3.2 Application of the Signal Extractor to a Sliding Window of Pedestal Events

By applying the signal extractor with a global extraction window to pedestal events, allowing it to "slide" and maximize the encountered signal, we determine the bias B and the mean-squared error MSE for the case of no signal ($S = 0$).

In MARS, this functionality is implemented with a function-call to:

MJPedestal::SetExtractionWithExtractor()

Table 3 shows the bias, the resolution and the mean-square error for all extractors using a sliding window. In this sample, every extractor had the freedom to move 5 slices, i.e. the global window size was fixed to five plus the extractor window size. This first line shows the resolution of the smallest existing robust fixed window algorithm in order to give the reference value of 2.5 and 3 photo-electrons RMS for an extra-galactic and a galactic star-field, respectively.

One can see that the bias B typically decreases with increasing window size, while the error R increases with increasing window size, except for the digital filter. There is also a small difference between the obtained error on a fixed window extraction and the one obtained from a sliding window extraction in the case of the spline and digital filter algorithms. The mean-squared error has an optimum somewhere in between: In the case of the sliding window and the spline at the lowest window size, in the case of the digital filter at 4 slices. The global winners is extractor #29 (digital filter with integration of 4 slices). All sliding window extractors – except #21 – have a smaller mean-square error than the resolution of the fixed window reference extractor (row 1,#4). This means that the global error of the sliding window extractors is smaller than the one of the fixed window extractors with 8 FADC slices even if the first have a bias.

The important information for the image cleaning is the number of photo-electrons above which the probability for obtaining a noise fluctuation is smaller than 0.3% (3σ). We approximated that number with the formula:

$$N_{\mathrm{phe}}^{\mathrm{thres.}} \approx B + 3 \cdot R \tag{32}$$

Table 3 shows that most of the sliding window algorithms yield a smaller signal threshold than the fixed window ones, although the first have a bias. The lowest threshold of only 4.2 photo-electrons for the extra-galactic star-field and 5.0 photo-electrons for the galactic star-field is obtained by the digital filter fitting 4 FADC slices (extractor %29). This is almost a factor 2 lower than the fixed window results. Also the spline integrating 1 FADC slice (extractor %24) yields almost comparable results.

The results shown in table 3 are also roughly consistent with those obtained in [15]. The main difference consists in the usage of the digital filter with 4 FADC slices which achieves the best results in this analysis, but is not shown in [15].

Statistical Parameters for $S = 0$ (units in N_{phe})															
		Closed camera				Extra-galactic NSB					Galactic NSB				
Nr.	Name	R (FW)	R (SW)	B (SW)	$\sqrt{MSE}$ (SW)	R (FW)	R (SW)	B (SW)	$\sqrt{MSE}$ (SW)	$B+3R$ (99.7% prob.)	R (FW)	R (SW)	B (SW)	$\sqrt{MSE}$ (SW)	$B+3R$ (99.7% prob.)
4	Fixed Win. 8	1.2	–	0.0	1.2	2.5	–	0.0	2.5	7.5	3.0	–	0.0	3.0	9.0
–	Slid. Win. 1	0.4	0.4	0.4	0.6	1.2	1.2	1.3	1.8	4.9	1.4	1.4	1.5	2.0	5.7
17	Slid. Win. 2	0.5	0.5	0.4	0.6	1.4	1.4	1.2	1.8	5.4	1.6	1.6	1.5	2.2	6.1
18	Slid. Win. 4	0.8	0.8	0.5	0.9	1.9	1.9	1.2	2.2	6.9	2.2	2.3	1.6	2.8	7.5
20	Slid. Win. 6	1.0	1.0	0.4	1.1	2.2	2.2	1.1	2.5	7.7	2.6	2.7	1.4	3.0	9.5
21	Slid. Win. 8	1.2	1.3	0.4	1.4	2.5	2.5	1.0	2.7	8.5	3.0	3.2	1.4	3.5	10.0
23	Spline Amp.	0.4	**0.4**	0.4	0.6	1.1	1.2	1.3	1.8	4.9	1.3	1.4	1.6	2.1	5.8
24	**Spline Int. 1**	0.4	**0.4**	0.3	**0.5**	1.0	1.2	1.0	1.6	4.6	1.3	**1.3**	1.3	1.8	5.2
25	Spline Int. 2	0.5	0.5	0.3	0.6	1.3	1.4	0.9	1.7	5.1	1.7	1.6	1.2	2.0	6.0
26	Spline Int. 4	0.7	0.7	**0.2**	0.7	1.5	1.7	**0.8**	1.9	5.3	2.0	2.0	1.0	2.2	7.0
27	Spline Int. 6	1.0	1.0	0.3	1.0	2.0	2.0	**0.8**	2.2	6.8	2.6	2.5	**0.9**	2.7	8.4
28	Dig. Filt. 6	0.4	0.5	0.4	0.6	1.1	1.3	1.3	1.8	5.2	1.3	1.5	1.5	2.1	6.0
29	**Dig. Filt. 4**	0.3	**0.4**	0.3	**0.5**	0.9	**1.1**	0.9	**1.4**	**4.2**	1.0	**1.3**	1.1	**1.7**	**5.0**

Table 3: The statistical parameters bias, resolution and mean error for the algorithms which can be applied to sliding windows (SW) and/or fixed windows (FW) of pedestal events. The first line displays the resolution of the smallest existing robust fixed–window extractor for reference. All units in equiv. photo-electrons, uncertainty: 0.1 phes. All extractors were allowed to move 5 FADC slices plus their window size. The "winners" for each column are marked in red. Global winners (within the given uncertainty) are the extractors Nr. #24 (MExtractTimeAndChargeSpline with an integration window of 1 FADC slice) and Nr.#29 (MExtractTimeAndChargeDigitalFilter with an integration window size of 4 slices)

Figures 30 through 34 show the extracted pedestal distributions for some selected extractors (#18, #23, #25, #28 and #29) for one typical channel (pixel 100) and two background situations: Closed camera with only electronic noise and open camera pointing to an extra-galactic source. One can see the (asymmetric) Poisson behaviour of the night sky background photons for the distributions with open camera.

6.3.3 Comparison With Results From the Monte Carlo Simulation

The resolution and the bias from obtained with the signal extractor applied to a sliding window of pedestal events should coincide with the bias and the resolution found in the Monte Carlo simulation for the case of zero photo-electrons input. One has to take into account the slightly lower level of simulated night sky background, however. We thus expect the values of the 8$^{\text{th}}$ and 9$^{\text{th}}$ row of table 3 to be about 20% higher than the corresponding values obtained in the Monte Carlo simulation. Table 4 shows that this is indeed the case if one takes into account the statistical uncertainties of about 10%. Both the values for the bias and the resolution are generally slightly under-estimated in the Monte Carlo simulation, compared with real data. The only exception to this rule concerns the digital filter with 4 FADC slices which has a much higher bias in the simulation. Note however that all bias values have a large statistical uncertainty.

Comparison Statistical Parameters MC and Extra-Galactic Source Observation (units in N_{phe})					
Nr.	Name	B (MC)	B (Real)	R^9 (MC)	R (Real)
17	Slid. Win. 2	1.0	1.2	1.1	1.4
18	Slid. Win. 4	1.1	1.2	1.4	1.9
20	Slid. Win. 6	1.0	1.1	1.8	2.2
21	Slid. Win. 8	0.8	1.0	2.1	2.5
23	Spline Amp.	1.1	1.3	1.1	1.2
24	Spline Int. 1	0.8	1.0	1.1	1.2
25	Spline Int. 2	0.9	0.9	1.2	1.4
26	Spline Int. 4	0.8	0.8	1.3	1.7
27	Spline Int. 6	0.8	0.8	1.7	2.0
28	Dig. Filt. 6	1.25	1.3	1.1	1.3
29	Dig. Filt. 4	1.25	0.9	1.0	1.1

Table 4: The statistical parameters bias, resolution, compared between the Monte Carlo simulation results and a pedestal run taken with the telescope pointing to an extra-galactic source.

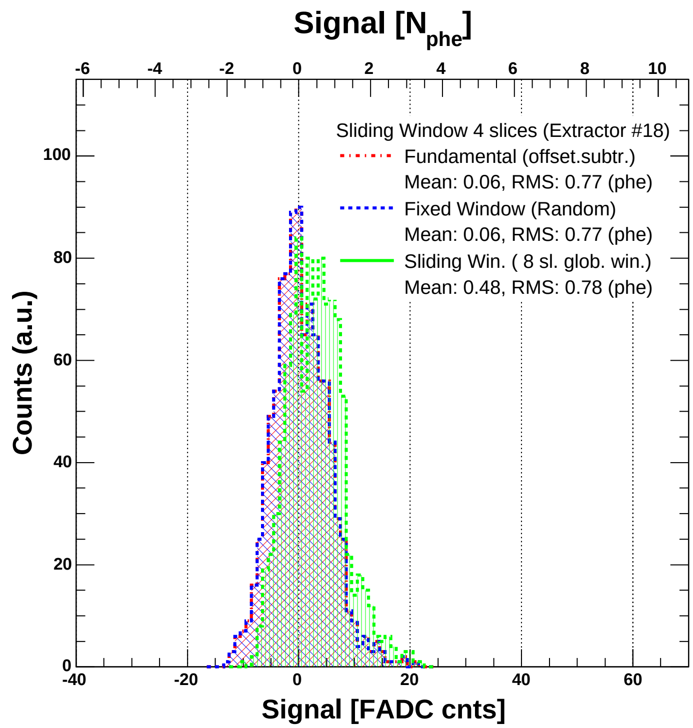

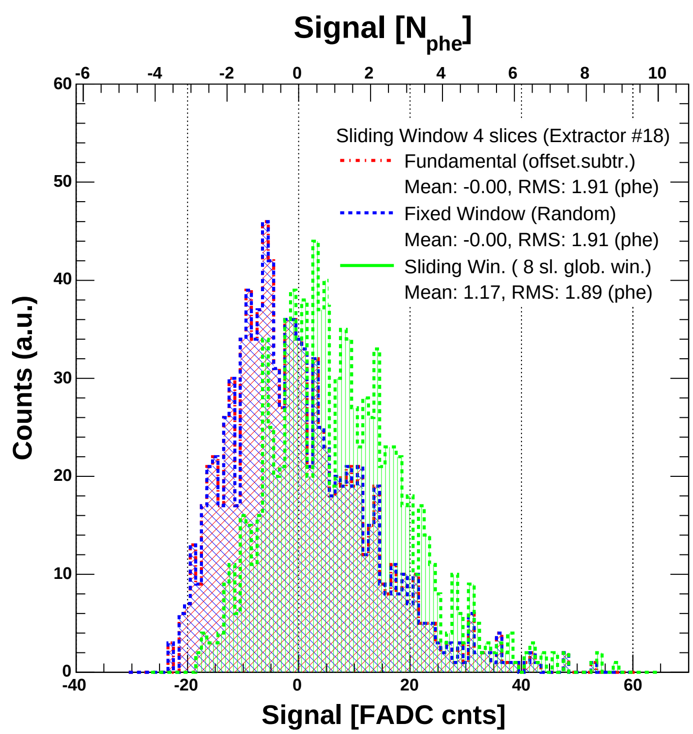

Figure 30: MExtractTimeAndChargeSlidingWindow with extraction window of 4 FADC slices: Distribution of extracted "pedestals" from pedestal run with closed camera (top) and open camera observing an extra-galactic star field (bottom) for one channel (pixel 100). The result obtained from a simple addition of 4 FADC slice contents ("fundamental") is displayed as red histogram, the one obtained from the application of the algorithm on a fixed window of 4 FADC slices as blue histogram ("extractor random") and the one obtained from the full algorithm allowed to slide within a global window of 12 slices. The obtained histogram means and RMSs have been converted to equiv. photo-electrons.

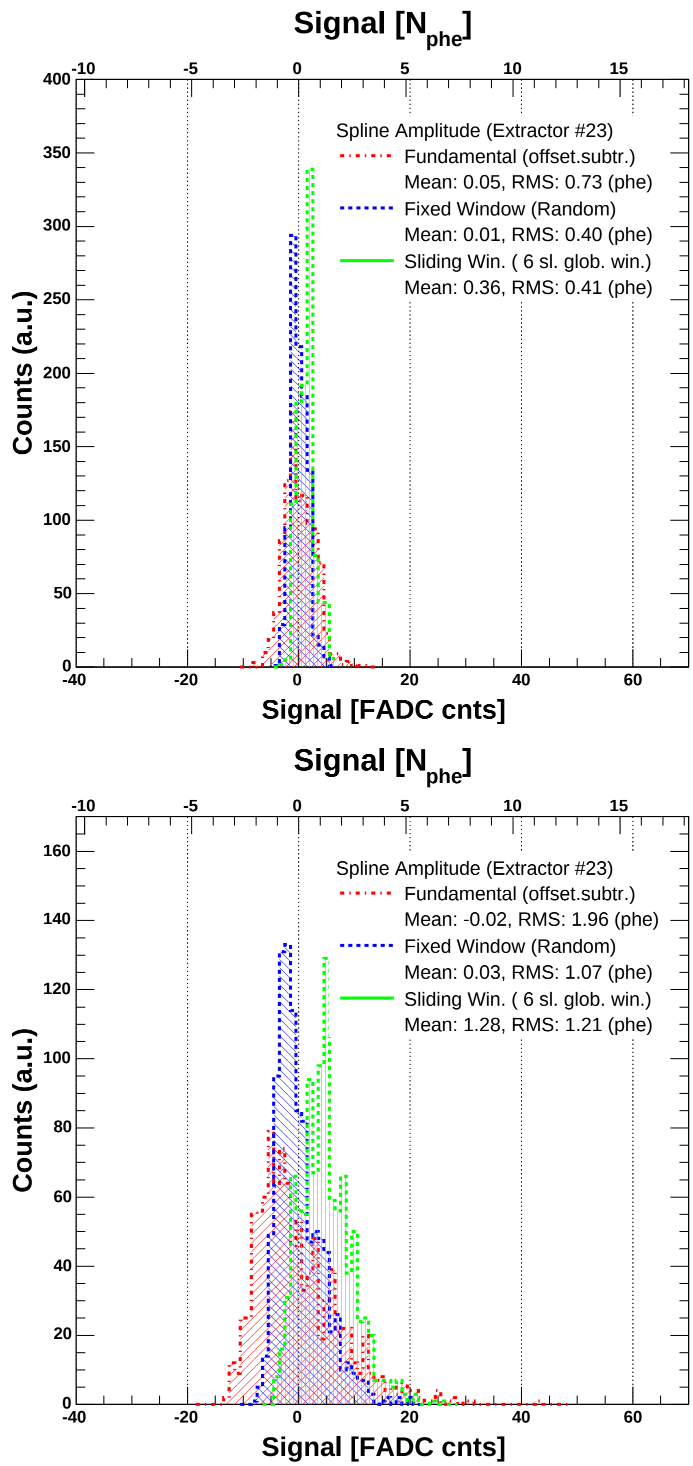

Figure 31: MExtractTimeAndChargeSpline with amplitude extraction: Spectrum of extracted "pedestals" from pedestal run with closed camera lids (top) and open lids observing an extra-galactic star field (bottom) for one channel (pixel 100). The result obtained from a simple addition of 2 FADC slice contents ("fundamental") is displayed as red histogram, the one obtained from the application of the algorithm on a fixed window of 1 FADC slice as blue histogram ("extractor random") and the one obtained from the full algorithm allowed to slide within a global window of 12 slices. The obtained histogram means and RMSs have been converted to equiv. photo-electrons.

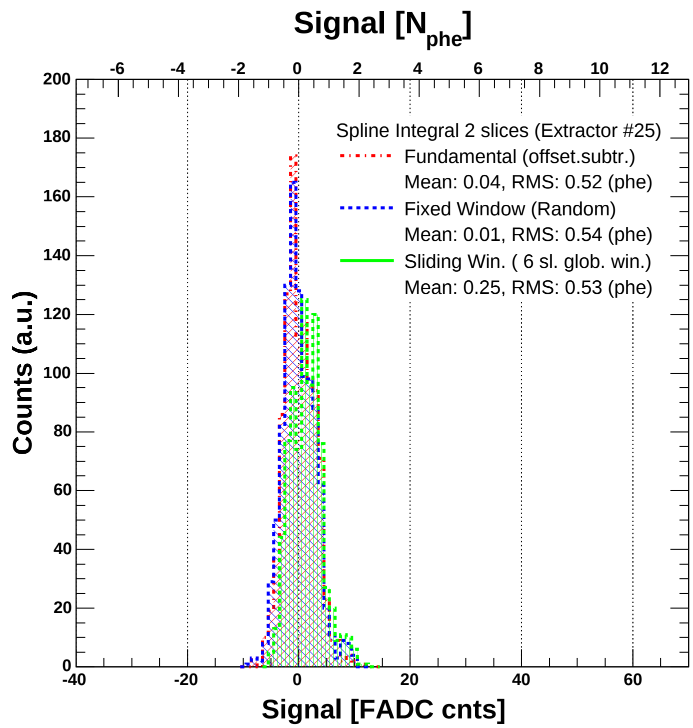

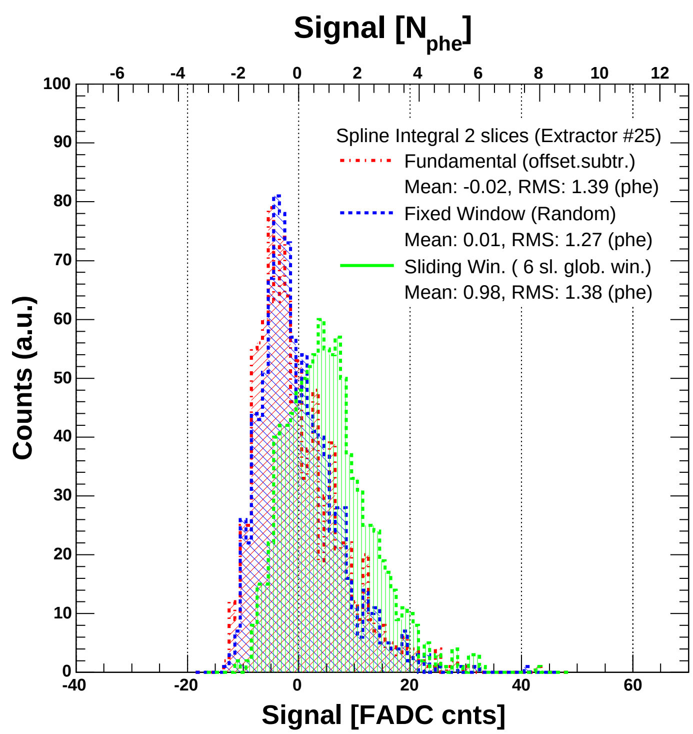

Figure 32: MExtractTimeAndChargeSpline with integral extraction over 2 FADC slices: Distribution of extracted "pedestals" from pedestal run with closed camera lids (top) and open lids observing an extra-galactic star field (bottom) for one channel (pixel 100). The result obtained from a simple addition of 2 FADC slice contents ("fundamental") is displayed as red histogram, the one obtained from the application of time-randomized weights on a fixed window of 2 FADC slices as blue histogram and the one obtained from the full algorithm allowed to slide within a global window of 12 slices. The obtained histogram means and RMSs have been converted to equiv. photo-electrons.

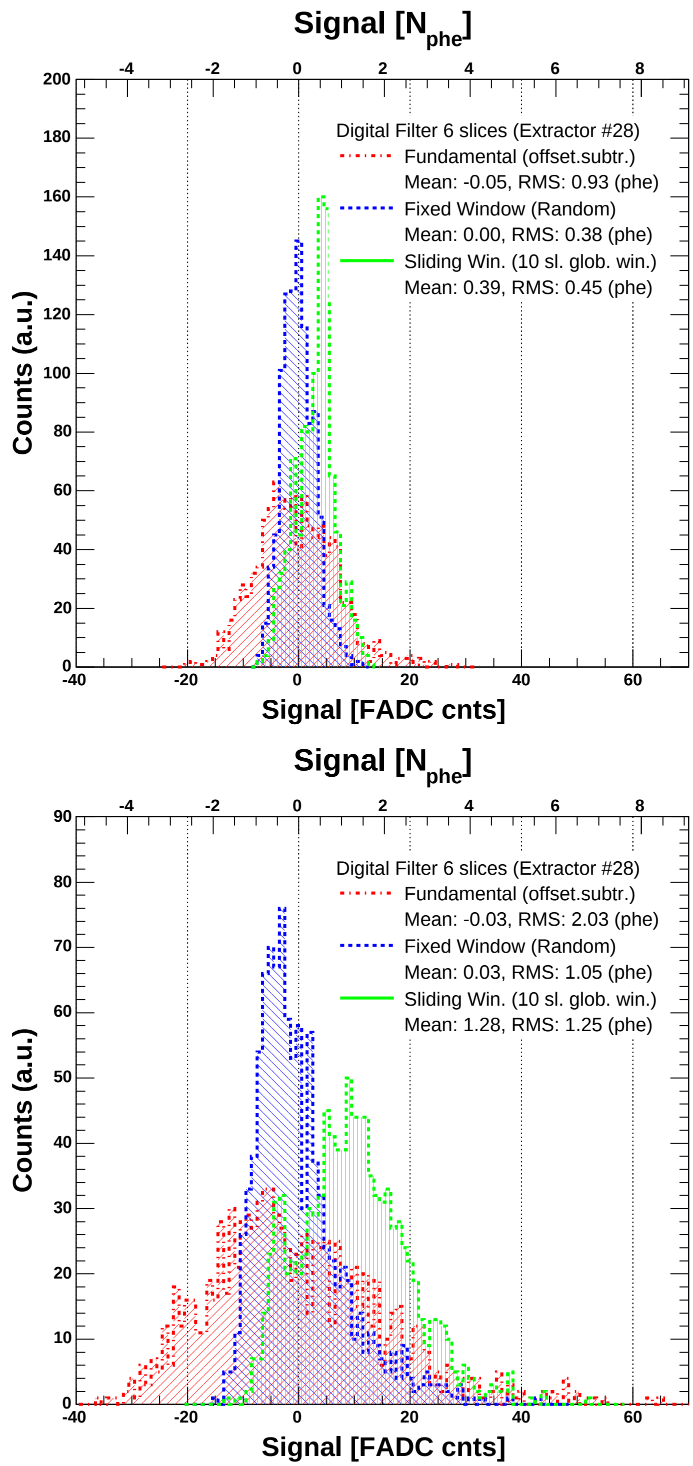

Figure 33: MExtractTimeAndChargeDigitalFilter: Spectrum of extracted "pedestals" from pedestal run with closed camera lids (top) and open lids observing an extra-galactic star field (bottom) for one channel (pixel 100). The result obtained from a simple addition of 6 FADC slice contents ("fundamental") is displayed as red histogram, the one obtained from the application of time-randomized weights on a fixed window of 6 slices as blue histogram and the one obtained from the full algorithm allowed to slide within a global window of 12 slices. The obtained histogram means and RMSs have been converted to equiv. photo-electrons.

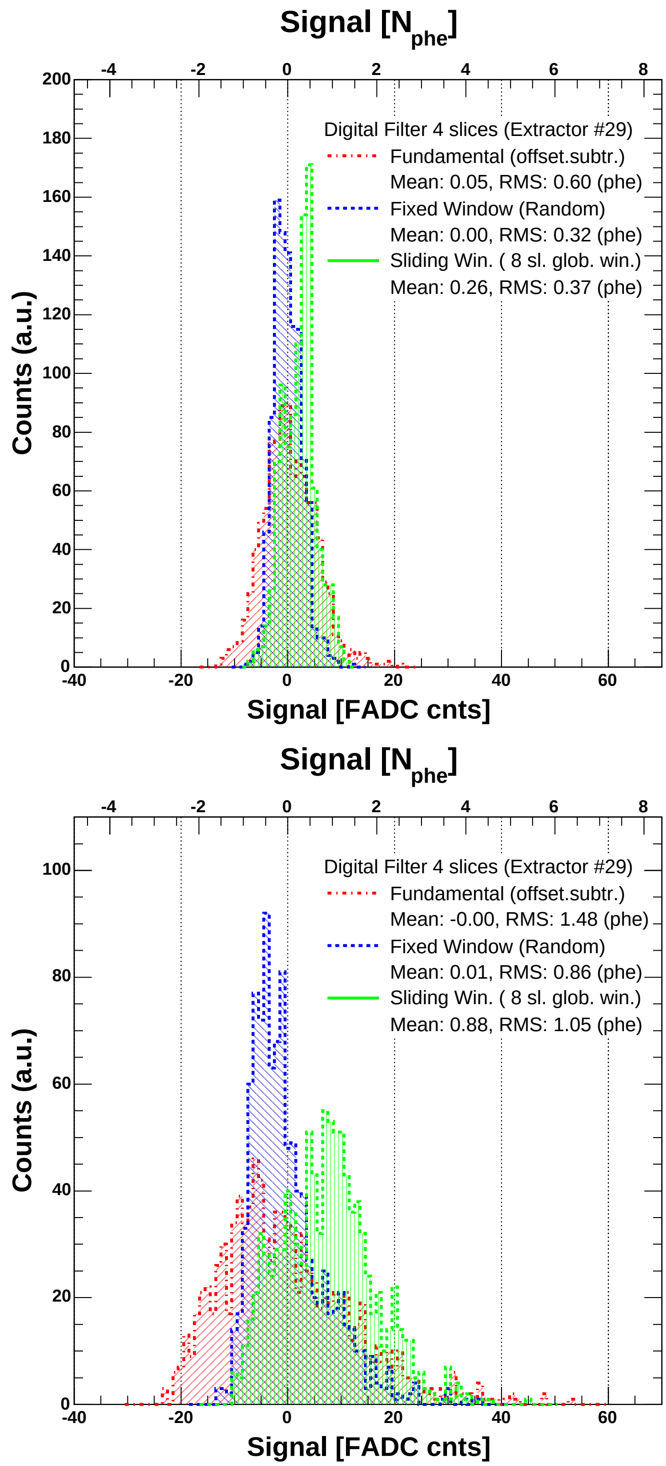

Figure 34: MExtractTimeAndChargeDigitalFilter: Spectrum of extracted "pedestals" from pedestal run with closed camera lids (top) and open lids observing an extra-galactic star field (bottom) for one channel (pixel 100). The result obtained from a simple addition of 4 FADC slice contents ("fundamental") is displayed as red histogram, the one obtained from the application of time-randomized weights on a fixed window of 4 slices as blue histogram and the one obtained from the full algorithm allowed to slide within a global window of 10 slices. The obtained histogram means and RMSs have been converted to equiv. photo-electrons.

6.4 Single Photo-Electron Extraction with the Digital Filter

Figure 35 shows spectra obtained with the digital filter applied on three different global search windows. One can clearly distinguish a pedestal peak (fitted to Gaussian with index 0) and further, positive contributions.

Because the background is determined by the single photo-electrons from the night-sky background, the following possibilities can occur:

1. There is no "signal" (photo-electron) in the extraction window and the extractor finds only electronic noise. Usually, the returned signal charge is then negative.
2. There is one photo-electron in the extraction window and the extractor finds it.
3. There are more than one photo-electron in the extraction window, but separated by more than two FADC slices whereupon the extractor finds the one with the highest charge (upward fluctuation) of both.
4. The extractor finds an overlap of two or more photo-electrons.

Although the probability to find a certain number of photo-electrons in a fixed window follows a Poisson distribution, the one for employing the sliding window is *not* Poissonian. The extractor will usually find one photo-electron even if more are present in the global search window, i.e. the probability for two or more photo-electrons to occur in the global search window is much higher than the probability for these photo-electrons to overlap in time such as to be recognized as a double or triple photo-electron pulse by the extractor. This is especially true for small extraction windows and for the digital filter.

Given a global extraction window of size WS and an average rate of photo-electrons from the night-sky background R, we will now calculate the probability for the extractor to find zero photo-electrons in the WS. The probability to find any number of k photo-electrons can be written as:

$$P(k) = \frac{e^{-R \cdot WS}(R \cdot WS)^k}{k!} \tag{33}$$

and thus:

$$P(0) = e^{-R \cdot WS} \tag{34}$$

The probability to find one or more photo-electrons is then:

$$P(>0) = 1 - e^{-R \cdot WS} \tag{35}$$

In figures 35, one can clearly distinguish the pedestal peak (fitted to Gaussian with index 0), corresponding to the case of $P(0)$ and further contributions of $P(1)$ and $P(2)$ (fitted to

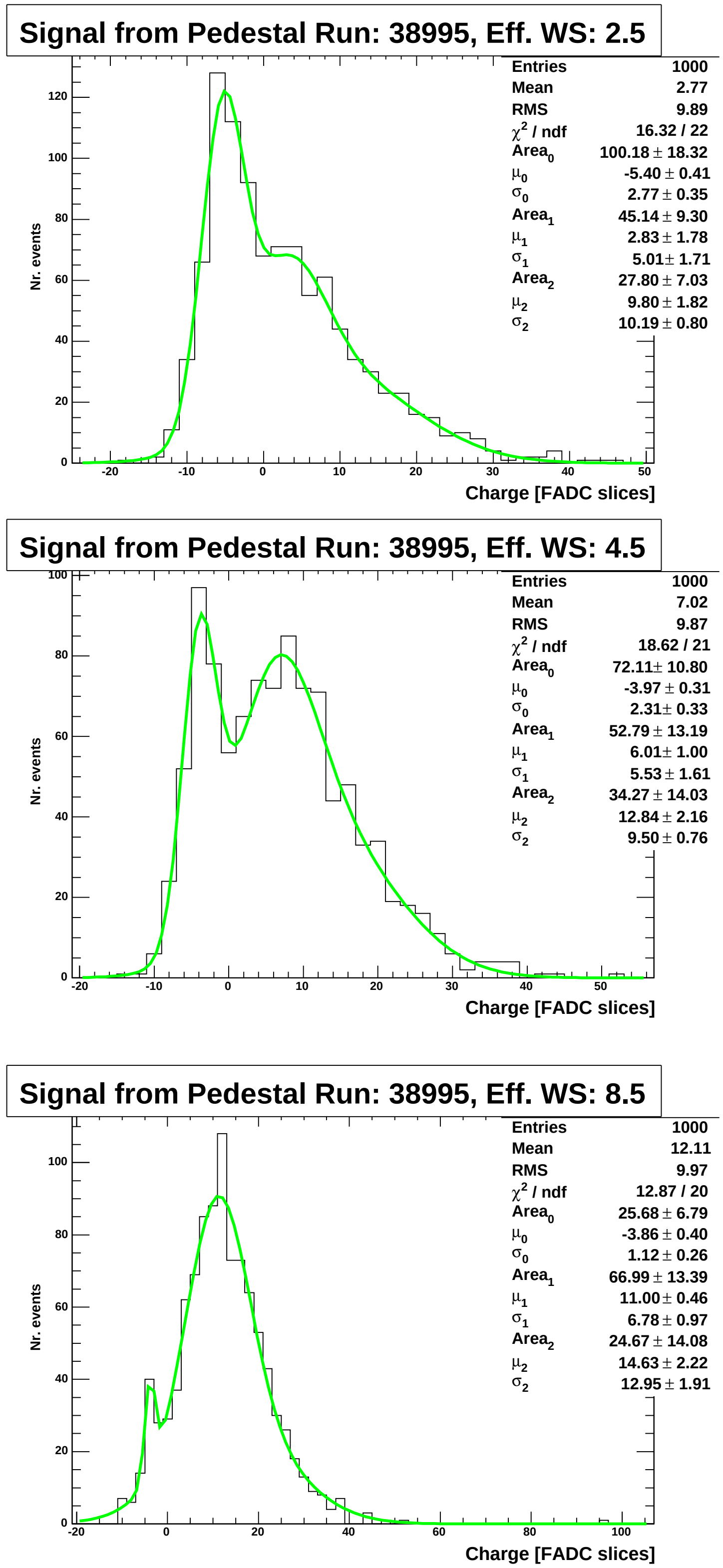

Figure 35: MExtractTimeAndChargeDigitalFilter: Spectrum obtained from the extraction of a pedestal run using a sliding window of 6 FADC slices allowed to move within a window of 7 (top), 9 (center) and 13 slices. A pedestal run with galactic star background has been taken and one typical pixel (Nr. 100). One can clearly see the pedestal contribution and a further part corresponding to one or more photo-electrons.

Gaussians with index 1 and 2). One can also see that the contribution of $P(0)$ dimishes with increasing global search window size.

In the following, we will make a short consistency test: Assuming that the spectral peaks are attributed correctly, one would expect the following relation:

$$P(0)/P(>0) = \frac{e^{-R \cdot WS}}{1 - e^{-R \cdot WS}} \tag{36}$$

We tested this relation assuming that the fitted area underneath the pedestal peak $Area_0$ is proportional to $P(0)$ and the sum of the fitted areas underneath the single photo-electron peak $Area_1$ and the double photo-electron peak $Area_2$ proportional to $P(>0)$. We assumed that the probability for a triple photo-electron to occur is negligible. Thus, one expects:

$$Area_0/(Area_1 + Area_2) = \frac{e^{-R \cdot WS}}{1 - e^{-R \cdot WS}} \tag{37}$$

We estimated the effective window size WS as the sum of the range in which the digital filter amplitude weights are greater than 0.5 (1.5 FADC slices) and the global search window minus the size of the window size of the weights (which is 6 FADC slices). Figure 36 shows the result for two different levels of night-sky background. The fitted rates deliver 0.08 and 0.1 phes/ns, respectively. These rates are about 50% lower than those obtained from the November 2004 test campaign. However, we should take into account that the method is at the limit of distinguishing single photo-electrons. It may occur often that a single photo-electron signal is too low in order to get recognized as such. We tried various pixels and found that some of them do not permit to apply this method at all. The ones which succeed, however, yield about the same fitted rates. To conclude, one may say that there is consistency within the double-peak structure of the pedestal spectrum found by the digital filter which can be explained by the fact that single photo-electrons are separated from the pure electronics noise.

Figure 37 shows the obtained "conversion factors" and "F-Factor" computed as [8]:

$$c_{phe} = \frac{1}{\mu_1 - \mu_0} \tag{38}$$

$$F_{phe} = \sqrt{1 + \frac{\sigma_1^2 - \sigma_0^2}{(\mu_1 - \mu_0)^2}} \tag{39}$$

where μ_0 denotes the mean position of the pedestal peak and μ_1 the mean position of the (assumed) single photo-electron peak. The obtained conversion factors are systematically lower than the ones obtained from the standard calibration and decrease with increasing window size. This is consistent with the assumption that the digital filter finds the most upward fluctuating pulse out of several. Therefore, μ_1 is biased against higher values. The F-Factor is also systematically low (however with huge error bars), which is also consistent with the

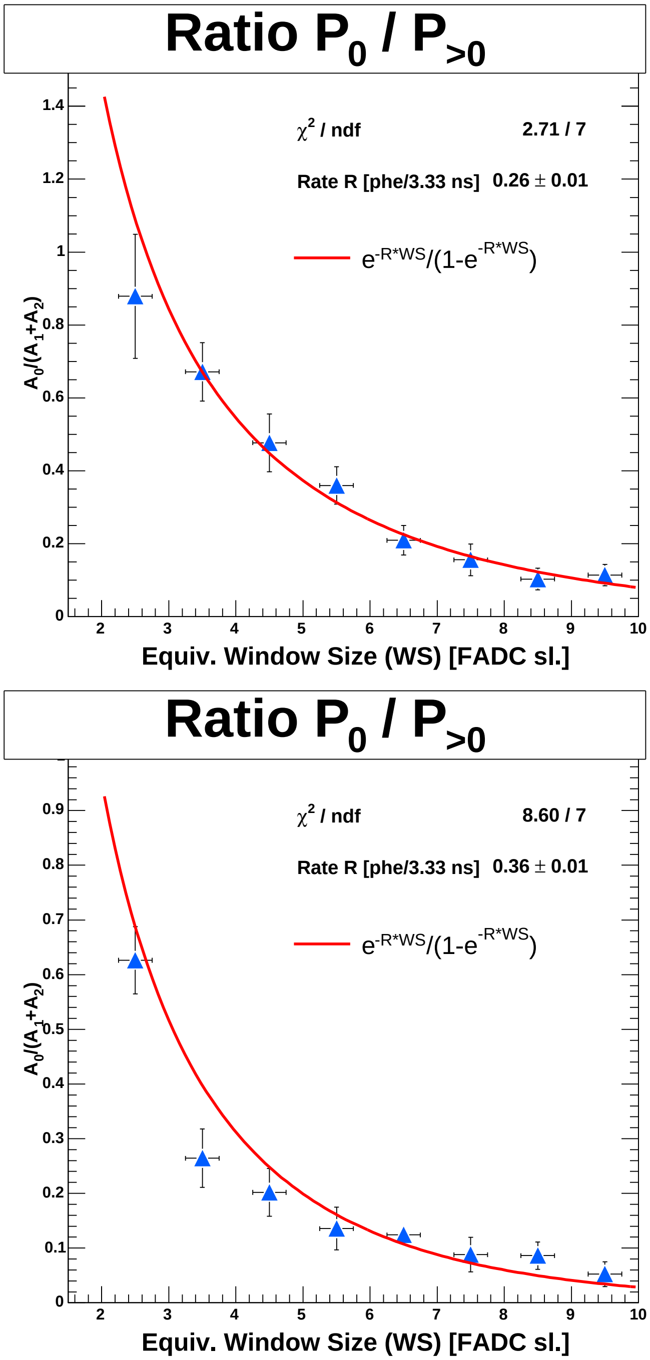

Figure 36: MExtractTimeAndChargeDigitalFilter: Fit to the ratio of the area beneath the pedestal peak and the single and double photo-electron(s) peak(s) with the extraction algorithm applied on a sliding window of different sizes. In the top plot, a pedestal run with extra-galactic star background has been taken and in the bottom, a galactic star background. An typical pixel (Nr. 100) has been used. Above, a rate of 0.08 phe/ns and below, a rate of 0.1 phe/ns has been obtained.

assumption that the spacing between μ_1 and μ_0 is artificially high. Unfortunately, the error bars are too high for a "calibration" of the F-Factor.

In conclusion, the digital filter is at the edge of being able to see single photo-electrons, however a single photo-electron calibration cannot yet be done with the current FADC system because the resolution is too poor. These limitations might be overcome if a higher sampling speed is used and the artificial pulse shaping removed. We expect to improve this method considerably with the new 2 GSamples/s FADC readout of MAGIC.

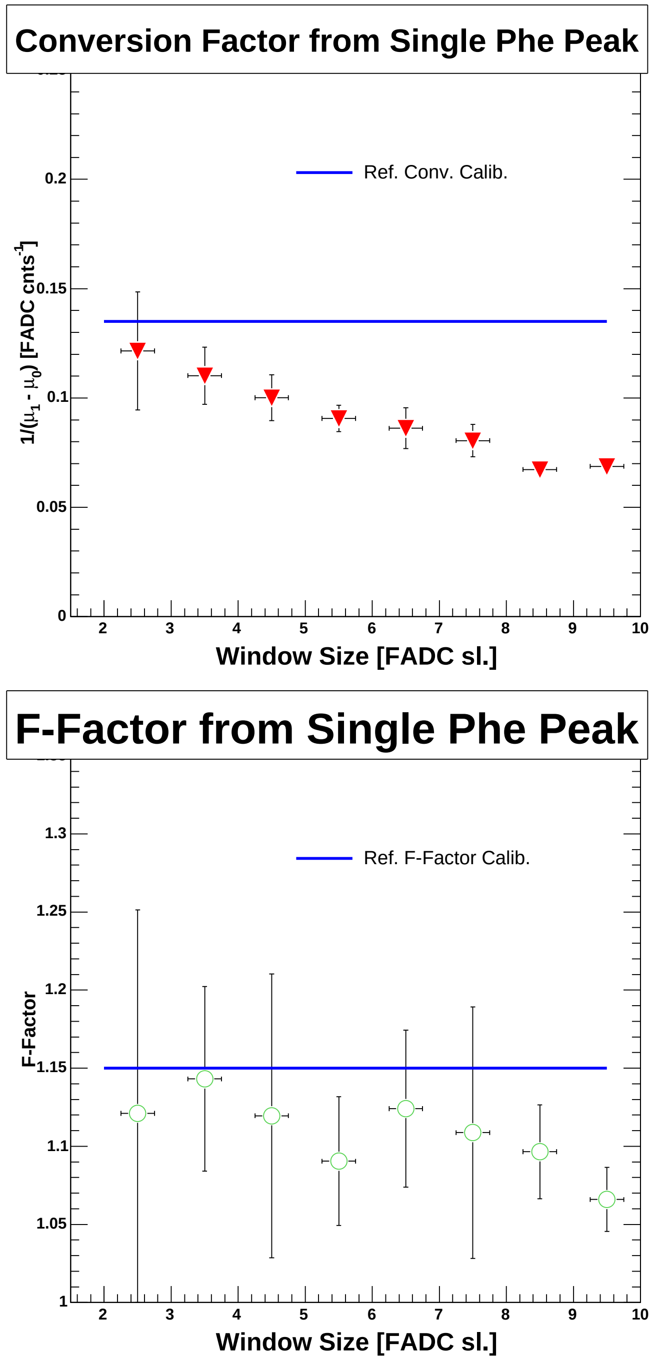

Figure 37: MExtractTimeAndChargeDigitalFilter: Obtained conversion factors (top) and F-Factors (bottom) from the position and width of the fitted Gaussian mean of the single photo-electron peak and the pedestal peak depending on the applied global extraction window sizes. A pedestal run with extra-galactic star background has been taken and an typical pixel (Nr. 100) used. The conversion factor obtained from the standard calibration is shown as a reference line. The obtained conversion factors are systematically lower than the reference one.

7 High-Gain vs. Low-Gain Inter-Calibration

All signals of the MAGIC telescope get split into two branches where one part (the "high-gain" channel) gets amplified by about a factor 10 more than the other part (the "low-gain" channel). Additionally, the low-gain signal gets delayed by 55 ns and obtains thus a different shape due to the limited dynamic range of the passive delay line (see section 1).

In order to combine the signals from both high-gain and low-gain, an inter-calibration is necessary. One can make the following ansatz:

$$\widehat{Q}^N_{HG} = \widehat{Q}^N_{LG} \cdot f^N_A \cdot f_E \ , \tag{40}$$

where $\widehat{Q}^N_{LG}$ is the extracted signal from the low-gain channel N, $\widehat{Q}^N_{HG}$ the equivalent signal the would have been obtained from the high-gain channel N. f^N_A is the (hardware) signal amplification ratio between high-gain and low-gain for channel N. A constant factor f_E comes from possible different normalizations of the signal extractors for both pulse shapes which is independent of the individual readout channel. By selecting events which have both a non-saturation high-gain signal $\widehat{Q}^N_{HG}$ and an extractable low-gain signal $\widehat{Q}^N_{LG}$ and assuming linearity of both the hardware amplification chain and the signal extractor, the proportionality factors $f^N_A \cdot f_E$ can be retrieved for every channel individually and later applied to every extracted low-gain signal:

$$R^N_E = \frac{\widehat{Q}^N_{HG}}{\widehat{Q}^N_{LG}} \equiv f^N_A \cdot f_E \ . \tag{41}$$

The obtained "calibration"-constant R^N_E is in general different for every channel N and for every signal extractor E.

The high-gain vs. low-gain inter-calibration was performed with cosmics data taken in September and December 2004. An event selection was made requiring that the highest FADC slice content is higher than 180 FADC counts, but does not exceed 240 FADC counts. This selection ensures that the signals do not yet saturate the high-gain channel, but are intense enough to trigger the low-gain switch of the electronics. We assumed that the signal reconstruction bias is negligible in any low-gain event above the chosen threshold (see also chapter 5).

Figures 38 show some of the obtained distributions. One can see that the mean conversion factors $< R^N_E >$ are not always centered at the hardware value of 10. The spread over the pixels is about 10% for the sliding window extractor, 8% for the digital filter and even lower for the spline over a low number of FADC slices where it can reach only 6%. Figure 39 shows the distribution of the constants R^N_E over the MAGIC camera. One can clearly distinguish clusters of eight pixels which correspond to one same optical receiver board.

Figure 40 shows the correlation of the amplification ratios obtained with one signal extractor against those obtained with another extractor. Generally, a clear correlation is visible which confirms the assumption that the differences in amplification ratios between different readout channels are mainly due to hardware differences whereas the effect of the signal extractor is

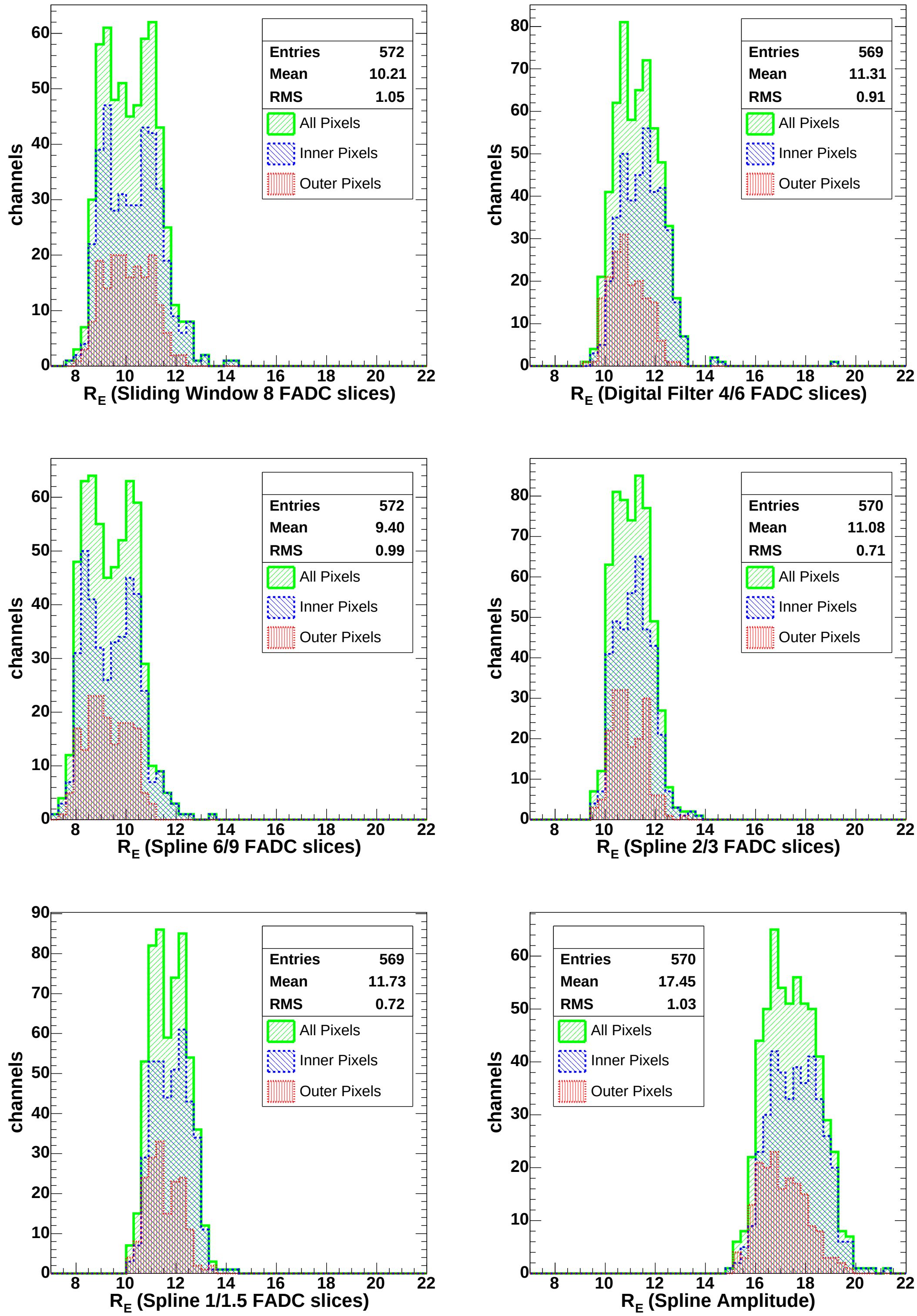

Figure 38: Distributions of the calibrated high-gain vs. low-gain signal ratio, calculated with a sliding window over 8 FADC slices (top left), the digital filter over 4 high-gain and 6 low-gain FADC slices (top right), the spline integrating 6 high-gain and 9 low-gain FADC slices (center left), the spline integrating 2 high-gain and 3 low-gain FADC slices (center right), the spline integrating 1 high-gain and 1.5 low-gain FADC slices (bottom left) and the spline extracting the signal amplitudes (bottom right). Different mean conversion factors are visible, the spread remains equal, however.

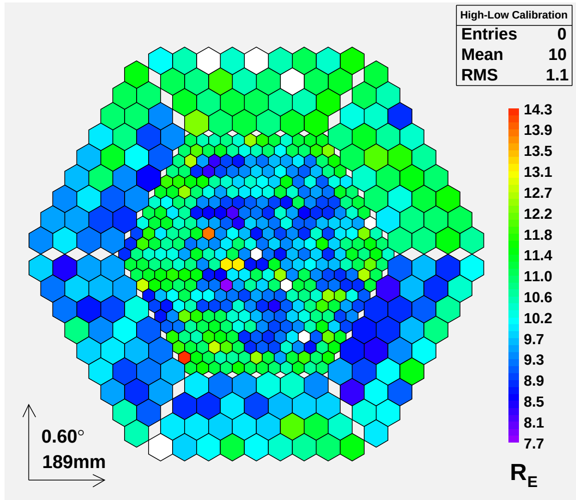

Figure 39: Distributions of the calibrated high-gain vs. low-gain signal ratios R_E, calculated with a sliding window summing 8 high-gain and 8 low-gain FADC slices, displayed in the MAGIC camera. The constants R_E cluster in groups of eight corresponding to the individual optical receiver boards.

constant for all channels. However, there seem to be two classes A and B of signal extractors which produce inter-calibration constants which correlate very well with those obtained from an extractor of the same class and not so well with one of a different class. Table 5 shows which extractors belong to which class:

Classification of Signal Extractors		
Nr.	Name	Class
20	Sliding Window 6/6	A
21	Sliding Window 8/8	A
23	Spline Amplitude	B
24	Spline Integral 1/1.5	B
25	Spline Integral 2/3	B
27	Spline Integral 6/9	A
28	Digital Filter 6/6	B
29	Digital Filter 4/4	B
	Digital Filter 4/6	B

Table 5: The classification of signal extractors with respect to their correlation properties of the high-gain vs. low-gain inter-calibration constants R_E^N. Extractors of a same class produce values of R^N which correlate very well with each other and extractors of a different class do correlate, but show a much bigger spread.

In order to further test equation 40, the following relation is also displayed in figures 40:

$$R_{E_y}^{N_y} = \frac{< R_{E_y} >}{< R_{E_x} >} \cdot R_{E_x}^{N_x} \approx \frac{f_{E_y}}{f_{E_x}} \cdot R_{E_x}^{N_x} \tag{42}$$

One can see that eq. 42 matches the data points well for all extractors of a same cases, but not those obtained with extractors of a different class. The reason for this behaviour of the signal extractors is still not understood.

7.1 Comparison With Results From the Monte Carlo Simulation

Table 6 compares the mean inter-calibration constants $< R_E >$ between the Monte-Carlo simulation results (see figures 23 and 24) to the values obtained from real data in this chapter. One can see that the obtained values of $< R_E >$ are in general considerably higher in the simulation. Only the digital filter coincides more or less if not 4 FADC slices are taken for the low-gain. These differences are not yet understood.

Comparison Inter-Calibration High-gain vs. Low-gain MC and Real Data			
Nr.	Name	$< R_E >$ (MC)	$< R_E >$ (Real)
20	Sliding Window 6/6	11.6	10.4
21	Sliding Window 8/8	11.1	10.2
23	Spline Amplitude	17.6	17.5
24	Spline Integral 1/1.5	12.1	11.8
25	Spline Integral 2/3	11.3	11.1
27	Spline Integral 6/9	10.6	9.4
28	Digital Filter 6/6	11.5	11.5
29	Digital Filter 4/4	12.1	12.8
	Digital Filter 4/6	12.9	11.3

Table 6: The mean high-gain vs. low-gain inter-calibration constants $< R_E >$ for different signal extractors, compared between the Monte Carlo simulation result and real data.

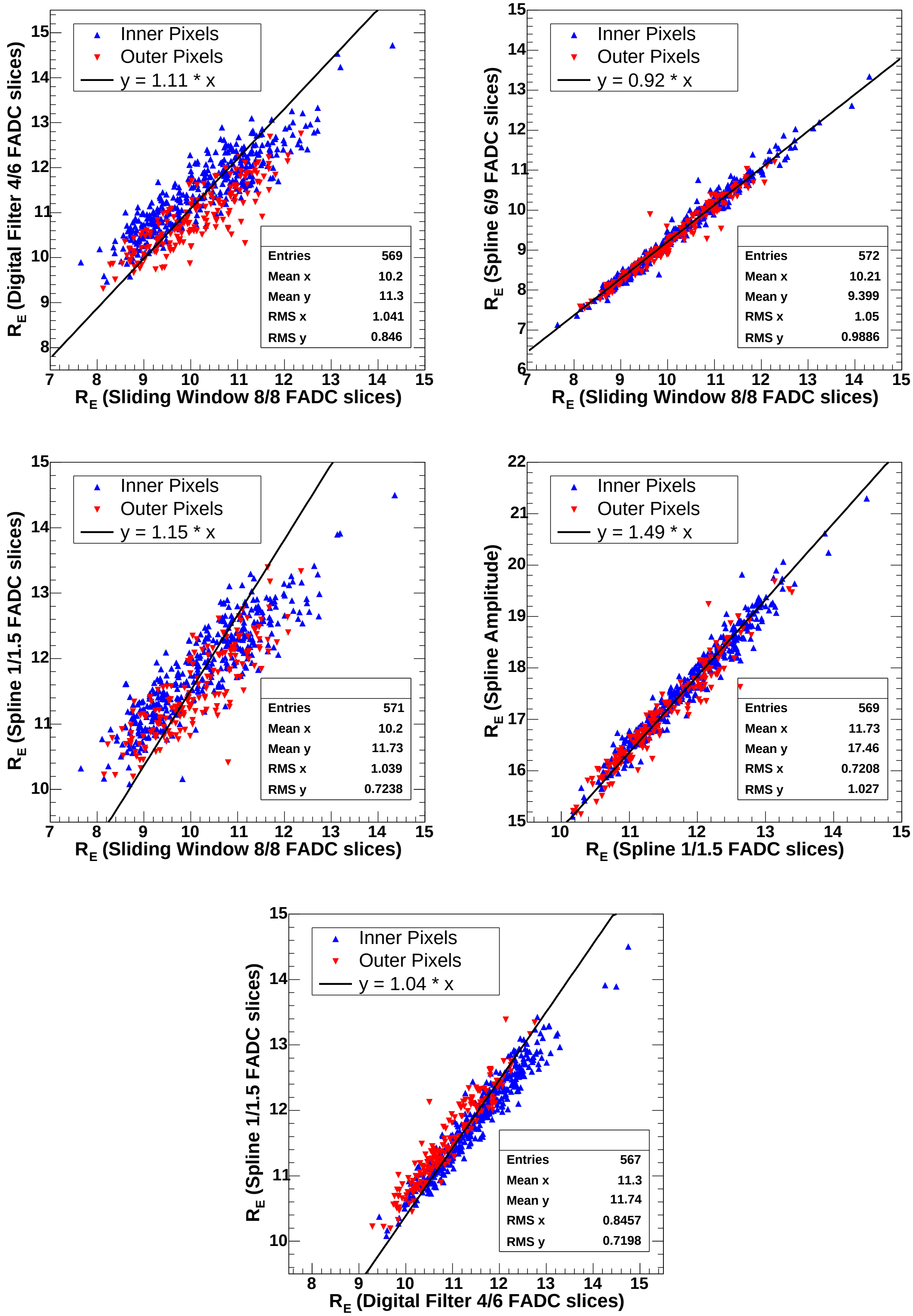

Figure 40: Distributions of the calibrated high-gain vs. low-gain signal ratios R_E, calculated with the digital filter fitting 4 high-gain and 6 low-gain FADC slices, the sliding window summing 8 FADC slices each and the spline integrating 6 high-gain and 9 low-gain FADC slices, 1 high-gain and 1.5 low-gain FADC slices and only the amplitude of spline. The values of R_E, obtained with the five different signal extractors, correlate well. Also equation 42 is displayed.

8 Calibration

In this section, we describe the tests performed using light pulses of different colour, pulse shapes and intensities with the MAGIC LED Calibration Pulser Box [16].

The LED pulser system is able to provide fast light pulses of 2–4 ns FWHM with intensities ranging from 3–4 to more than 600 photo-electrons in one inner photo-multiplier of the camera. These pulses can be produced in three colors **green, blue** and **UV**.

The possible pulsed light colors						
Colour	Wavelength [nm]	Spectral Width [nm]	Min. Nr. Phe's	Max. Nr. Phe's	Secondary Pulses	FWHM Pulse [ns]
Green	520	40	6	120	yes	3–4
Blue	460	30	6	600	yes	3–4
UV	375	12	3	50	no	2–3

Table 7: The pulser colors available from the calibration system

Table 7 lists the available colors and intensities and figures 41 and 42 show typical pulses as registered by the FADCs. Whereas the UV-pulse is rather stable, the green and blue pulses can show smaller secondary pulses after about 10–40 ns from the main pulse. One can see that the stable UV-pulses are unfortunately only available in such intensities as to not saturate the high-gain readout channel. However, the brightest combination of light pulses easily saturates all channels in the camera, but does not reach a saturation of the low-gain readout.

Our tests can be classified into three subsections:

1. Un-calibrated pixels and events: These tests measure the percentage of failures of the extractor resulting either in a pixel declared as un-calibrated or in an event which produces a signal outside of the expected Gaussian distribution.

2. Number of photo-electrons: These tests measure the reconstructed numbers of photo-electrons, their spread over the camera and the ratio of the obtained mean values for outer and inner pixels, respectively.

3. Linearity tests: These tests measure the linearity of the extractor with respect to pulses of different intensity and colour.

4. Time resolution: These tests show the time resolution and stability obtained with different intensities and colors.

We used data taken on the 7$^{\text{th}}$ of June, 2004 with different pulser LED combinations, each taken with 16384 events. 19 different calibration configurations have been tested. The corresponding MAGIC data run numbers range from nr. 31741 to 31772. These data have been taken before the latest camera repair access which resulted in a replacement of about 2% of the pixels known to be mal-functioning at that time. There is thus a lower limit to the number of un-calibrated pixels of about 1.5–2% of known mal-functioning photo-multipliers.

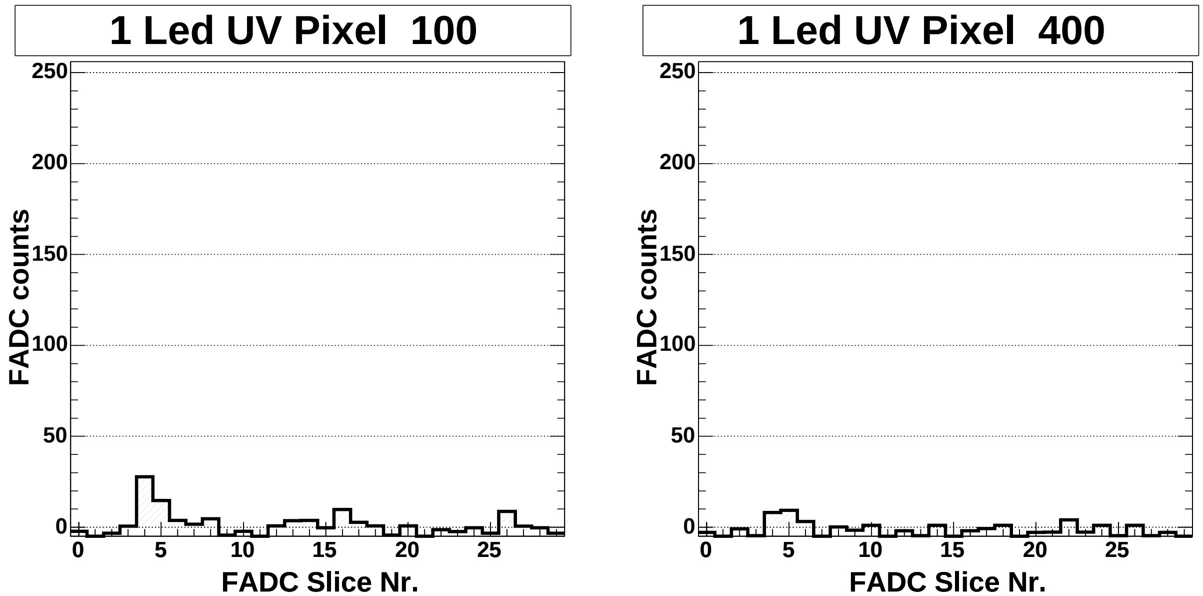

Figure 41: Example of a calibration pulse from the lowest available intensity (1 Led UV). The left plot shows the signal obtained in an inner pixel, the right one the signal in an outer pixel. Note that the pulse height fluctuates much more than suggested from these pictures. Especially, a zero-pulse is also possible.

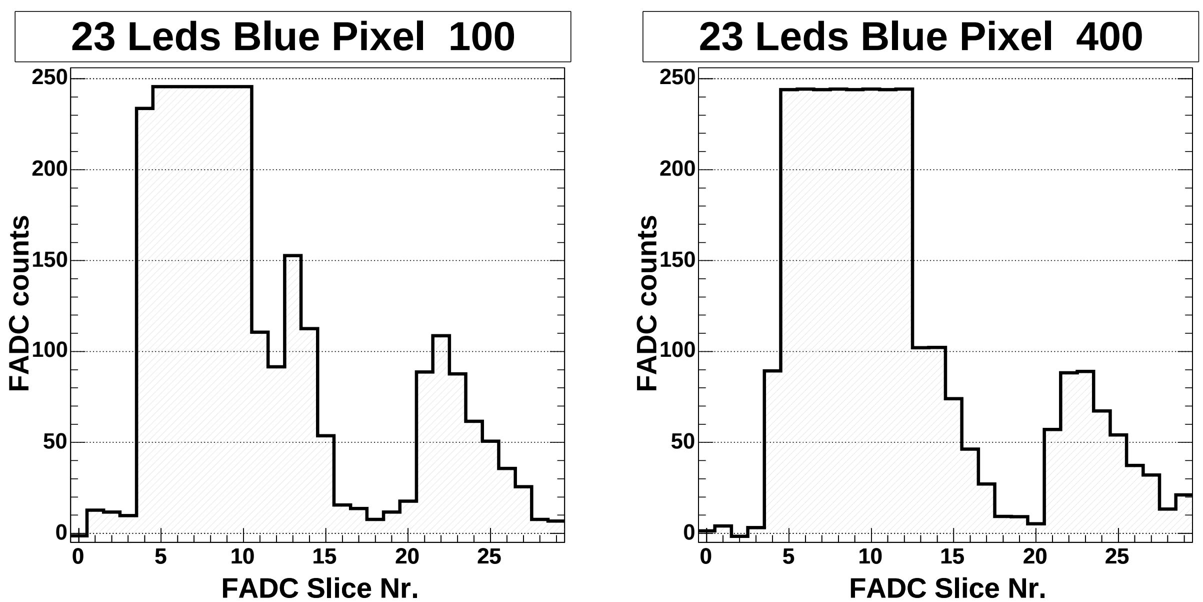

Figure 42: Example of a calibration pulse from the highest available mono-chromatic intensity (23 Leds Blue). The left plot shows the signal obtained in an inner pixel, the right one the signal in an outer pixel. One the left side of both plots, the (saturated) high-gain channel is visible, on the right side from FADC slice 18 on, the delayed low-gain pulse appears. Note that in the left plot, there is a secondary pulses visible in the tail of the high-gain pulse.

Although we had looked at and tested all colour and extractor combinations resulting from these data, we restrict ourselves to show here only typical behaviour and results of extractors. All plots, including those which are not displayed in this TDAS, can be retrieved from the following locations:

http://www.magic.ifae.es/~markus/pheplots/
http://www.magic.ifae.es/~markus/timeplots/

8.1 Un-Calibrated Pixels and Events

The MAGIC calibration software incorporates a series of checks to sort out mal-functioning pixels. Except for the software bug searching criteria, the following exclusion criteria can apply:

1. The reconstructed mean signal $\widehat{Q}$ is less than 2.5 times the extractor resolution R: $\widehat{Q} < 2.5 \cdot R$. (2.5 Pedestal RMS in the case of the simple fixed window extractors, see section 6). This criterium essentially cuts out dead pixels.

2. The error of the mean reconstructed signal $\delta\widehat{Q}$ is larger than the mean reconstructed signal $\widehat{Q}$: $\delta\widehat{Q} > \widehat{Q}$. This criterion cuts out signal distributions which fluctuate so much that their RMS is bigger than its mean value. This criterium cuts out "ringing" pixels or mal-functioning extractors.

3. The reconstructed mean number of photo-electrons lies 4.5 sigma outside the distribution of photo-electrons obtained with the inner or outer pixels in the camera, respectively. This criterium cuts out channels with apparently deviating (hardware) behaviour compared to the rest of the camera readout[10].

4. All pixels with reconstructed negative mean signal or with a mean numbers of photo-electrons smaller than one. Pixels with a negative pedestal RMS subtracted sigma occur, especially when stars are focused onto that pixel during the pedestal run (resulting in a large pedestal RMS), but have moved to another pixel during the calibration run. In this case, the number of photo-electrons would result artificially negative. If these channels do not show any other deviating behaviour, their number of photo-electrons gets replaced by the mean number of photo-electrons in the camera, and the channel is further calibrated as normal.

Moreover, the number of events are counted which have been reconstructed outside a 5σ region from the mean signal $< \widehat{Q} >$. These events are called "outliers". Figure 43 shows a typical outlier obtained with the digital filter applied on a low-gain signal, and figure 44 shows the average number of all excluded pixels and outliers obtained from all 19 calibration configurations. One can already see that the largest window sizes yield a high number of un-calibrated pixels, mostly due to the missing ability to recognize the low-intensity pulses (see later). One can also

[10]This criteria is not applied any more in the standard analysis, although we kept using it here

see that the amplitude extracting spline yields a higher number of outliers than the rest of the extractors.

The global champion in lowest number of un-calibrated pixels results to be **MExtractTime-AndChargeSpline** extracting the integral over two FADC slices (extractor #25). The one with the lowest number of outliers is **MExtractFixedWindowPeakSearch** with an extraction range of 2 slices (extractor #11).

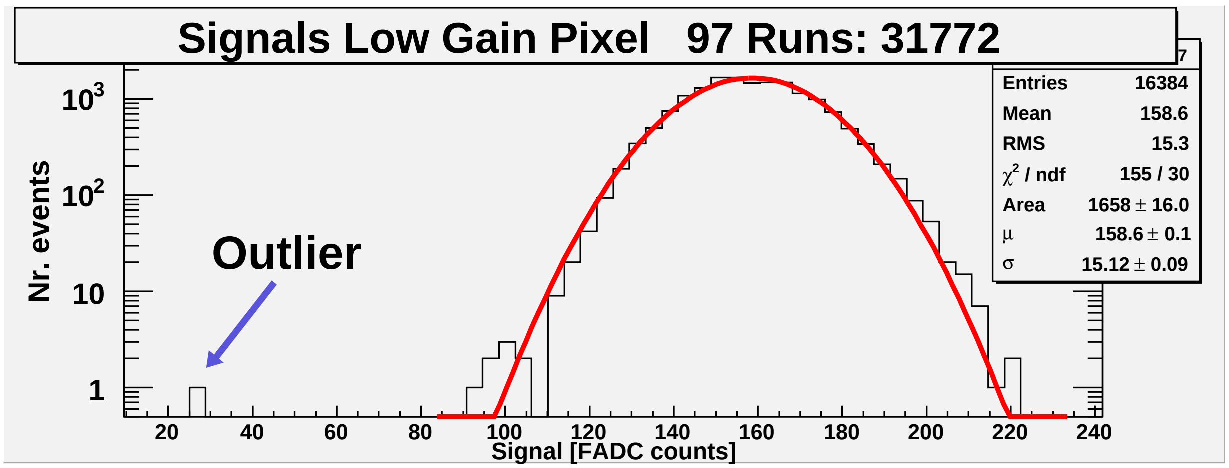

Figure 43: Example of an event classified as "outlier". The histogram has been obtained using the digital filter (extractor #32) applied to a high-intensity blue pulse (run 31772). The event marked as "outlier" clearly has been mis-reconstructed. It lies outside the 5σ–region from the fitted mean.

The following figures 45, 46, 47 and 48 show the resulting numbers of un-calibrated pixels and events for different colors and intensities. Because there is a strong anti-correlation between the number of excluded pixels and the number of outliers per event, we have chosen to show these numbers together.

One can see that in general, big extraction windows raise the number of un-calibrated pixels and are thus less stable. Especially for the very low-intensity **1 Led UV**-pulse, the big extraction windows – summing 8 or more slices – cannot calibrate more than 50% of the inner pixels (fig. 46). This is an expected behavior since big windows sum up more noise which in turn makes the search for the small signal more difficult.

In general, one can also find that all "sliding window"-algorithms (extractors #17-32) discard less pixels than the corresponding "fixed window"-ones (extractors #1–16).

The spline (extractors #23–27) and the digital filter with the correct weights (extractors #30-31) discard the least number of pixels and are also robust against slight modifications of the pulse form (of the weights for the digital filter).

Concerning the numbers of outliers, one can conclude that in general, the numbers are very low never exceeding 0.1% except for the amplitude-extracting spline which seems to mis-reconstruct a certain type of events.

In conclusion, already this first test excludes all extractors with too large window sizes because they are not able to extract cleanly small signals produced by about 4 photo-electrons. Moreover, the amplitude extracting spline produces a significantly higher number of outlier

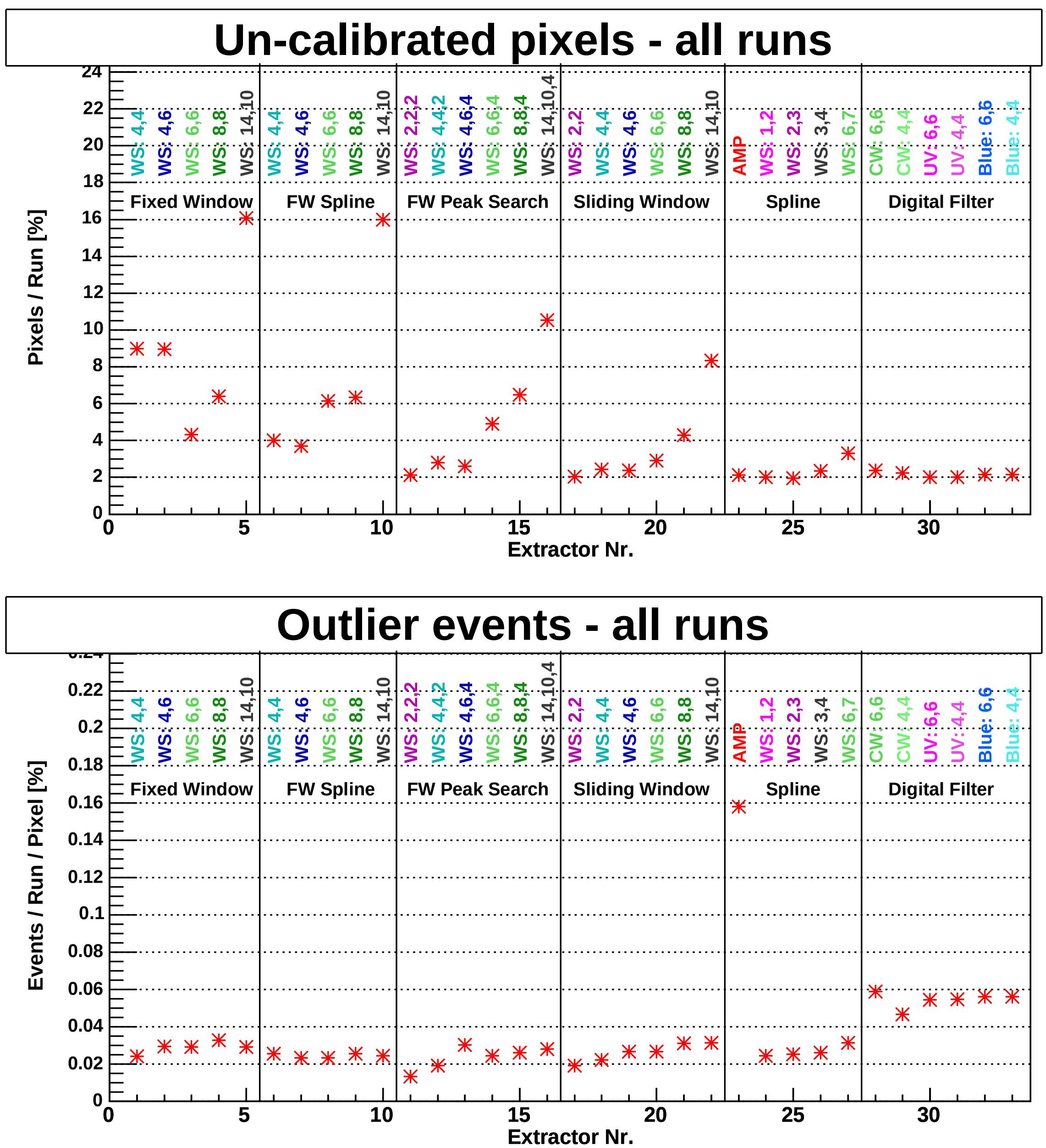

Figure 44: Un-calibrated pixels and outlier events averaged over all available calibration runs.

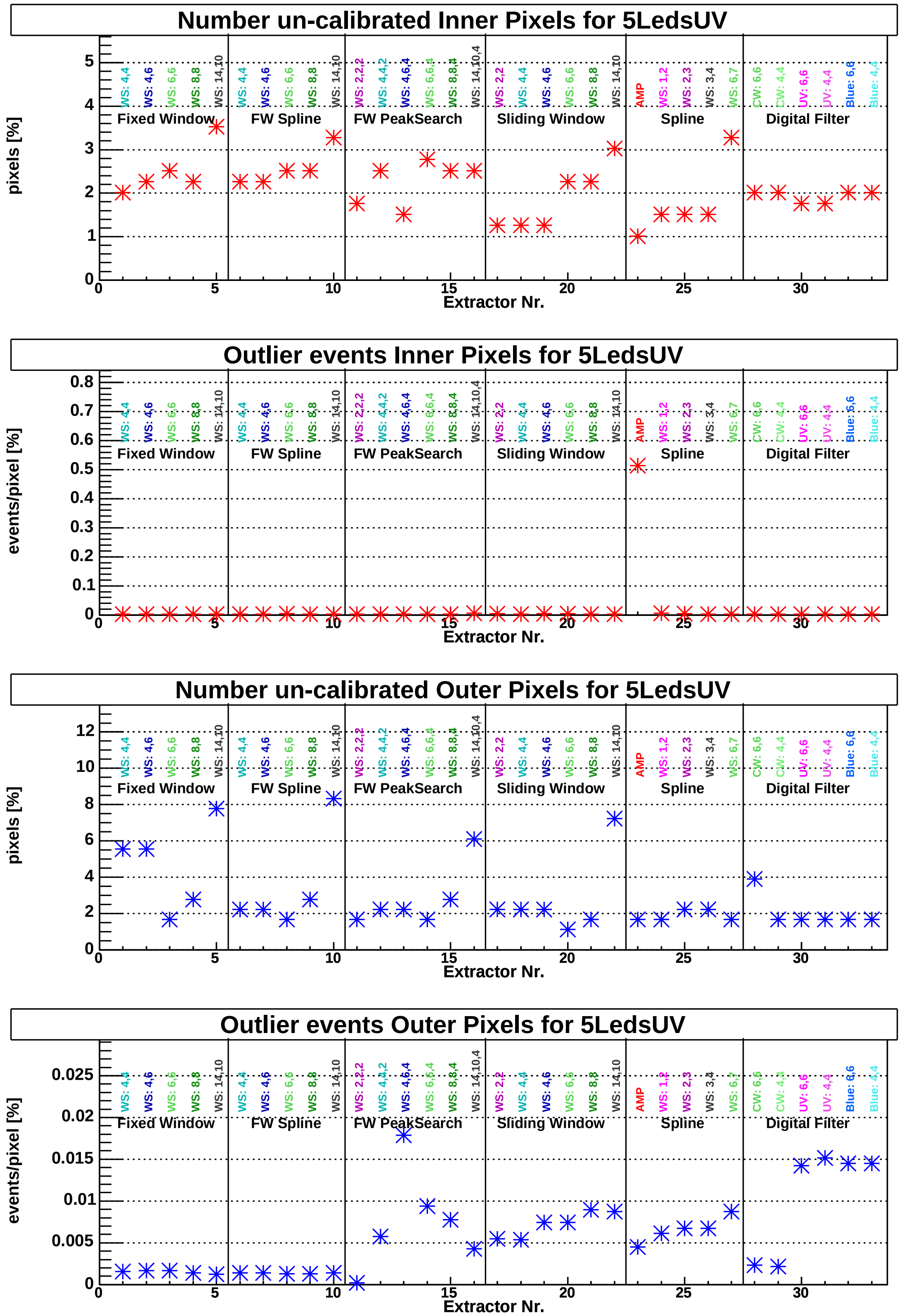

Figure 45: Un-calibrated pixels and outlier events for a typical calibration pulse of UV-light which does not saturate the high-gain readout.

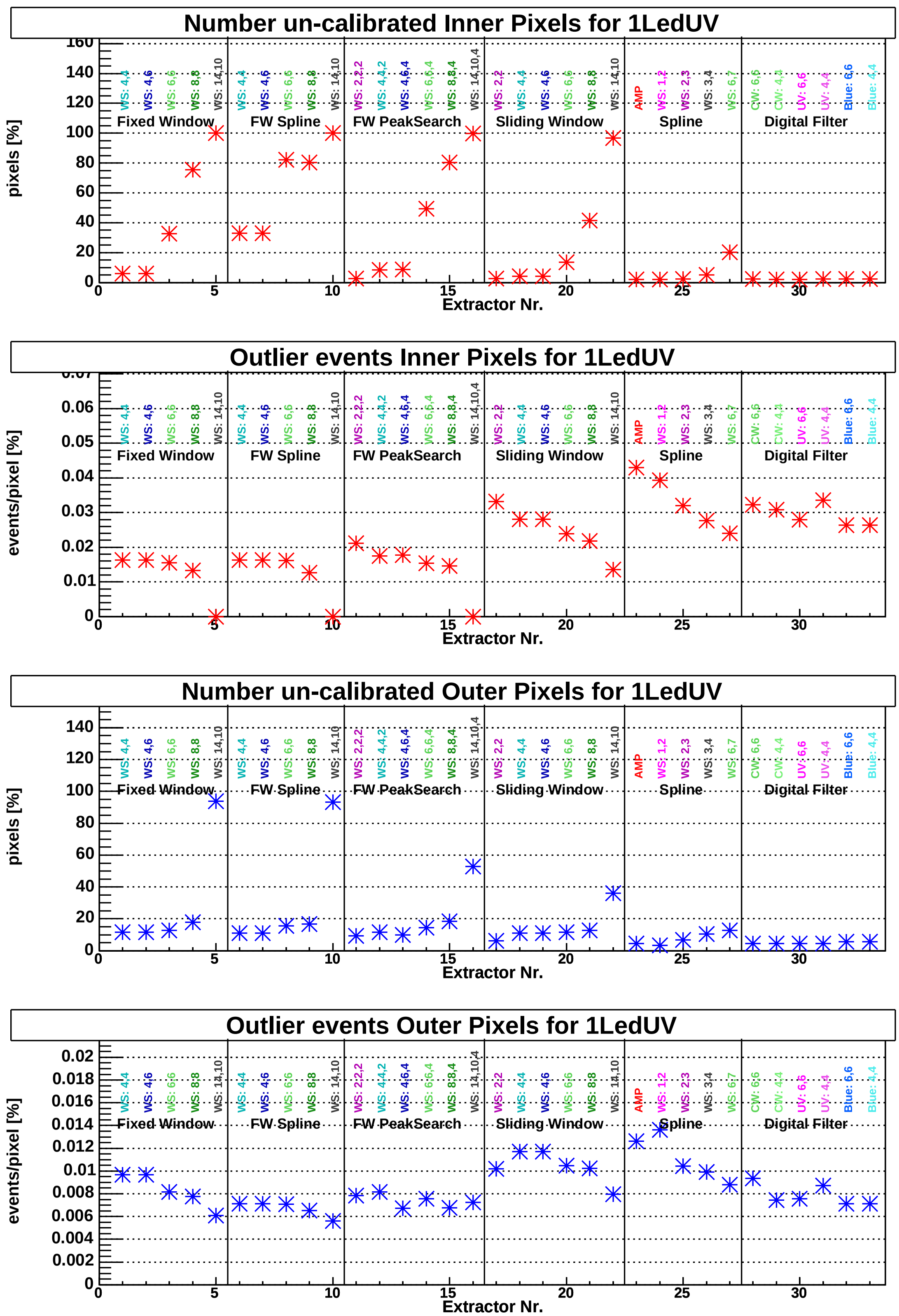

Figure 46: Un-calibrated pixels and outlier events for a very low intensity pulse.

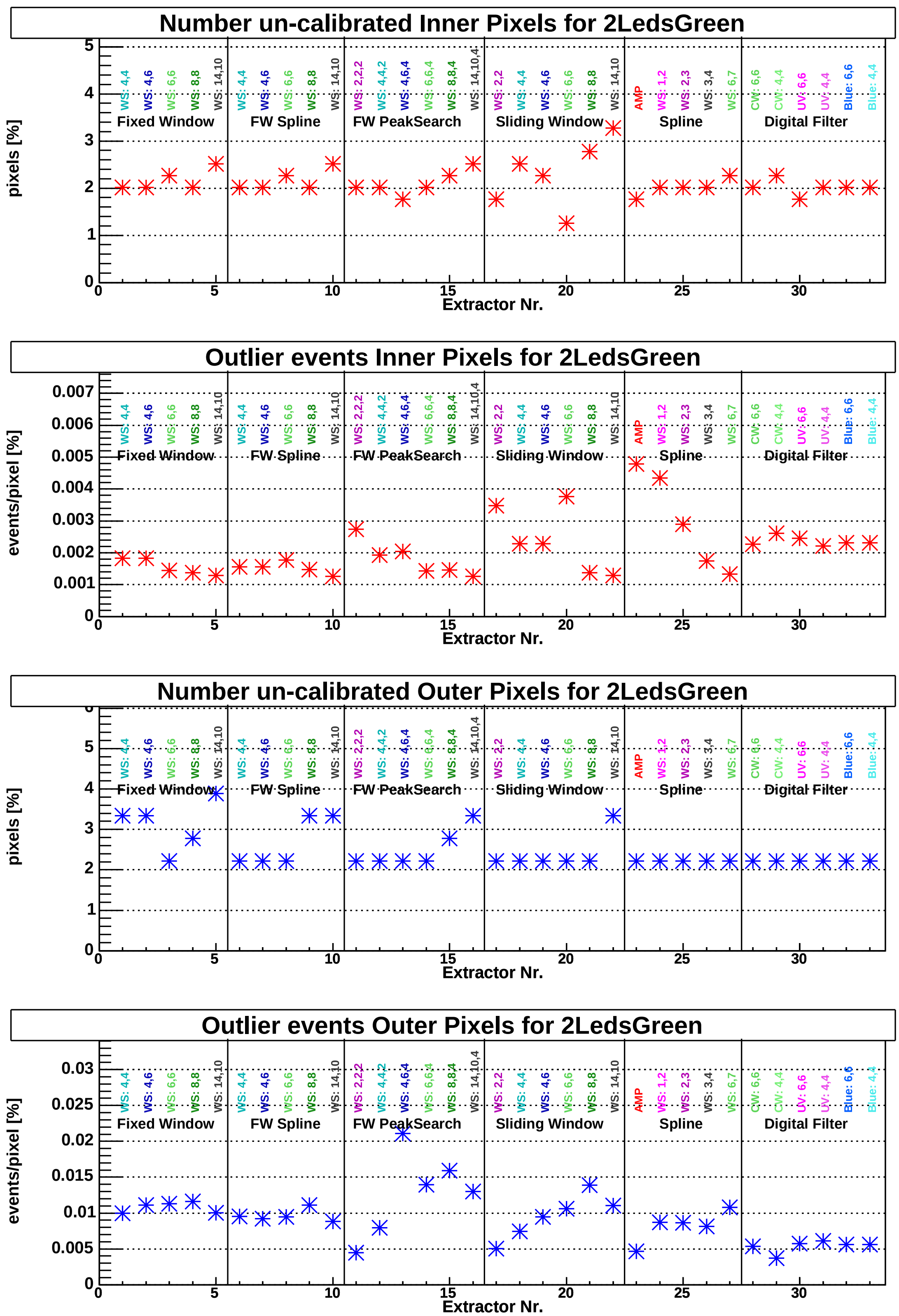

Figure 47: Un-calibrated pixels and outlier events for a typical green pulse.

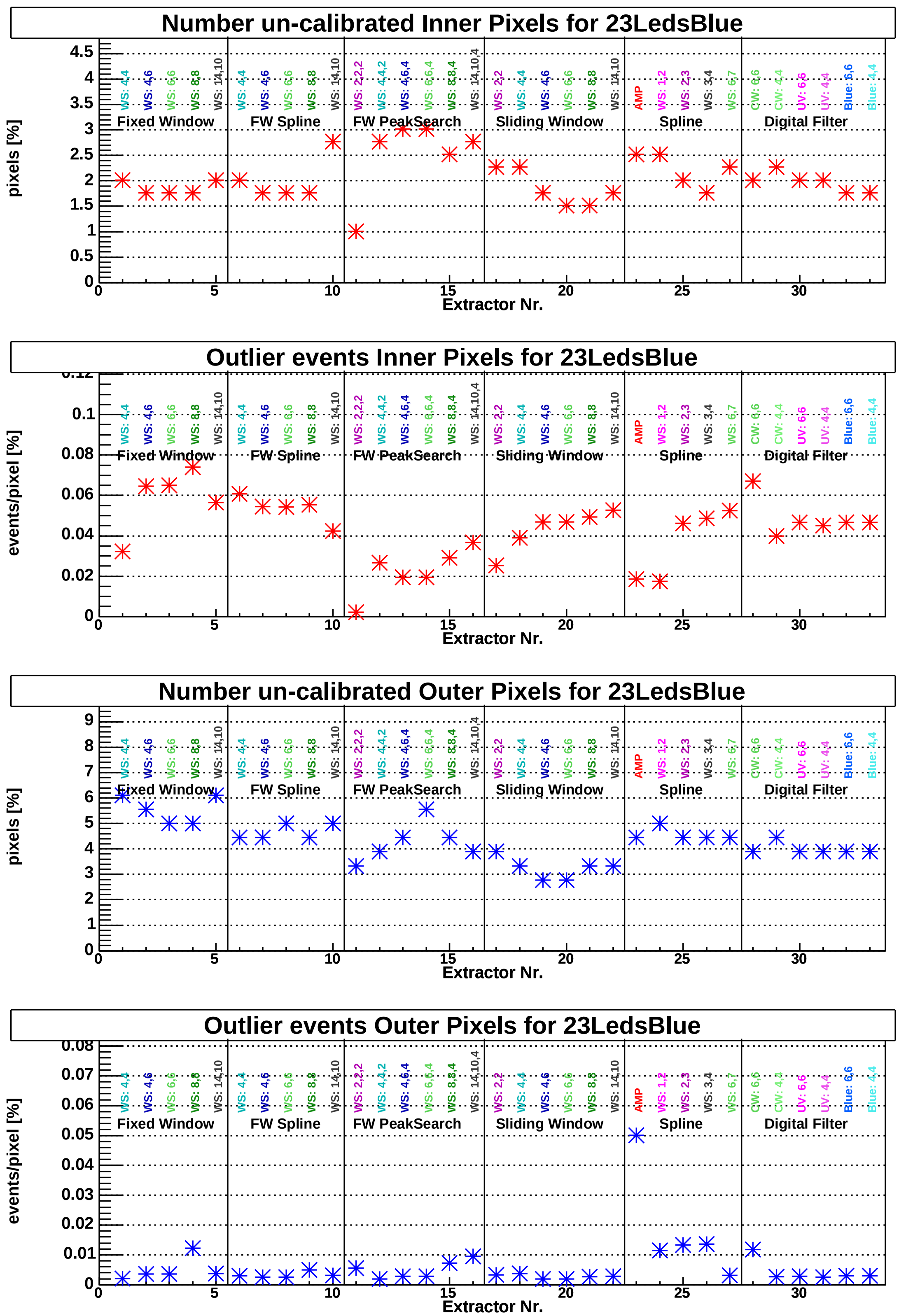

Figure 48: Un-calibrated pixels and outlier events for a high-intensity blue pulse.

events.

8.2 Number of Photo-Electrons

Assuming that the readout chain adds only negligible noise to the one introduced by the photo-multiplier itself, one can make the assumption that the variance of the true signal, S, is the amplified Poisson variance of the number of photo-electrons, multiplied with the excess noise of the photo-multiplier which itself is characterized by the excess-noise factor F:

$$Var[S] = F^2 \cdot Var[N_{phe}] \cdot \frac{< S >^2}{< N_{phe} >^2} \tag{43}$$

After introducing the effect of the night-sky background (eq. 31) and assuming that the variance of the number of photo-electrons is equal to the mean number of photo-electrons (because of the Poisson distribution), one obtains an expression to retrieve the mean number of photo-electrons released at the photo-multiplier cathode from the mean extracted signal, $\widehat{S}$, and the RMS of the extracted signal obtained from pure pedestal runs R (see section 6.2):

$$< N_{phe} > \approx F^2 \cdot \frac{< \widehat{S} >^2}{Var[\widehat{S}] - R^2} \tag{44}$$

In theory, eq. 44 must not depend on the extractor! Effectively, we will use it to test the quality of our extractors by requiring that a valid extractor yields the same number of photo-electrons for all pixels individually and does not deviate from the number obtained with other extractors. As the camera is flat-fielded, but the number of photo-electrons impinging on an inner and an outer pixel is different, we also use the ratio of the mean numbers of photo-electrons from the outer pixels to the one obtained from the inner pixels as a test variable. In the ideal case, it should always yield its central value of about 2.6±0.1 [17].

In our case, there is an additional complication due to the fact that the green and blue colored light pulses show secondary pulses which destroy the Poisson behaviour of the number of photo-electrons. We will have to split our sample of extractors into those being affected by the secondary pulses and those being immune to this effect.

Figures 49, 50, 51 and 52 show some of the obtained results. One can see a rather good stability for the standard **5 Leds UV** pulse, except for the extractors **MExtractFixedWindowPeak-Search**, initialized with an extraction window of 2 slices.

There is a considerable difference for all shown non-standard pulses. Especially the pulses from green and blue LEDs show a clear dependence of the number of photo-electrons on the extraction window. Only the largest extraction windows seem to catch the entire range of (jittering) secondary pulses and get the ratio of outer vs. inner pixels right. However, they (obviously) over-estimate the number of photo-electrons in the primary pulse.

The strongest discrepancy is observed in the low-gain extraction (fig. 52) where all fixed window extractors with extraction windows smaller than 8 FADC slices fail to reconstruct the correct numbers. This has to do with the fact that the fixed window extractors fail to catch a significant part of the (larger) pulse because of the 1 FADC slice event-to-event jitter and the larger pulse width covering about 6 FADC slices. Also the sliding windows smaller than 6 FADC slices and the spline smaller than 2 FADC slices reproduce too small numbers of photo-electrons. Moreover, the digital filter shows a small dependency of the number of photo-electrons w.r.t. the extraction window.

One can see that all extractors using a large window belong to the class of extractors being affected by the secondary pulses, except for the digital filter.

The extractor **MExtractTimeAndChargeDigitalFilter** seems to be sufficiently stable against modifications of the exact form of the weights in the high-gain readout channel since all applied weights yield about the same number of photo-electrons and the same ratio of outer vs. inner pixels.

All sliding window and spline algorithms yield a stable ratio of outer vs. inner pixels in the high and the low-gain.

Concluding, there is no fixed window extractor yielding always the correct number of photo-electrons, except for the extraction window of 8 FADC slices. Either the number of photo-electrons itself is wrong or the ratio of outer vs. inner pixels is not correct. All sliding window algorithms seem to reproduce the correct numbers if one takes into account the after-pulse behaviour of the light pulser itself. The digital filter seems to be stable against modifications of the intrinsic pulse width from 1 to 4 ns. This is the expected range within which the pulses from realistic cosmics signals may vary.

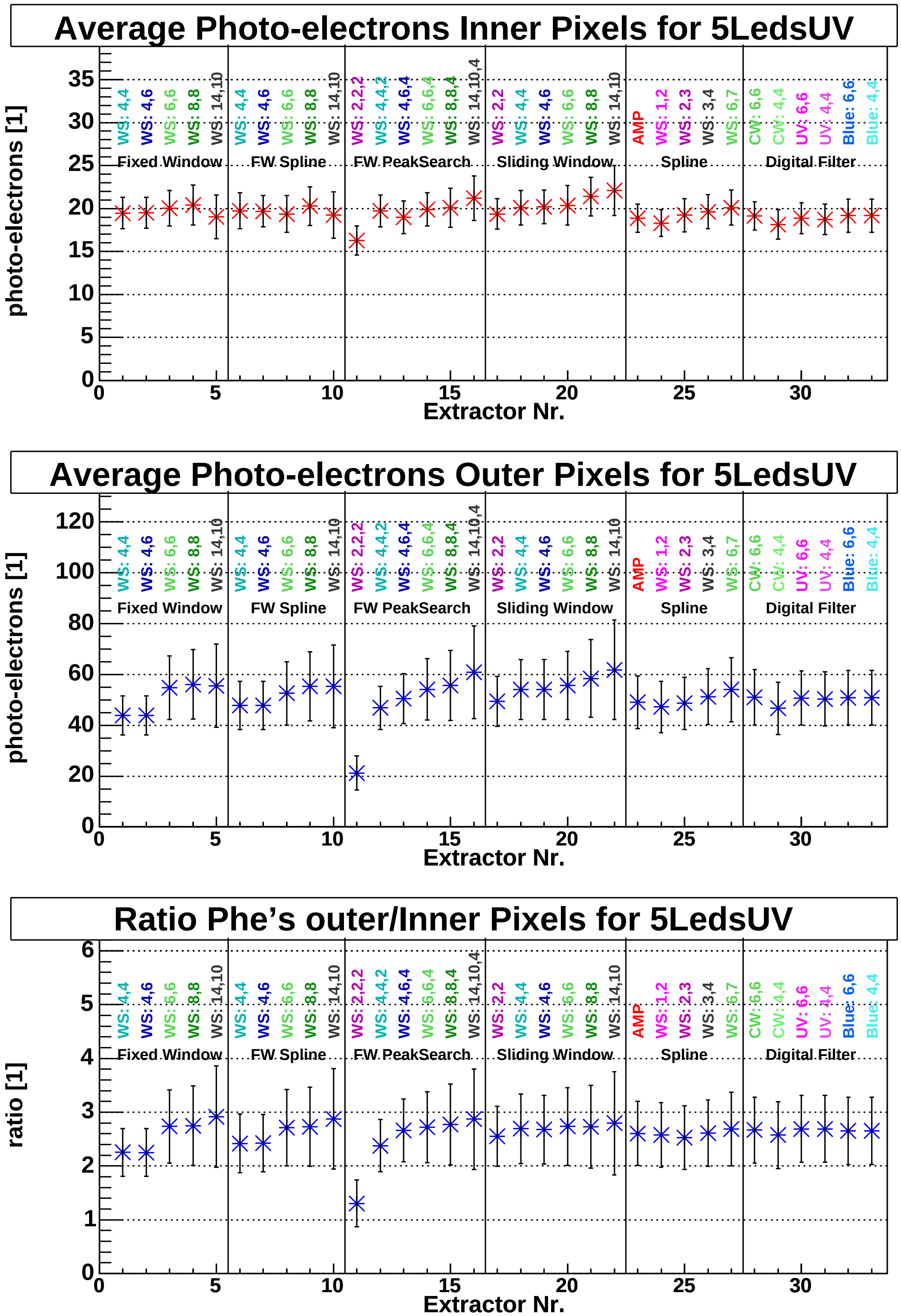

Figure 49: Number of photo-electrons from a typical, not saturating calibration pulse of colour UV, reconstructed with each of the tested signal extractors. The first plots shows the number of photo-electrons obtained for the inner pixels, the second one for the outer pixels and the third shows the ratio of the mean number of photo-electrons for the outer pixels divided by the mean number of photo-electrons for the inner pixels. Points denote the mean of all not-excluded pixels, the error bars their RMS.

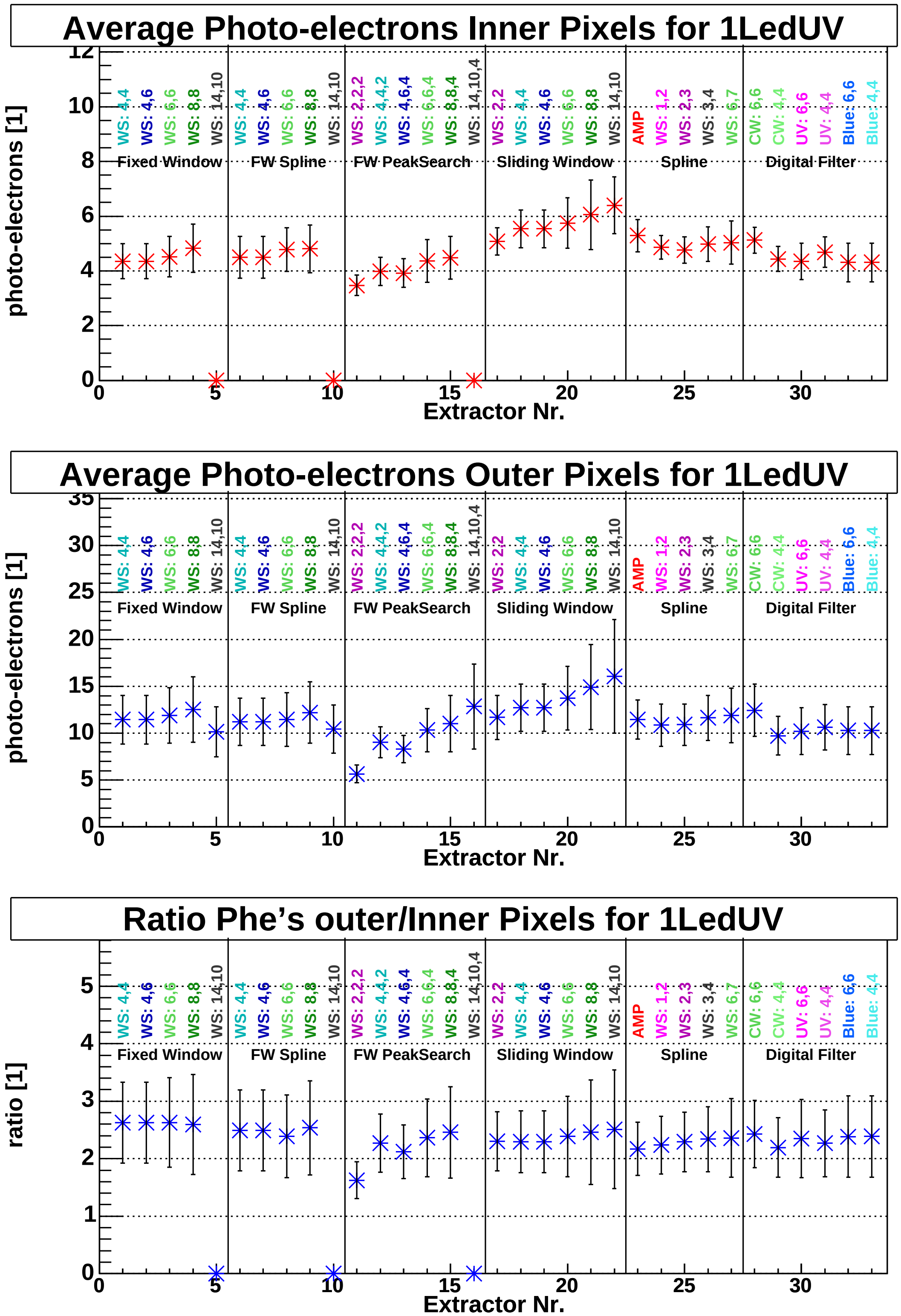

Figure 50: Number of photo-electrons from a typical, very low-intensity calibration pulse of colour UV, reconstructed with each of the tested signal extractors. The first plots shows the number of photo-electrons obtained for the inner pixels, the second one for the outer pixels and the third shows the ratio of the mean number of photo-electrons for the outer pixels divided by the mean number of photo-electrons for the inner pixels. Points denote the mean of all not-excluded pixels, the error bars their RMS.

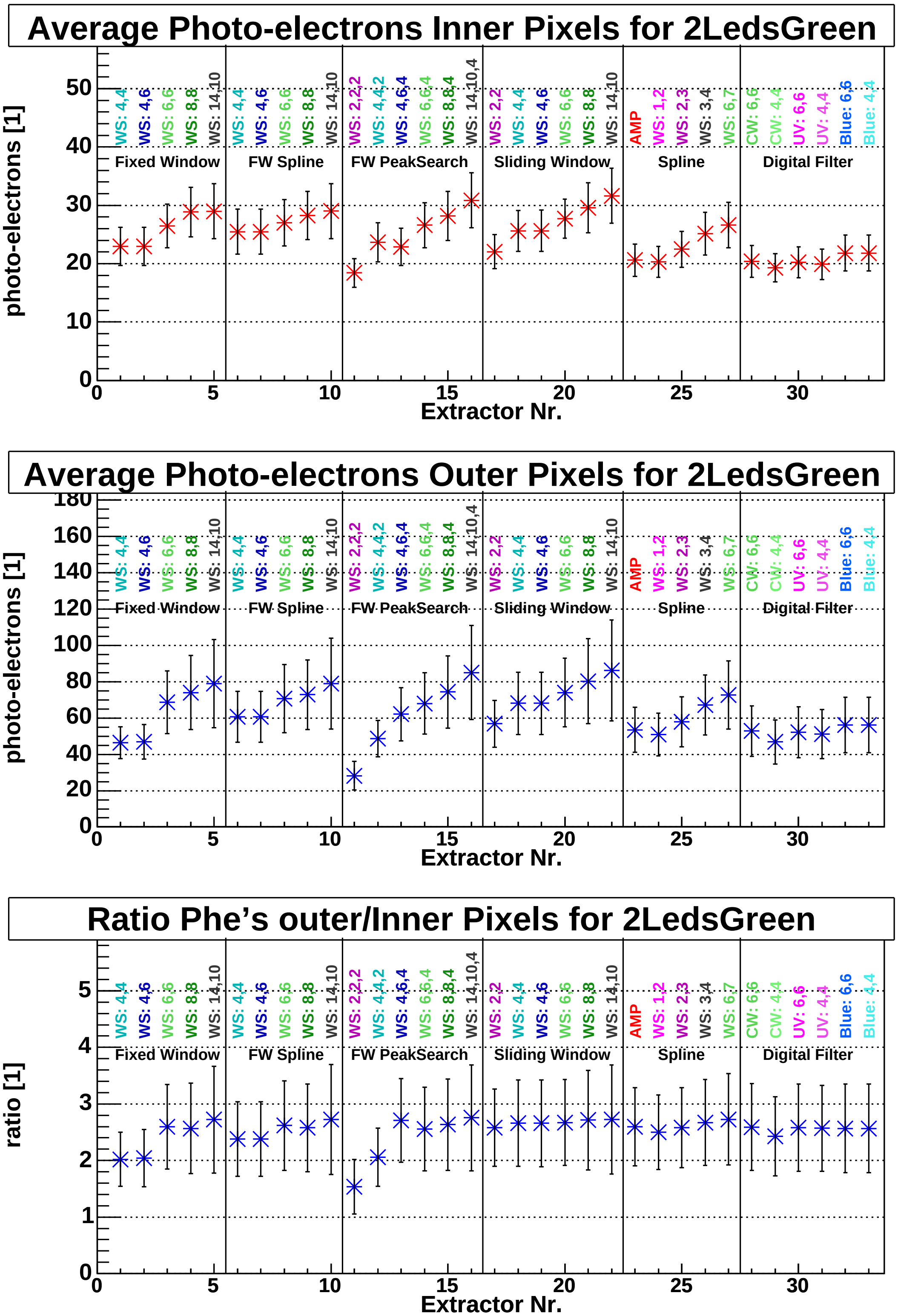

Figure 51: Number of photo-electrons from a typical, not saturating calibration pulse of colour green, reconstructed with each of the tested signal extractors. The first plots shows the number of photo-electrons obtained for the inner pixels, the second one for the outer pixels and the third shows the ratio of the mean number of photo-electrons for the outer pixels divided by the mean number of photo-electrons for the inner pixels. Points denote the mean of all not-excluded pixels, the error bars their RMS.

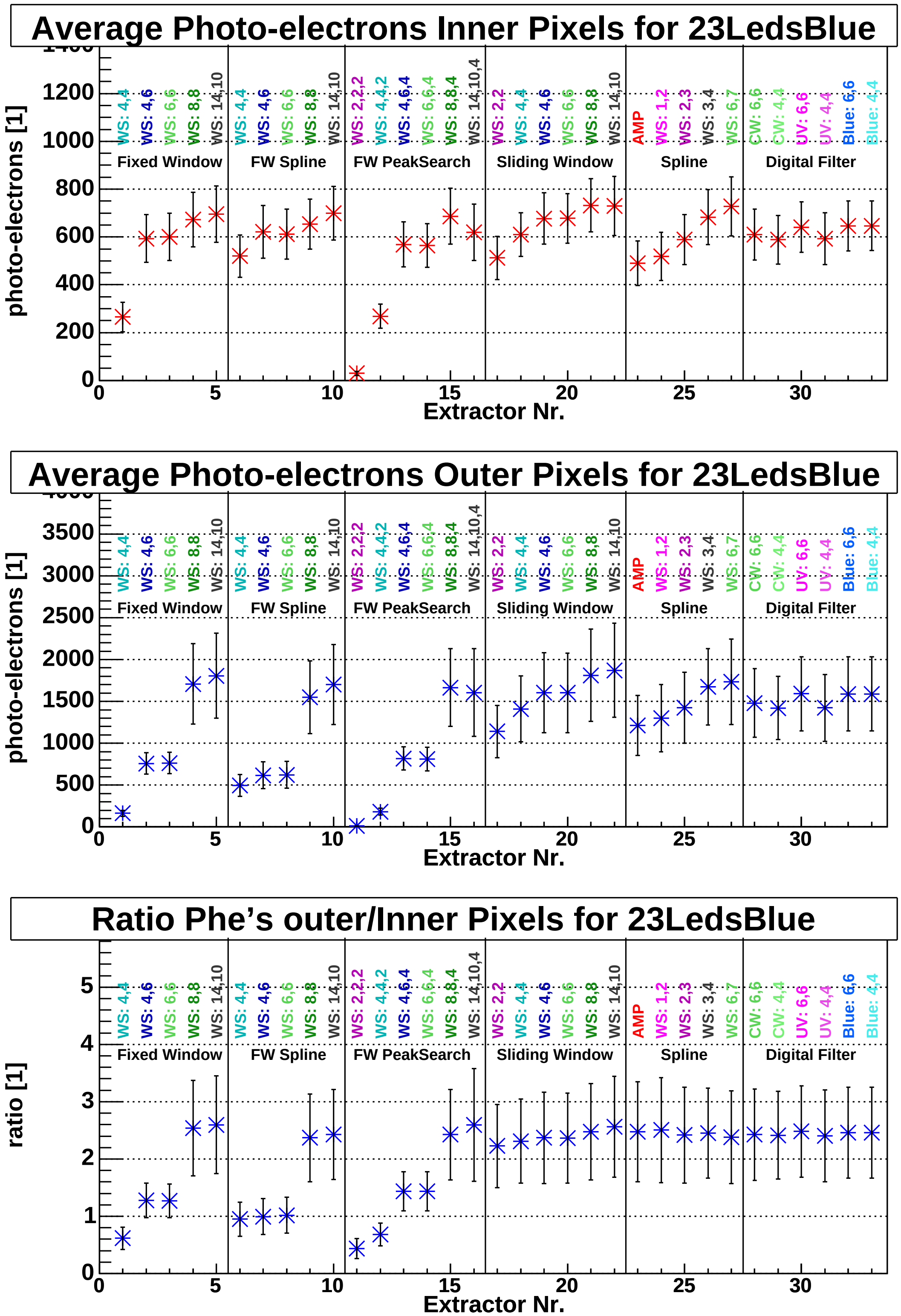

Figure 52: Number of photo-electrons from a typical, high-gain saturating calibration pulse of colour blue, reconstructed with each of the tested signal extractors. The first plots shows the number of photo-electrons obtained for the inner pixels, the second one for the outer pixels and the third shows the ratio of the mean number of photo-electrons for the outer pixels divided by the mean number of photo-electrons for the inner pixels. Points denote the mean of all not-excluded pixels, the error bars their RMS.

8.3 Linearity

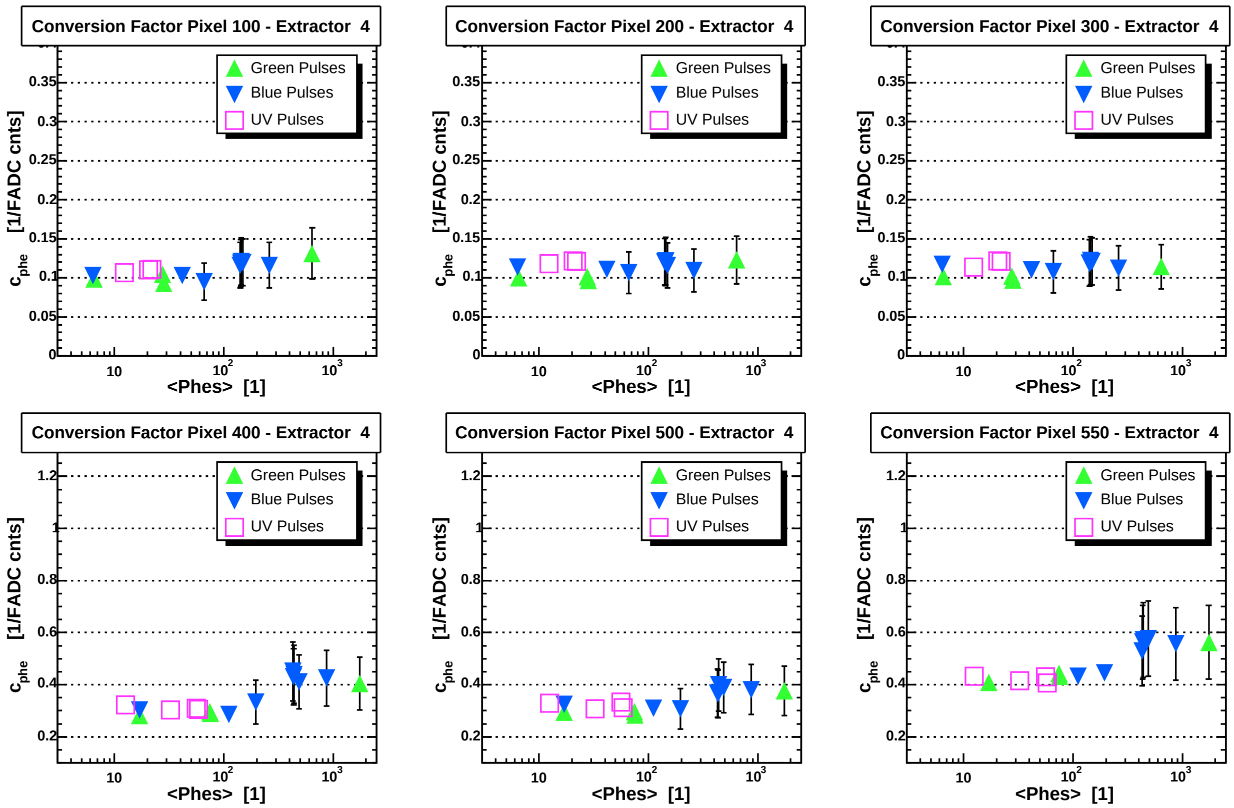

Figure 53: Conversion factor c_{phe} for three typical inner pixels (upper plots) and three typical outer ones (lower plots) obtained with the extractor MExtractFixedWindow on a window size of 8 high-gain and 8 low-gain slices (extractor #4).

In this section, we test the linearity of the conversion factors FADC counts to photo-electrons:

$$c_{phe} = < N_{phe} > / < \widehat{S} > \tag{45}$$

As the photo-multiplier and the subsequent optical transmission devices [18] is a relatively linear device over a wide dynamic range, the number of photo-electrons per charge has to remain constant over the tested linearity region.

A first test concerns the stability of the conversion factor: mean number of averaged photo-electrons per FADC counts over the tested intensity region. This test includes all systematic uncertainties in the calculation of the number of photo-electrons and the computation of the mean signal. A more detailed investigation of the linearity will be shown in a separate TDAS [6], although there, the number of photo-electrons will be calculated in a more independent way.

Figure 53 shows the conversion factor c_{phe} obtained for different light intensities and colors for three typical inner and three typical outer pixels using a fixed window on 8 FADC slices. The conversion factor seems to be linear to a good approximation, with the following restrictions:

- The green pulses yield systematically low conversion factors
- Some of the pixels show a difference between the high-gain ($<$100 phes for the inner, $<$300 phes for the outer pixels) and the low-gain ($>$100 phes for the inner, $>$300 phes for the outer pixels) region and a rather good stability of c_{phe} for each region separately.

We conclude that, with the above restrictions, the fixed window extractor #4 is a linear extractor for both high-gain and low-gain regions, separately.

Figures 54 and 55 show the conversion factors using an integrated spline and a fixed window with global peak search, respectively, over an extraction window of 8 FADC slices. The same behaviour is obtained as before. These extractors are linear to a good approximation, except for the two cases mentioned above.

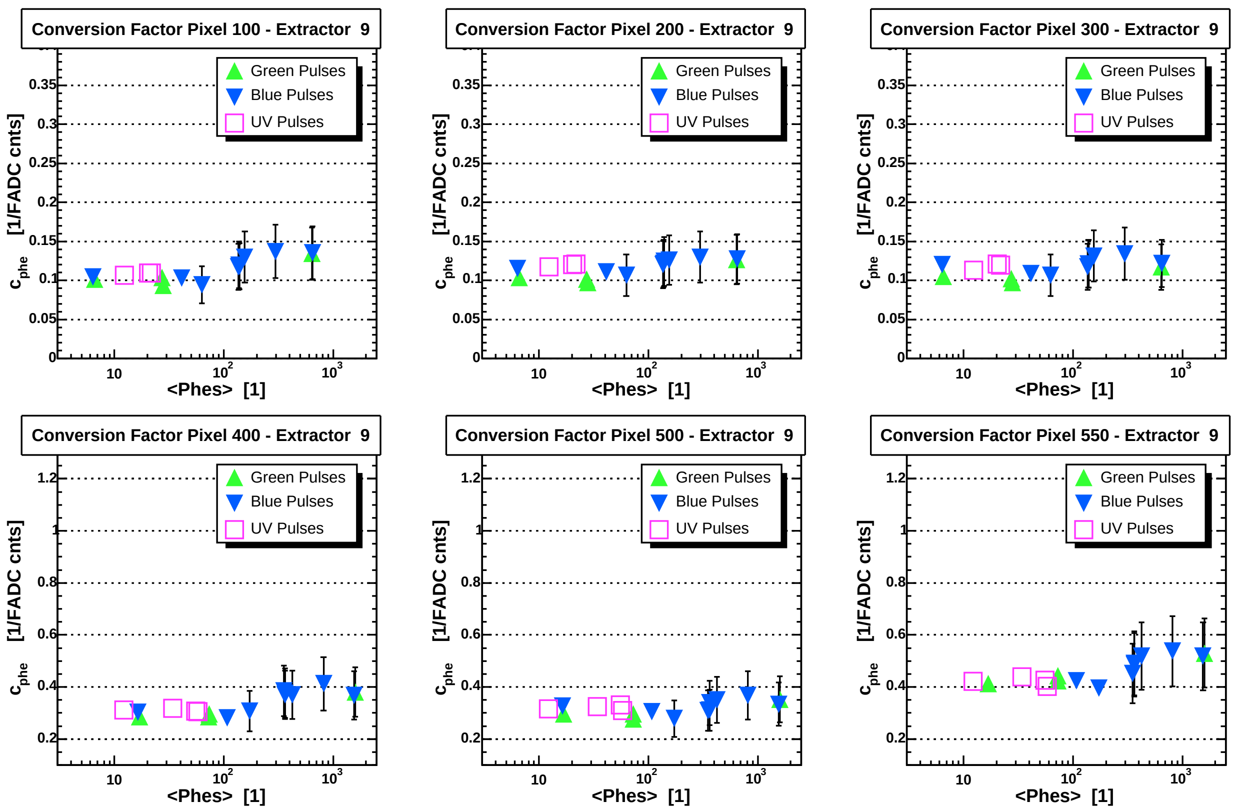

Figure 54: Conversion factor c_{phe} for three typical inner pixels (upper plots) and three typical outer ones (lower plots) obtained with the extractor MExtractFixedWindowSpline on a window size of 8 high-gain and 8 low-gain slices (extractor #9).

Figure 56 shows the conversion factors using a fixed window with global peak search integrating a window of 6 FADC slices. One can see that the linearity is completely lost above 300 photo-electrons in the outer pixels. Especially in the low-gain, the reconstructed mean charge is too low and the conversion factors bend down. We show this extractor especially because it has been used in the analysis and to derive a Crab spectrum with the consequence that the spectrum bends down at high energies. We suppose that the loss of linearity due to usage of

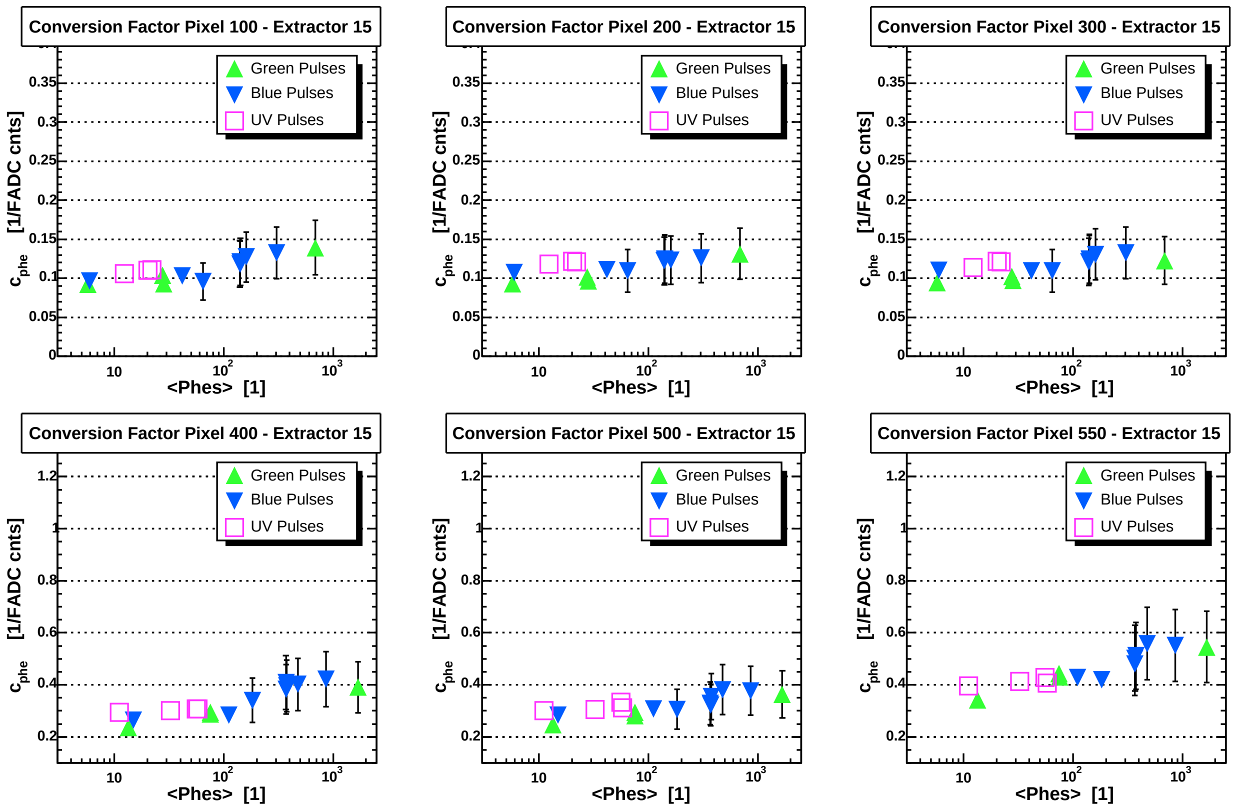

Figure 55: Conversion factor c_{phe} for three typical inner pixels (upper plots) and three typical outer ones (lower plots) obtained with the extractor MExtractFixedWindowPeakSearch on a window size of 8 high-gain and 8 low-gain slices (extractor #15).

this extractor is responsible for the encountered problems. A similar behaviour can be found for all extractors with window sizes smaller than 6 FADC slices, especially in the low-gain region. This is understandable since the low-gain pulse covers at least 6 FADC slices. (This behaviour was already visible in the investigations on the number of photo-electrons in the previous section 8.2).

Figure 57 shows the conversion factors using a sliding window of 6 FADC slices. The linearity is maintained like in the previous examples, except that for the smallest signals the effect of the bias is already visible.

Figure 58 shows the conversion factors using the amplitude-extracting spline (extractor #23). Here, the linearity is worse than in the previous examples. A very clear difference between high-gain and low-gain regions can be seen as well as a bigger general spread in conversion factors. In order to investigate if there is a common, systematic effect of the extractor, we show the averaged conversion factors over all inner and outer pixels in figure 59. Both characteristics are maintained there. Although the differences between high-gain and low-gain could be easily corrected for, we conclude that extractor #23 is still unstable against the linearity tests.

Figure 60 shows the conversion factors using a spline integrating over one effective FADC slice in the high-gain and 1.5 effective FADC slices in the low-gain region (extractor #24). The same

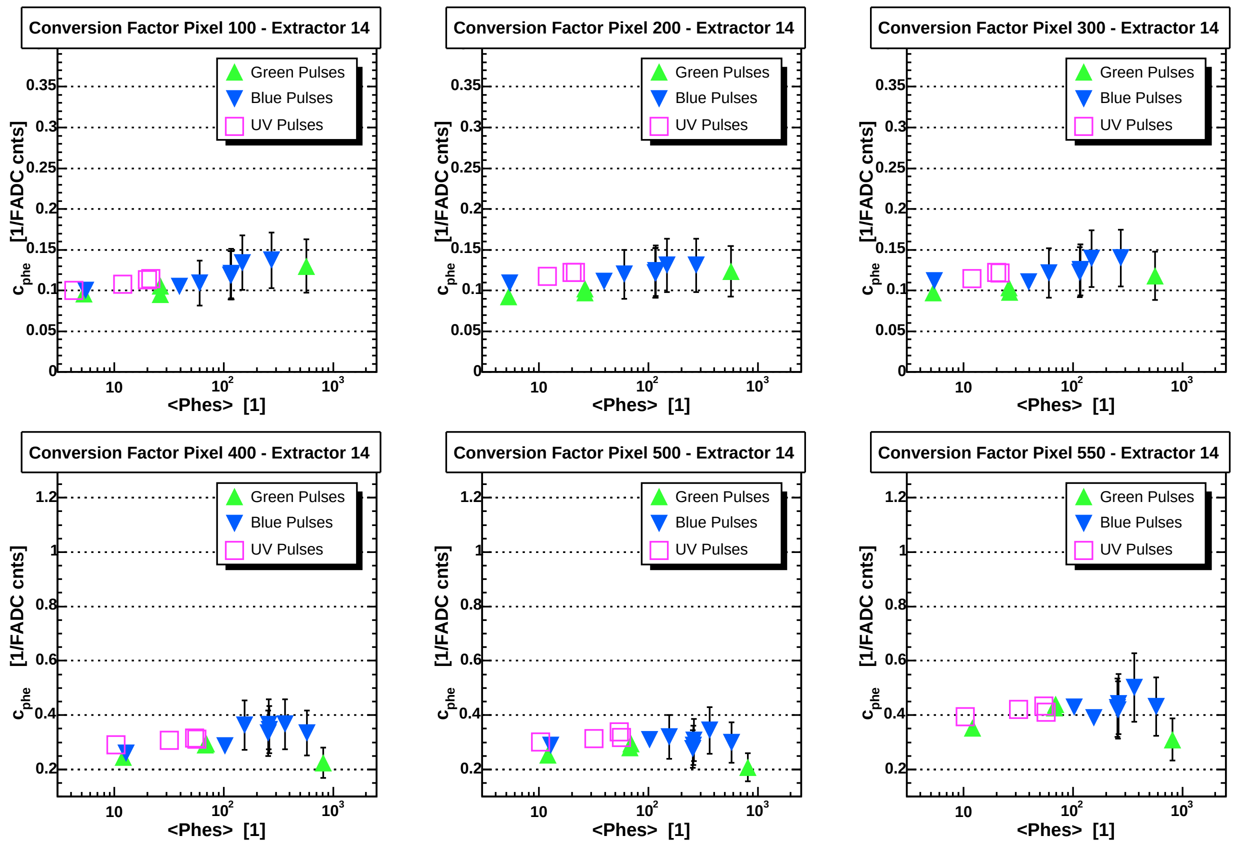

Figure 56: Example of a the development of the conversion factor FADC counts to photo-electrons for three typical inner pixels (upper plots) and three typical outer ones (lower plots) obtained with the extractor MExtractFixedWindowPeakSearch on a window size of 6 high-gain and 6 low-gain slices (extractor #11).

problems are found as with extractor #23, however to a much lower extent. The difference between high-gain and low-gain regions is less pronounced and the spread in conversion factors is smaller. Figure 61 shows already rather good stability except for the two lowest intensity pulses in green and blue. We conclude that extractor #24 is still un-stable, but preferable to the amplitude extractor.

Looking at figure 62, one can see that raising the integration window by two effective FADC slices in the high-gain and three effective FADC slices in the low-gain (extractor #25), the stability is completely resumed, except for a systematic increase of the conversion factor above 200 photo-electrons. We conclude that extractor #25 is almost as stable as the fixed window extractors.

Figure 64 and 66 show the conversion factors using a digital filter, applied on 6 FADC slices and respectively 4 FADC slices with weights calculated from the UV-calibration pulse in the high-gain region and from the blue calibration pulse in the low-gain region. One can see that one or two blue calibration pulses at low and intermediate intensity fall out of the linear region, moreover there is a small systematic offset between the high-gain and low-gain region. It seems that the digital filter does not pass this test if the pulse form changes for more than 2 ns

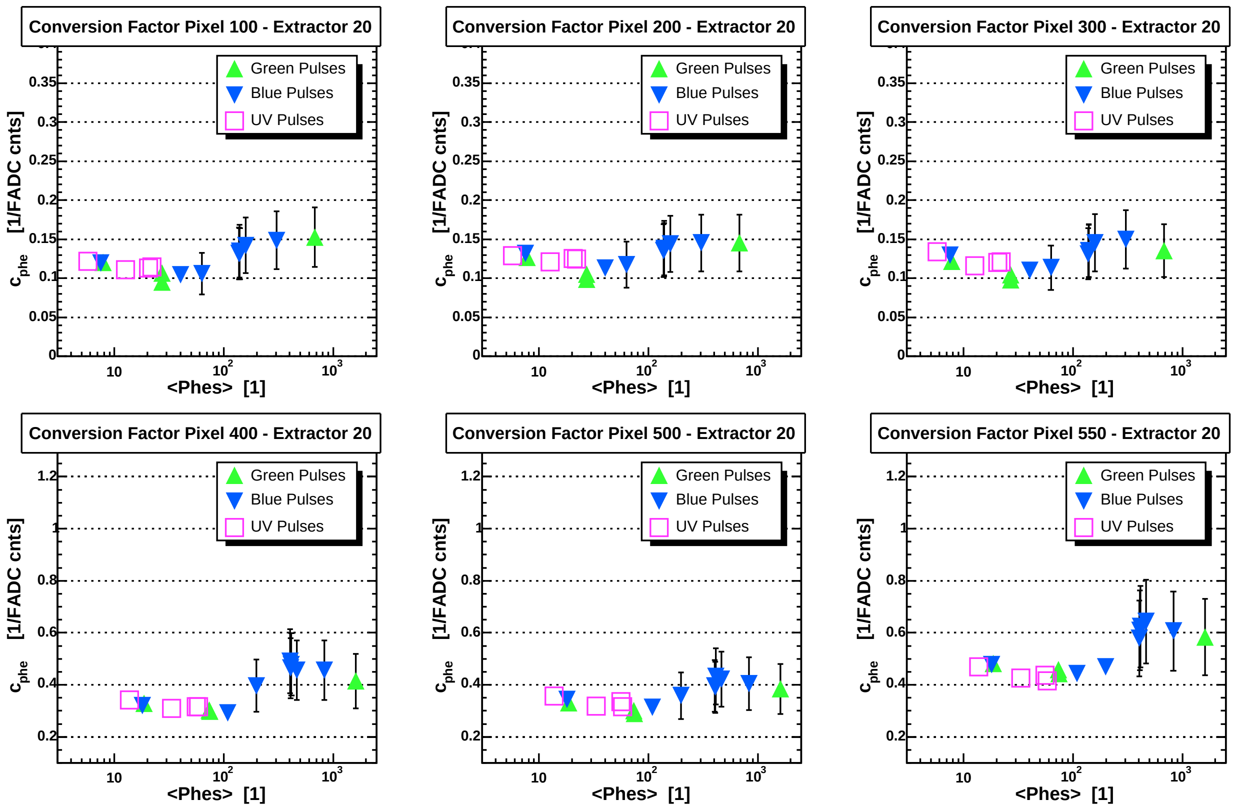

Figure 57: Example of a the development of the conversion factor FADC counts to photo-electrons for three typical inner pixels (upper plots) and three typical outer ones (lower plots) obtained with the extractor MExtractTimeAndChargeSlidingWindow on a window size of 6 high-gain and 6 low-gain slices (extractor #20).

from the expected one. The effect is not as problematic as it may appear here, because the actual calibration will not calculate the number of photo-electrons (with the F-Factor method) for every signal intensity. Thus, one possible reason for the instability is not relevant in the cosmics analysis. However, the limits of this extraction are visible here and should be monitored further.

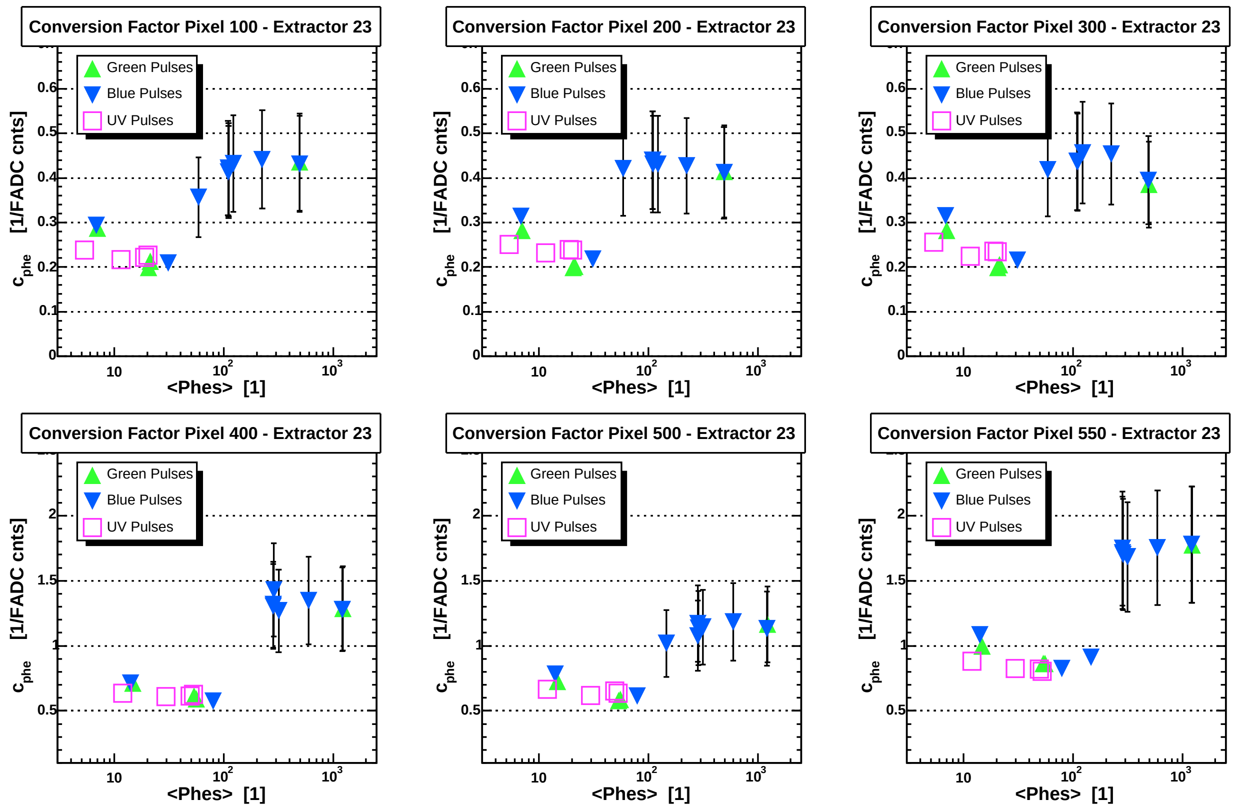

Figure 58: Conversion factor c_{phe} for three typical inner pixels (upper plots) and three typical outer ones (lower plots) obtained with the extractor MExtractTimeAndChargeSpline with amplitude extraction (extractor #23).

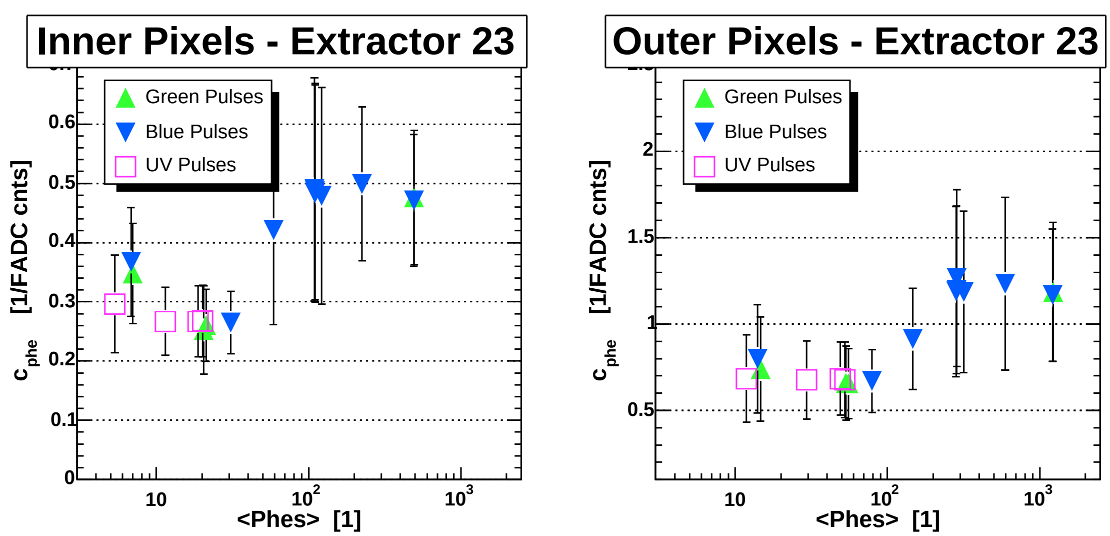

Figure 59: Conversion factor c_{phe} averaged over all inner (left) and all outer (right) pixels obtained with the extractor MExtractTimeAndChargeSpline with amplitude extraction (extractor #23).

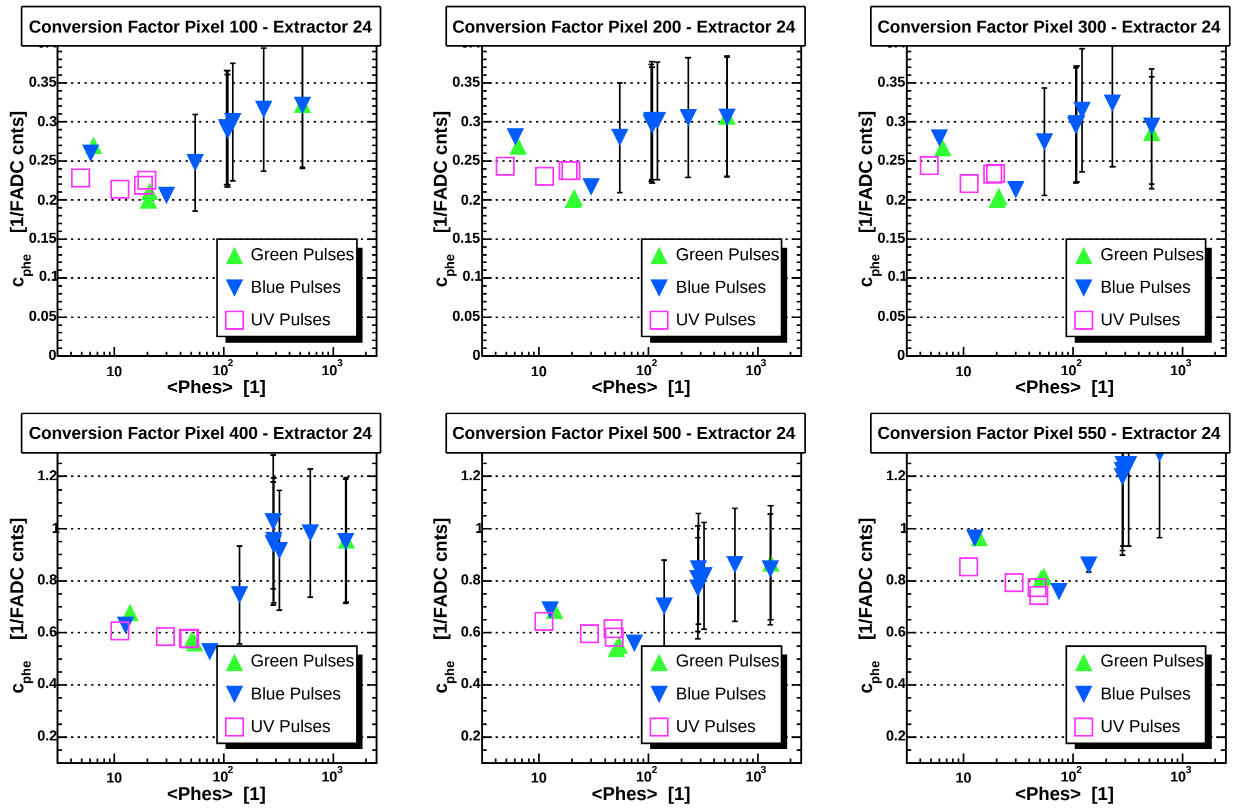

Figure 60: Conversion factor c_{phe} for three typical inner pixels (upper plots) and three typical outer ones (lower plots) obtained with the extractor MExtractTimeAndChargeSpline with window size of 1 high-gain and 2 low-gain slices (extractor #24).

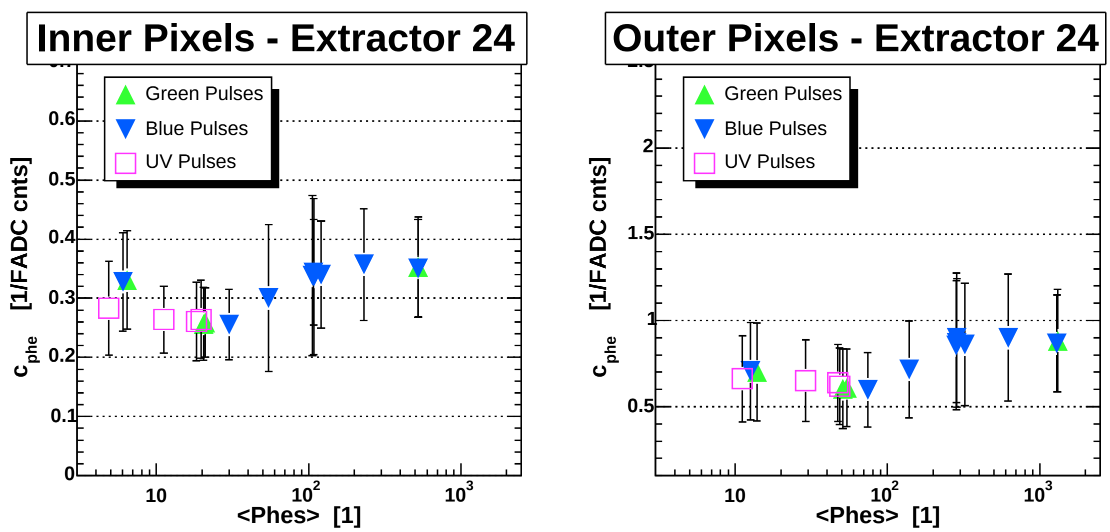

Figure 61: Conversion factor c_{phe} averaged over all inner (left) and all outer (right) pixels obtained with the extractor MExtractTimeAndChargeSpline with window size of 1 high-gain and 2 low-gain slices (extractor #24).

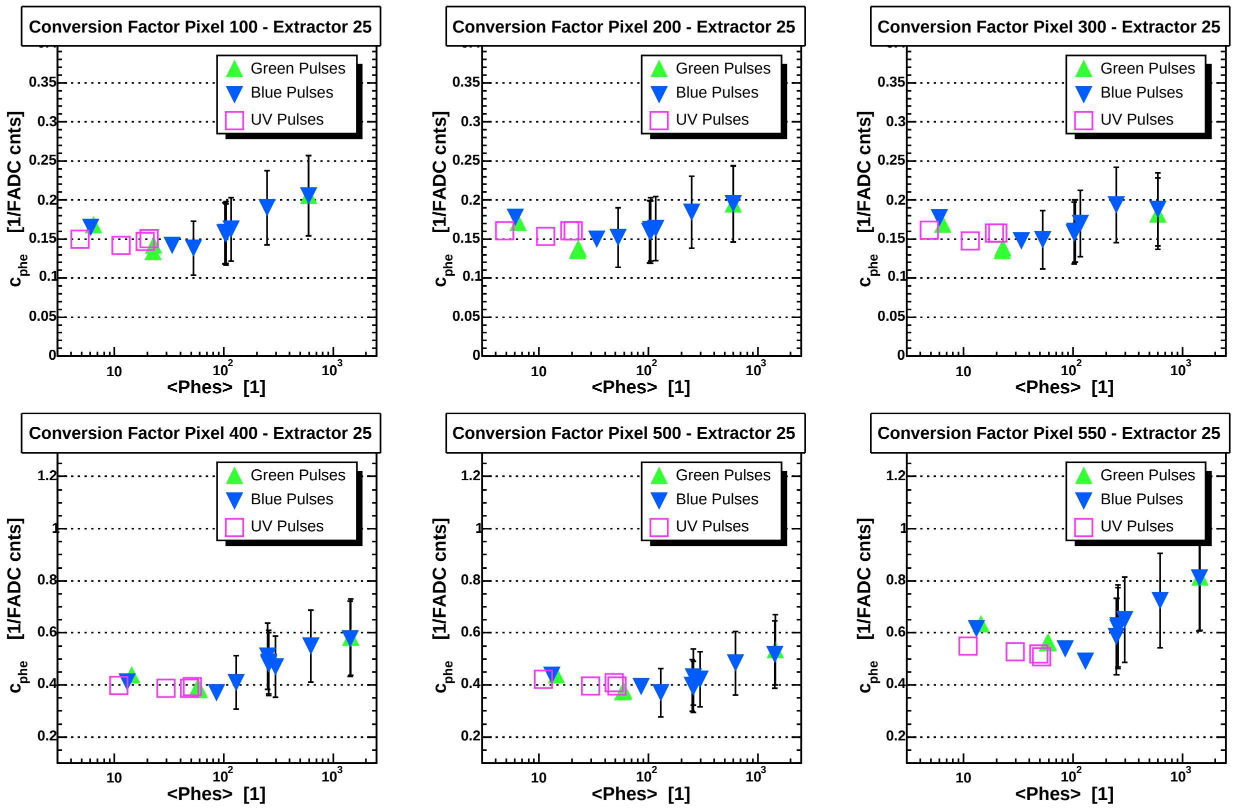

Figure 62: Conversion factor c_{phe} for three typical inner pixels (upper plots) and three typical outer ones (lower plots) obtained with the extractor MExtractTimeAndChargeSpline with window size of 2 high-gain and 3 low-gain slices (extractor #25).

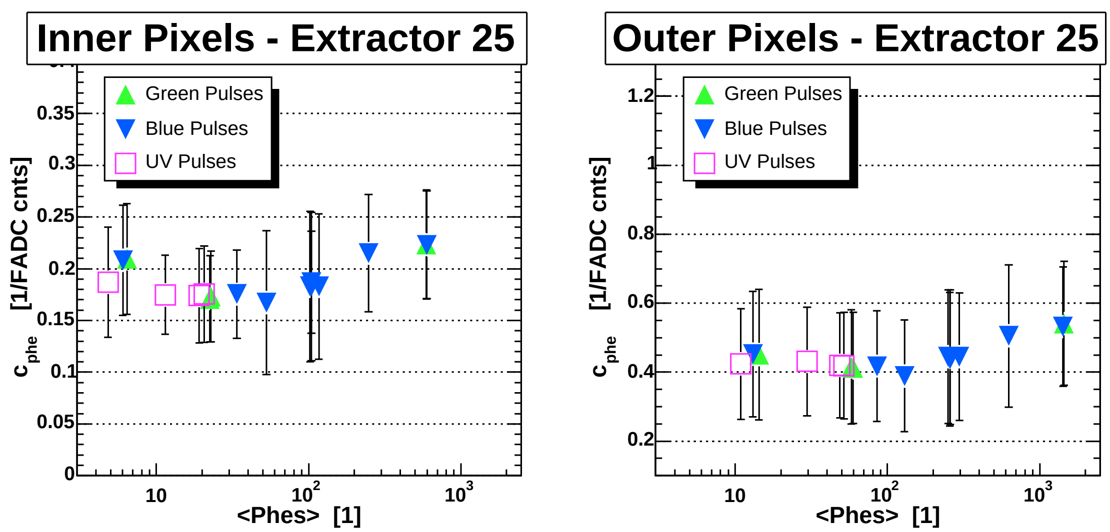

Figure 63: Conversion factor c_{phe} averaged over all inner (left) and all outer (right) pixels obtained with the extractor MExtractTimeAndChargeSpline with window size of 2 high-gain and 3 low-gain slices (extractor #25).

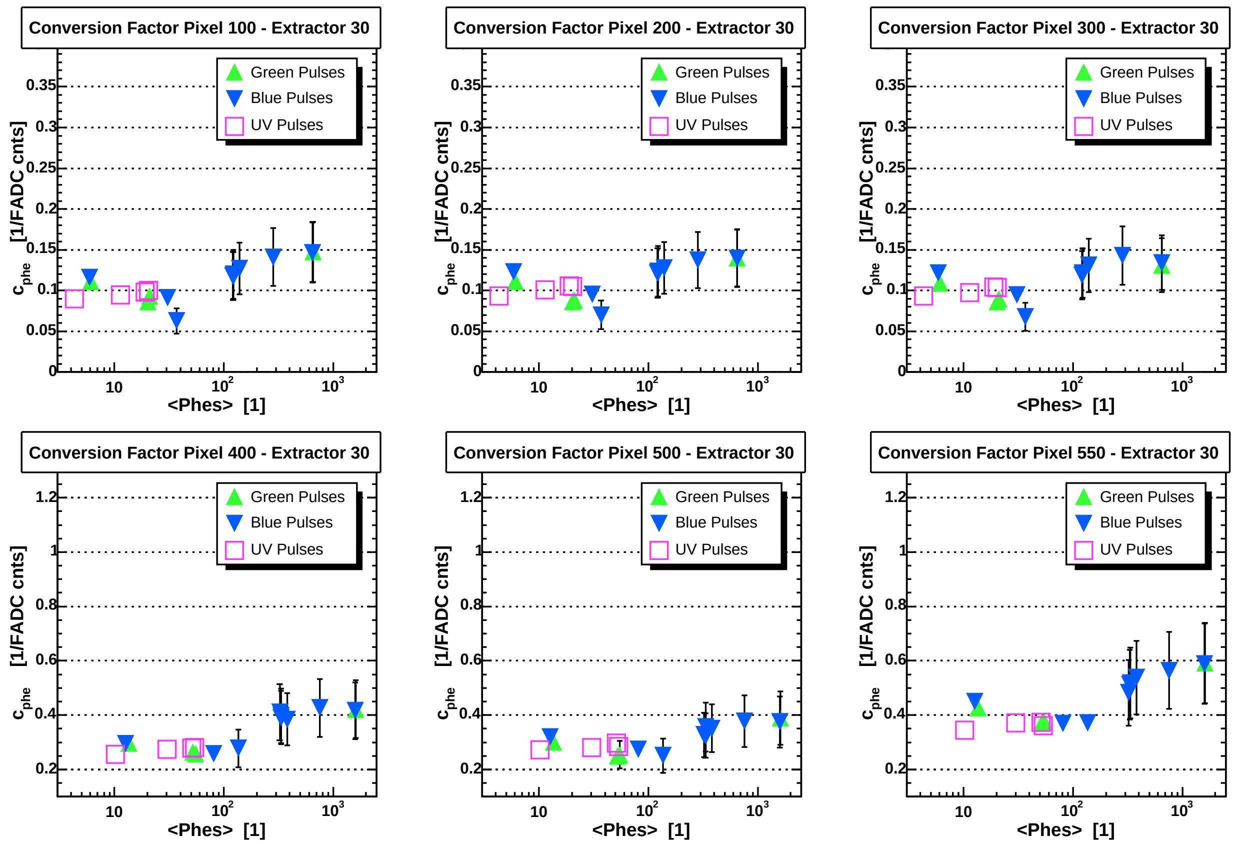

Figure 64: Conversion factor c_{phe} for three typical inner pixels (upper plots) and three typical outer ones (lower plots) obtained with the extractor MExtractTimeAndChargeDigitalFilter using a window size of 6 high-gain and 6 low-gain slices with UV-weights (extractor #30).

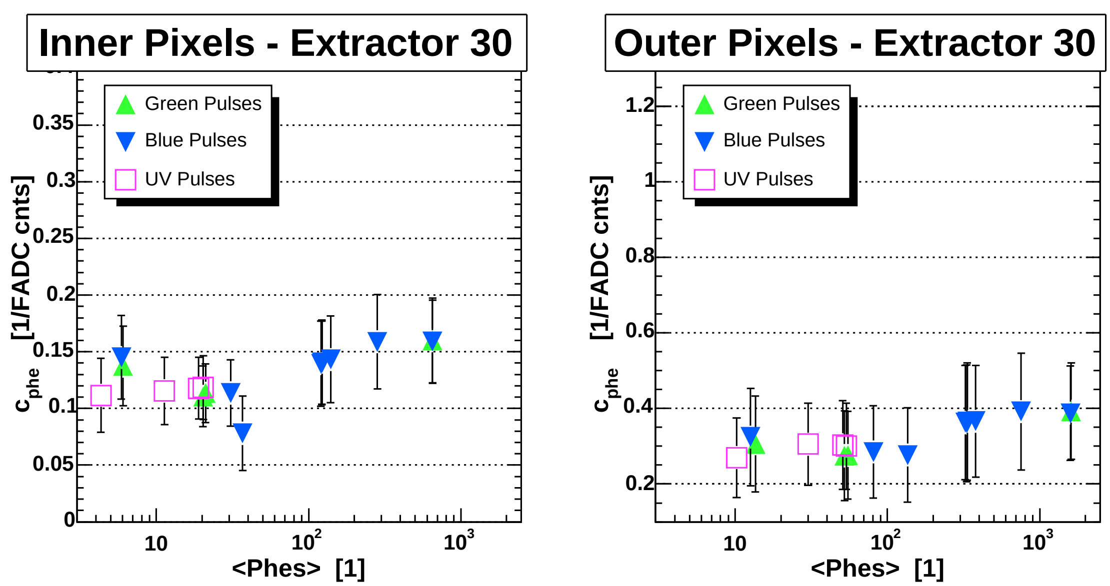

Figure 65: Conversion factor c_{phe} averaged over all inner (left) and all outer (right) pixels obtained with the extractor MExtractTimeAndChargeDigitalFilter with window size of 6 high-gain and 6 low-gain slices and UV-weight (extractor #30).

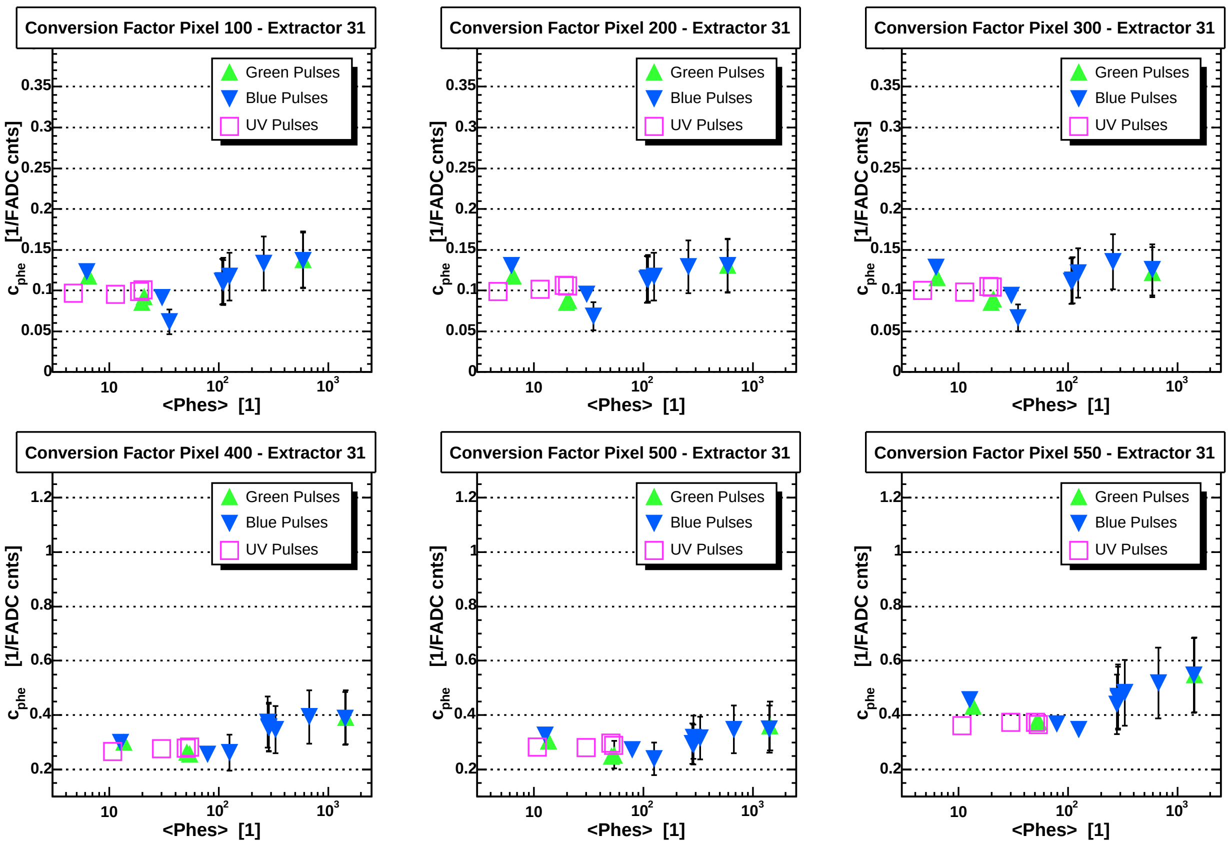

Figure 66: Conversion factor c_{phe} for three typical inner pixels (upper plots) and three typical outer ones (lower plots) obtained with the extractor MExtractTimeAndChargeDigitalFilter using a window size of 4 high-gain and 4 low-gain slices (extractor #31).

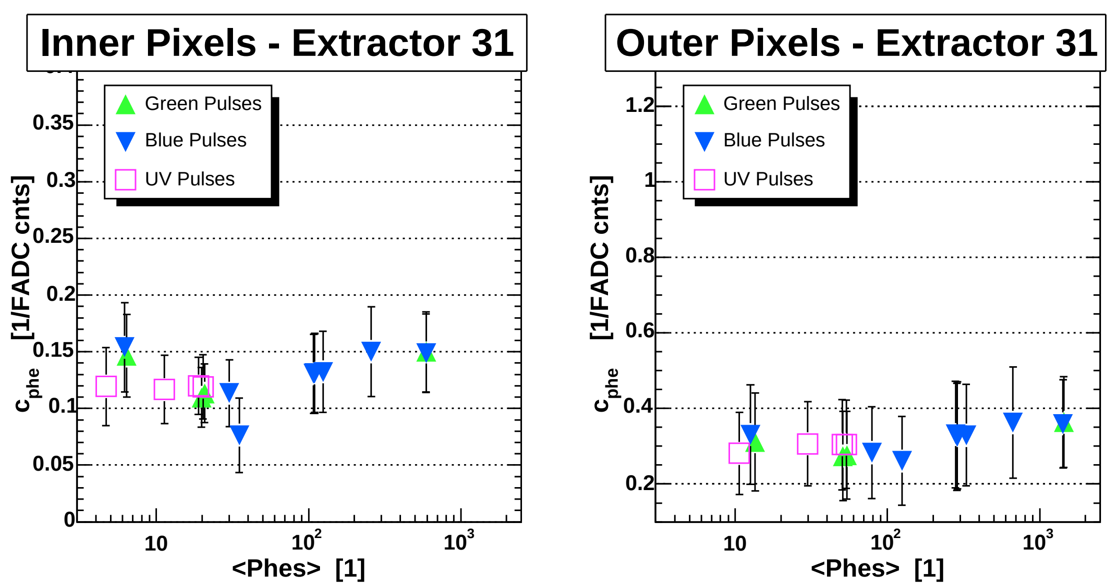

Figure 67: Conversion factor c_{phe} averaged over all inner (left) and all outer (right) pixels obtained with the extractor MExtractTimeAndChargeDigitalFilter with window size of 6 high-gain and 6 low-gain slices and blue weights (extractor #31).

8.4 Relative Arrival Time Calibration

The calibration LEDs deliver fast-rising pulses, uniform over the camera in signal size and time. We estimate the time-uniformity to as good as about 30 ps, a limit due to the different travel times of the light from the light source to the inner and outer parts of the camera. For cosmics data, however, the staggering of the mirrors limits the time uniformity to about 600 ps.

The extractors #17–33 are able to compute the arrival time of each pulse. Since the calibration does not permit a precise measurement of the absolute arrival time, we measure the relative arrival time for every channel with respect to a reference channel (usually pixel no. 1):

$$\delta t_i = t_i - t_1 \tag{46}$$

where t_i denotes the reconstructed arrival time of pixel number i and t_1 the reconstructed arrival time of the reference pixel no. 1 (software numbering). In one calibration run, one can then fill histograms of δt_i and fit them to the expected Gaussian distribution. The fits yield a mean $\mu(\delta t_i)$, comparable to systematic delays in the signal travel time, and a sigma $\sigma(\delta t_i)$, a measure of the combined time resolutions of pixel i and pixel 1. Assuming that the PMTs and readout channels are of the same kind, we obtain an approximate time resolution of pixel i:

$$t_i^{res} \approx \sigma(\delta t_i)/\sqrt{2} \tag{47}$$

Figures 68 show distributions of δt_i for a typical inner pixel and a non-saturating calibration pulse of UV-light, obtained with six different extractors. One can see that all of them yield acceptable Gaussian distributions, except for the sliding window extracting 2 slices which shows a three-peak structure and cannot be fitted. We discarded that particular extractor from the further studies of this section.

Figures 69 and 70 show the distributions of δt_i for a typical inner pixel and an intense, high-gain-saturating calibration pulse of blue light, obtained from the low-gain readout channel. One can see that the sliding window extractors yield double Gaussian structures, except for the largest window sizes of 8 and 10 FADC slices. Even then, the distributions are not exactly Gaussian. The maximum position extracting spline also yields distributions which are not exactly Gaussian and seems to miss the exact arrival time in some events. Only the position of the half-maximum gives the expected result of a single Gaussian distribution. A similar problem occurs in the case of the digital filter: If one takes the correct weights (fig. 70 bottom), the distribution is perfectly Gaussian and the resolution good, however a rather slight change from the blue calibration pulse weights to cosmics pulses weights (top) adds a secondary peak of events with mis-reconstructed arrival times. In principle, the χ^2 of the digital filter fit gives an information about whether the correct shape has been used.

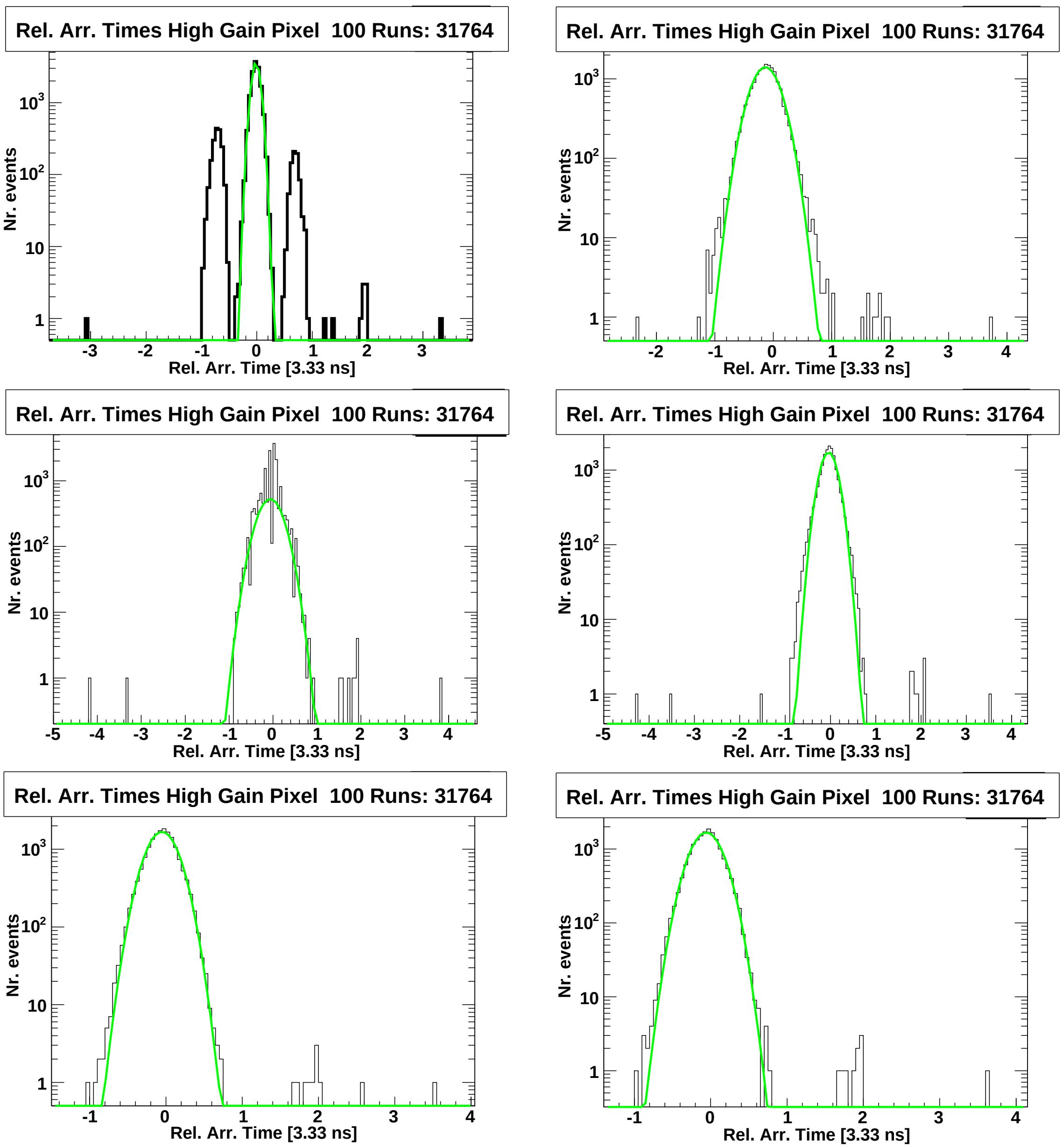

Figure 68: Examples of a distributions of relative arrival times δt_i of an inner pixel (no. 100)
Top: **MExtractTimeAndChargeSlidingWindow** *over 2 slices (#17) and 4 slices (#18)*
Center: **MExtractTimeAndChargeSpline** *with maximum (#23) and half-maximum pos. (#24)*
Bottom: **MExtractTimeAndChargeDigitalFilter** *fitted to a UV-calibration pulse over 6 slices (#30) and 4 slices (#31)*
A medium sized UV-pulse (5 Leds UV) has been used which does not saturate the high-gain readout channel.

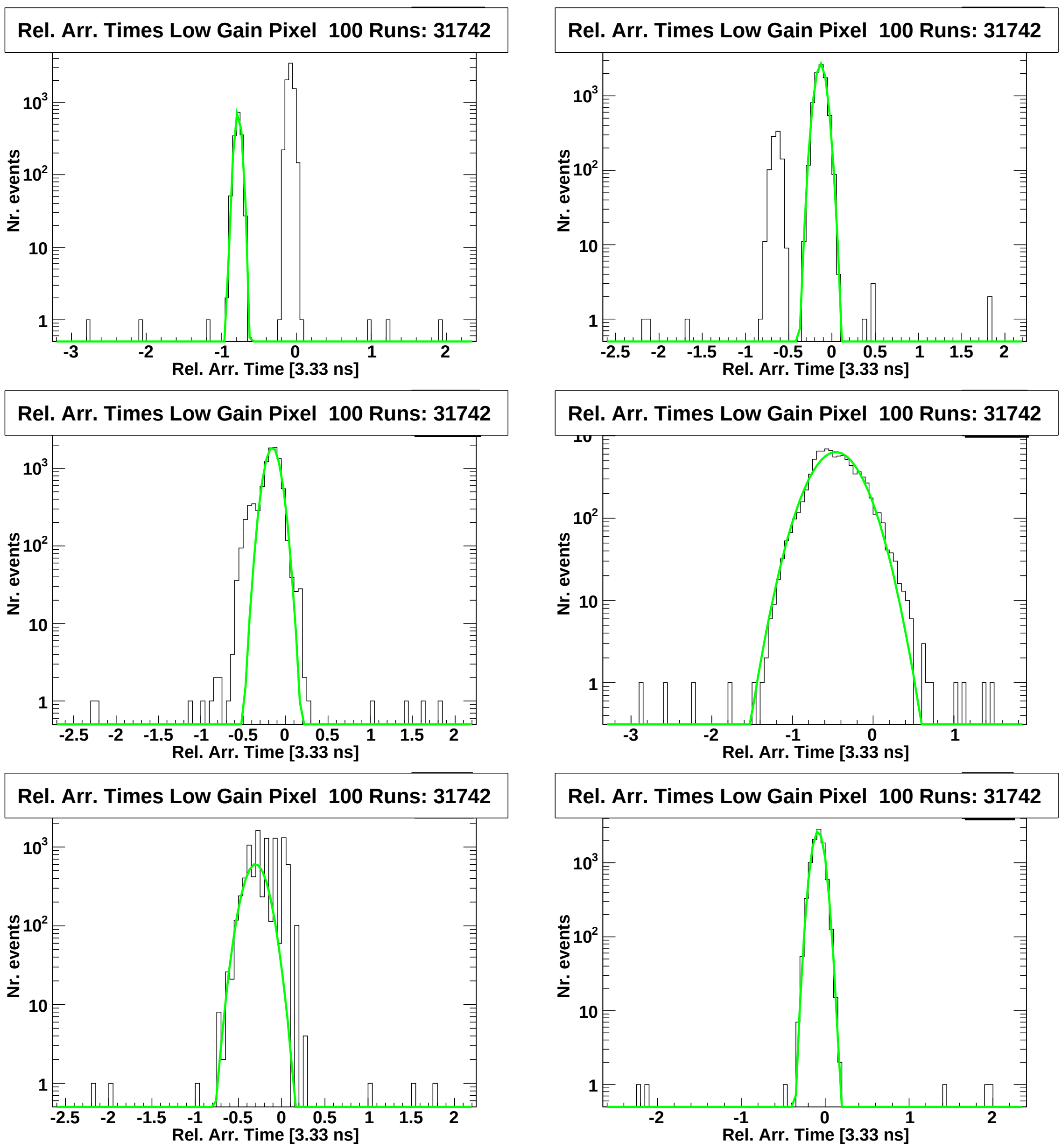

Figure 69: Examples of a distributions of relative arrival times δt_i of an inner pixel (no. 100)
Top: **MExtractTimeAndChargeSlidingWindow** *over 4 slices (#18) and 6 slices (#19)*
Center: **MExtractTimeAndChargeSlidingWindow** *over 8 slices (#20) and 10 slices (#21)*
Bottom: **MExtractTimeAndChargeSpline** *with maximum (#23) and half-maximum pos. (#24)*
A strong Blue pulse (23 Leds Blue) has been used which does not saturate the high-gain readout channel.

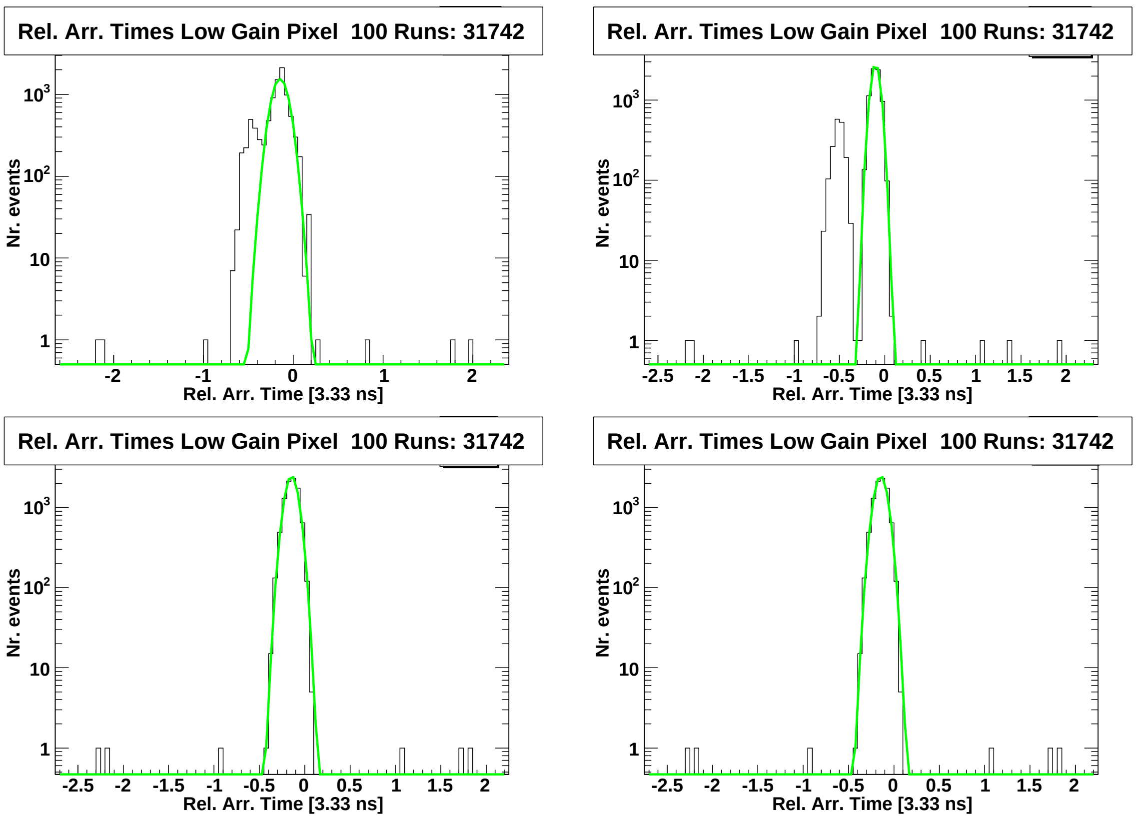

Figure 70: Examples of a distributions of relative arrival times δt_i of an inner pixel (no. 100)
Top: **MExtractTimeAndChargeDigitalFilter** *fitted to cosmics pulses over 6 slices (#30) and 4 slices (#31)*
Bottom: **MExtractTimeAndChargeDigitalFilter** *fitted to the correct blue calibration pulse over 6 slices (#30) and 4 slices (#31) A strong Blue pulse (23 Leds Blue) has been used which does not saturate the high-gain readout channel.*

8.5 Number of Outliers

As in section 8.1, we tested the number of outliers from the Gaussian distribution in order to count how many times the extractor has failed to reconstruct the correct arrival time.

Figure 71 shows the number of outliers for the different time extractors, obtained with a UV pulse of about 20 photo-electrons. One can see that all time extractors yield an acceptable mis-reconstruction rate of about 0.5%, except for the maximum searching spline yields three times more mis-reconstructions.

If one goes to very low-intensity pulses, as shown in figure 72, obtained with on average 4 photo-electrons, the number of mis-reconstructions increases considerably up to 20% for some extractors. We interpret this high mis-reconstruction rate to the increase possibility to mis-reconstruct a pulse from the night sky background noise instead of the signal pulse from the calibration LEDs. One can see that the digital filter using weights on 4 FADC slices is clear inferior to the one using 6 FADC slices in that respect.

The same conclusion seems to hold for the green pulse of about 20 photo-electrons (figure 73) where the digital filter over 6 FADC slices seems to yield more stable results than the one over 4 FADC slices. The half-maximum searching spline seems to be superior to the maximum-searching one.

In figure 74, one can see the number of outliers from an intense calibration pulse of blue light yielding about 600 photo-electrons per inner pixel. All extractors seem to be stable, except for the digital filter with weights over 4 FADC slices. This is expected, since the low-gain pulse is wider than 4 FADC slices.

In all previous plots, the sliding window yielded the most stable results, however later we will see that this stability is only due to an increased time spread.

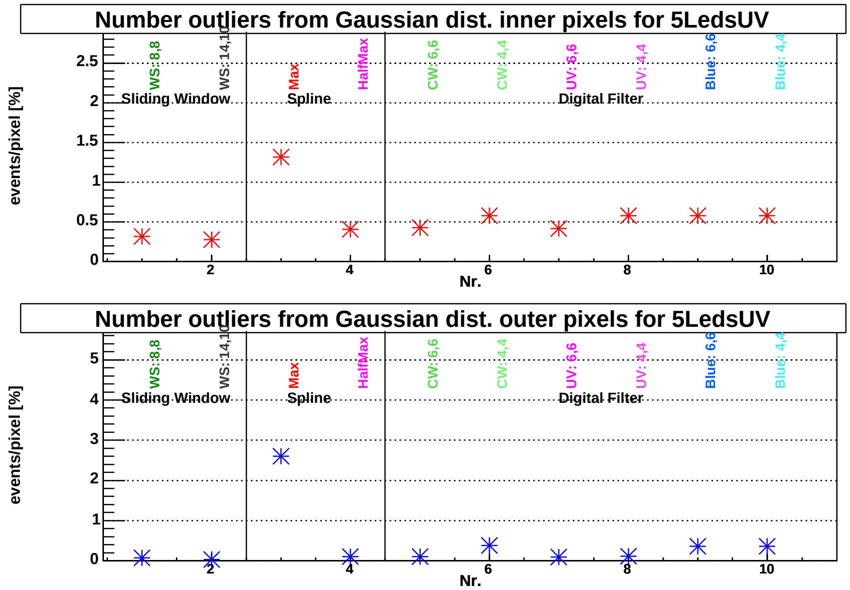

Figure 71: Reconstructed arrival time resolutions from a typical, not saturating calibration pulse of colour UV, reconstructed with each of the tested arrival time extractors. The first plots shows the time resolutions obtained for the inner pixels, the second one for the outer pixels. Points denote the mean of all not-excluded pixels, the error bars their RMS.

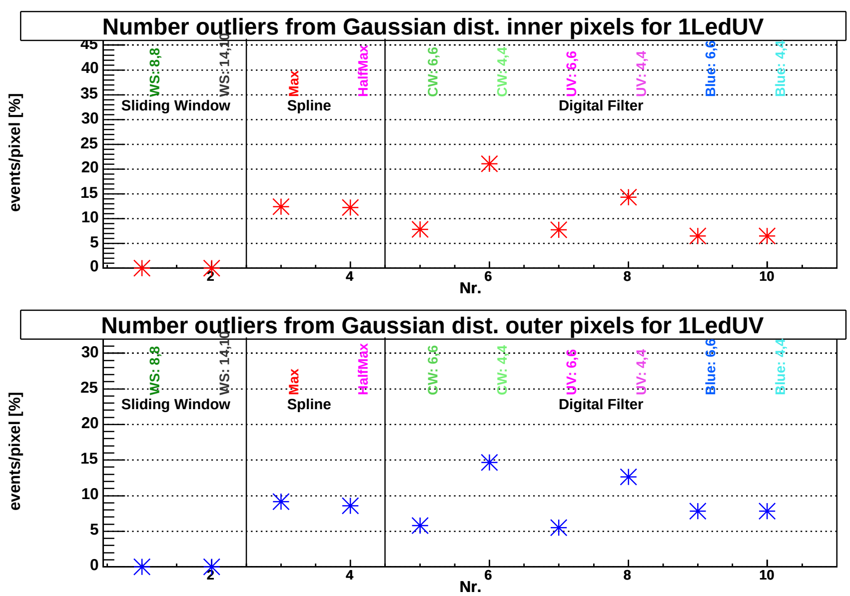

Figure 72: Reconstructed arrival time resolutions from the lowest intensity calibration pulse of colour UV (carrying a mean number of 4 photo-electrons), reconstructed with each of the tested arrival time extractors. The first plots shows the time resolutions obtained for the inner pixels, the second one for the outer pixels. Points denote the mean of all not-excluded pixels, the error bars their RMS.

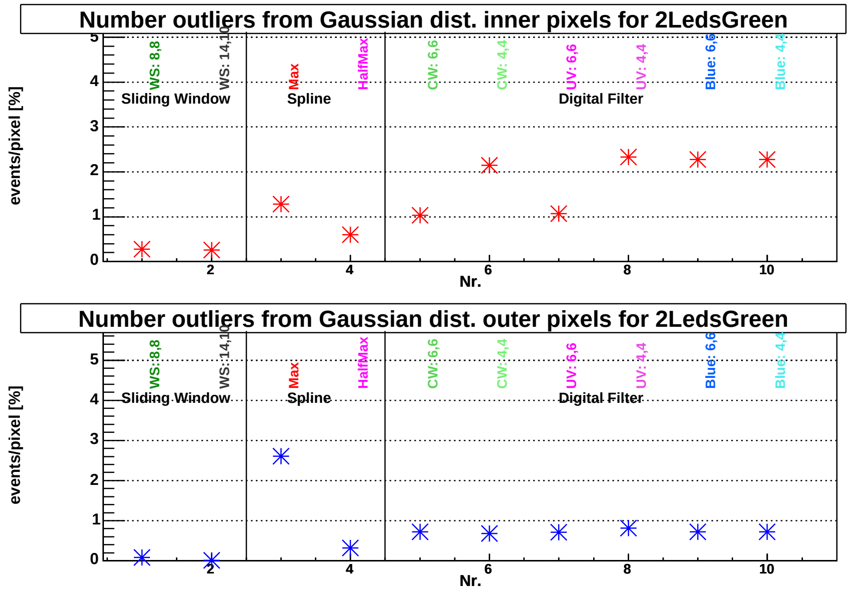

Figure 73: Reconstructed arrival time resolutions from a typical, not saturating calibration pulse of colour Green, reconstructed with each of the tested arrival time extractors. The first plots shows the time resolutions obtained for the inner pixels, the second one for the outer pixels. Points denote the mean of all not-excluded pixels, the error bars their RMS.

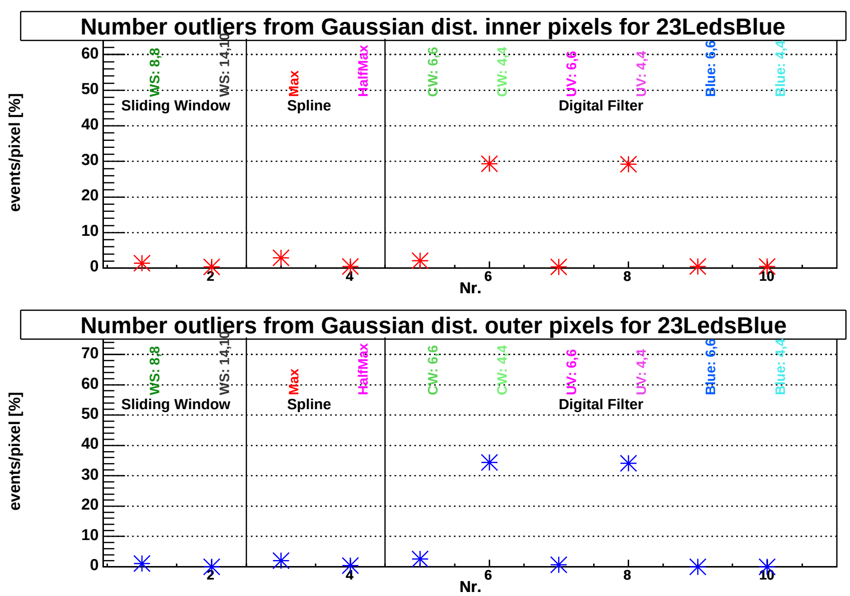

Figure 74: Reconstructed arrival time resolutions from the highest intensity calibration pulse of colour blue, reconstructed with each of the tested arrival time extractors. The first plots shows the time resolutions obtained for the inner pixels, the second one for the outer pixels. Points denote the mean of all not-excluded pixels, the error bars their RMS.

8.6 Time Resolution

There are three intrinsic contributions to the timing accuracy of the signal:

1. The intrinsic arrival time spread of the photons on the PMT: This time spread can be estimated roughly by the intrinsic width δt_{IN} of the input light pulse. The resulting time resolution is given by:

$$\Delta t \approx \frac{\delta t_{\mathrm{IN}}}{\sqrt{Q/\mathrm{phe}}} \tag{48}$$

   The width δt_{LED} of the calibration pulses of about 2 ns for the faster UV pulses and 3–4 ns for the green and blue pulses, for muons it is a few hundred ps, for gammas about 1 ns and for hadrons a few ns.

2. The intrinsic transit time spread TTS of the photo-multiplier: It can be of the order of a few hundreds of ps per single photo electron, depending on the wavelength of the incident light. As in the case of the photon arrival time spread, the total time spread scales with the inverse of the square root of the number of photo-electrons:

$$\Delta t \approx \frac{\delta t_{\mathrm{TTS}}}{\sqrt{Q/\mathrm{phe}}} \tag{49}$$

3. The reconstruction error due to the background noise and limited extractor resolution: This contribution is inversely proportional to the signal to square root of background light intensities.

$$\Delta t \approx \frac{\delta t_{\mathrm{rec}} \cdot R/\mathrm{phe}}{Q/\mathrm{phe}} \tag{50}$$

   where R is the resolution defined in equation 23.

4. A constant offset due to the residual FADC clock jitter [19]

$$\Delta t \approx \delta t_0 \tag{51}$$

In the following, we show measurements of the time resolutions at different signal intensities in real conditions for the calibration pulses. These set upper limits to the time resolution for cosmics since their intrinsic arrival time spread is smaller.

Figures 75 through 78 show the measured time resolutions for very different calibration pulse intensities and colors. One can see that the sliding window resolutions are always worse than the spline and digital filter algorithms. Moreover, the half-maximum position search by the spline is always slightly better than the maximum position search. The digital filter does not show notable differences with respect to the pulse form or the extraction window size, except for the low-gain extraction where the 4 slices seem to yield a better resolution. This is only after excluding about 30% of the events, as shown in figure 74.

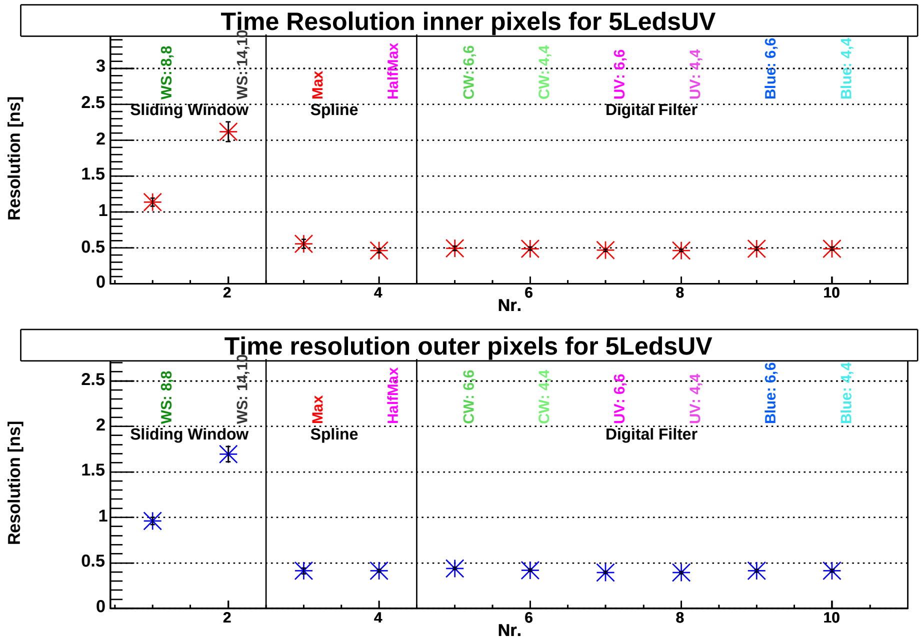

Figure 75: Reconstructed arrival time resolutions from a typical, not saturating calibration pulse of colour UV, reconstructed with each of the tested arrival time extractors. The first plots shows the time resolutions obtained for the inner pixels, the second one for the outer pixels. Points denote the mean of all not-excluded pixels, the error bars their RMS.

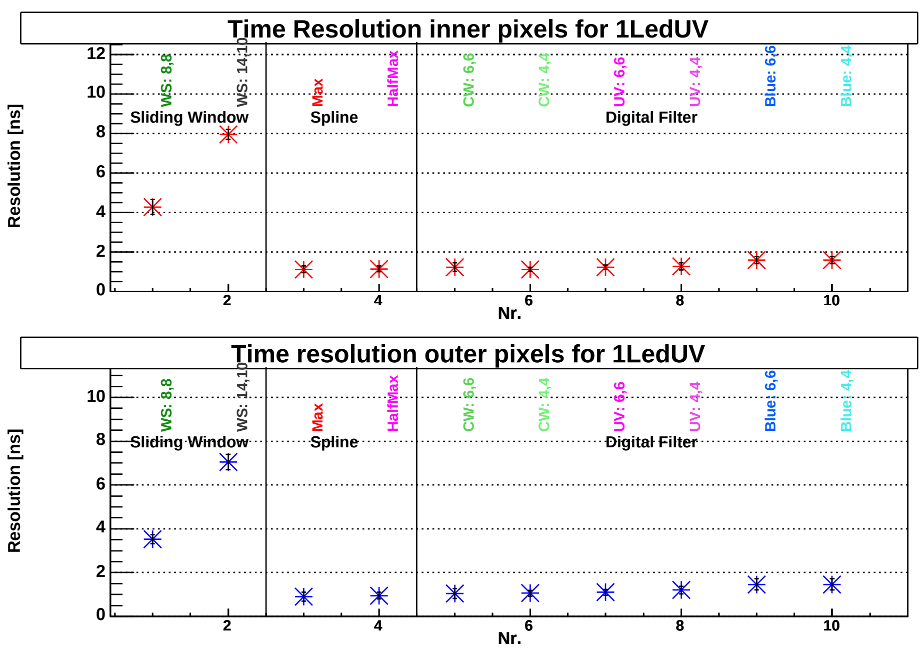

Figure 76: Reconstructed arrival time resolutions from the lowest intensity calibration pulse of colour UV (carrying a mean number of 4 photo-electrons), reconstructed with each of the tested arrival time extractors. The first plots shows the time resolutions obtained for the inner pixels, the second one for the outer pixels. Points denote the mean of all not-excluded pixels, the error bars their RMS.

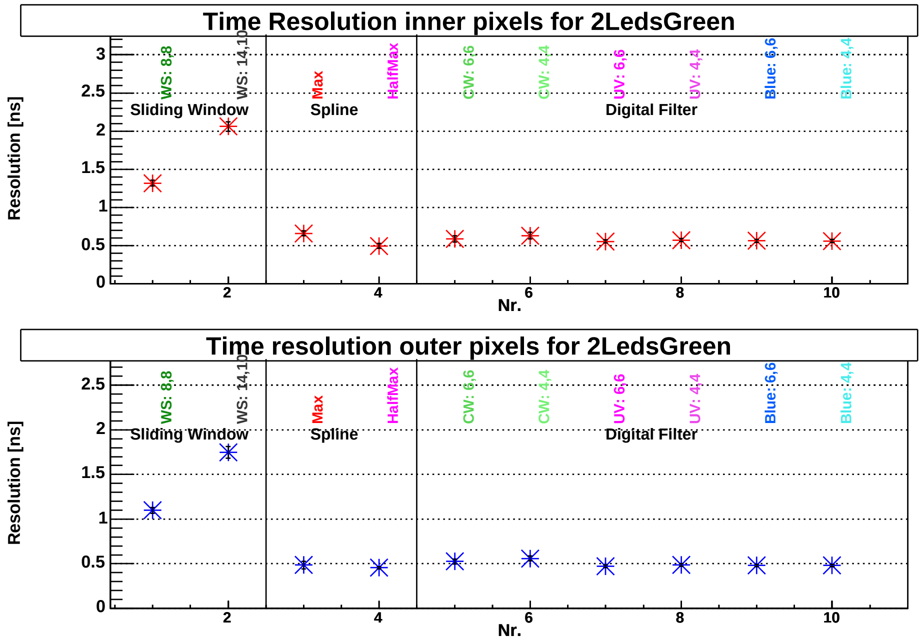

Figure 77: Reconstructed arrival time resolutions from a typical, not saturating calibration pulse of colour Green, reconstructed with each of the tested arrival time extractors. The first plots shows the time resolutions obtained for the inner pixels, the second one for the outer pixels. Points denote the mean of all not-excluded pixels, the error bars their RMS.

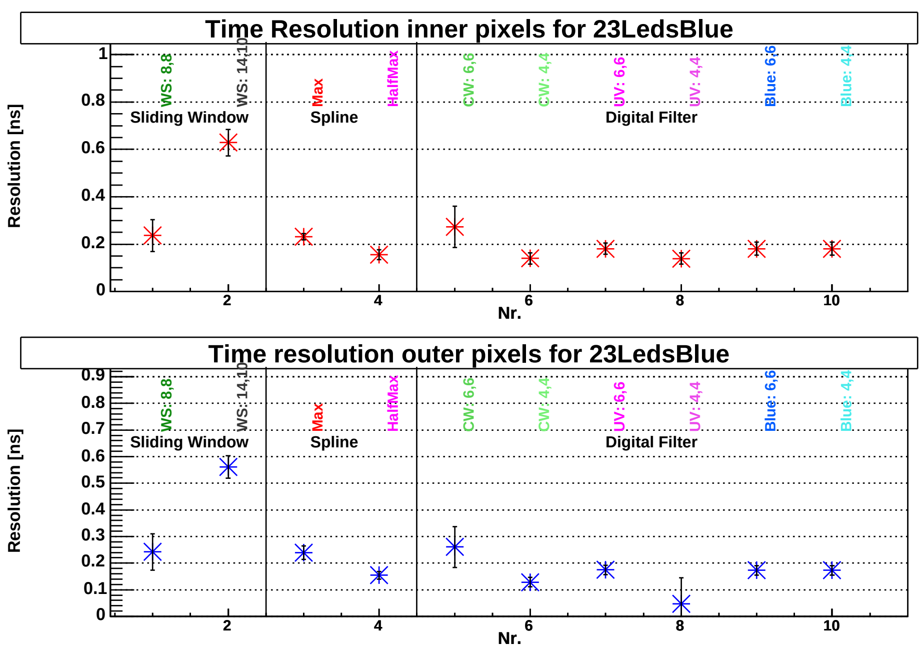

Figure 78: Reconstructed arrival time resolutions from the highest intensity calibration pulse of colour blue, reconstructed with each of the tested arrival time extractors. The first plots shows the time resolutions obtained for the inner pixels, the second one for the outer pixels. Points denote the mean of all not-excluded pixels, the error bars their RMS.

The following figure 79 shows the time resolution for various calibration runs taken with different colors and light intensities as a function of the mean number of photo-electrons – reconstructed with the F-Factor method – for four different time extractors. The dependencies have been fit to the following empirical relation:

$$\Delta T = \sqrt{\frac{A^2}{<Q>/\mathrm{phe}} + \frac{B^2}{<Q>^2/\mathrm{phe}^2} + C^2}. \tag{52}$$

The fit results are summarized in table 8.

Time Fit Results									
		Inner Pixels				Outer Pixels			
Nr.	Name	A	B	C	χ^2/NDF	A	B	C	χ^2/NDF
21	Sliding Window (8,8)	3.5±0.4	29±1	0.24±0.05	10.2	6.0±0.7	52±4	0.23±0.04	4.3
25	Spline Half Max.	1.9±0.2	3.8±1.0	0.15±0.02	1.6	2.6±0.2	8.3±1.9	0.15±0.01	2.3
32	Digital Filter (6 sl.)	1.7±0.2	5.7±0.8	0.21±0.02	5.0	2.3±0.3	13 ±2	0.20±0.01	4.0
33	Digital Filter (4 sl.)	1.7±0.1	4.6±0.7	0.21±0.02	6.2	2.3±0.2	11 ±2	0.20±0.01	5.3

Table 8: The fit results obtained from the fit of equation 52 to the time resolutions obtained for various intensities and colors. The fit probabilities are very small mainly because of the different intrinsic arrival time spreads of the photon pulses from different colors.

.

The low fit probabilities are partly due to the systematic differences in the pulse forms in intrinsic arrival time spreads between pulses of different LED colors. Nevertheless, we had to include all colors in the fit to cover the full dynamic range. In general, one can see that the time resolutions for the UV pulses are systematically better than for the other colors which we attribute to the fact the these pulses have a smaller intrinsic pulse width – which is very close to pulses from cosmics. Moreover, there are clear differences visible between different time extractors, especially the sliding window extractor yields poor resolutions. The other three extractors are compatible within the errors, with the half-maximum of the spline being slightly better.

To summarize, we find that we can obtain a time resolution of better than 1 ns for all pulses above a threshold of 5 photo-electrons. This corresponds roughly to the image cleaning threshold in case of using the best signal extractor. At the largest signals, we can reach a time resolution of as good as 200 ps.

The expected time resolution for inner pixels and cosmics pulses can thus be conservatively estimated to be:

$$\Delta T_{\mathrm{cosmics}} \approx \sqrt{\frac{4\,\mathrm{ns}^2}{<Q>/\mathrm{phe}} + \frac{20\,\mathrm{ns}^2}{<Q>^2/\mathrm{phe}^2} + 0.04\,\mathrm{ns}^2}. \tag{53}$$

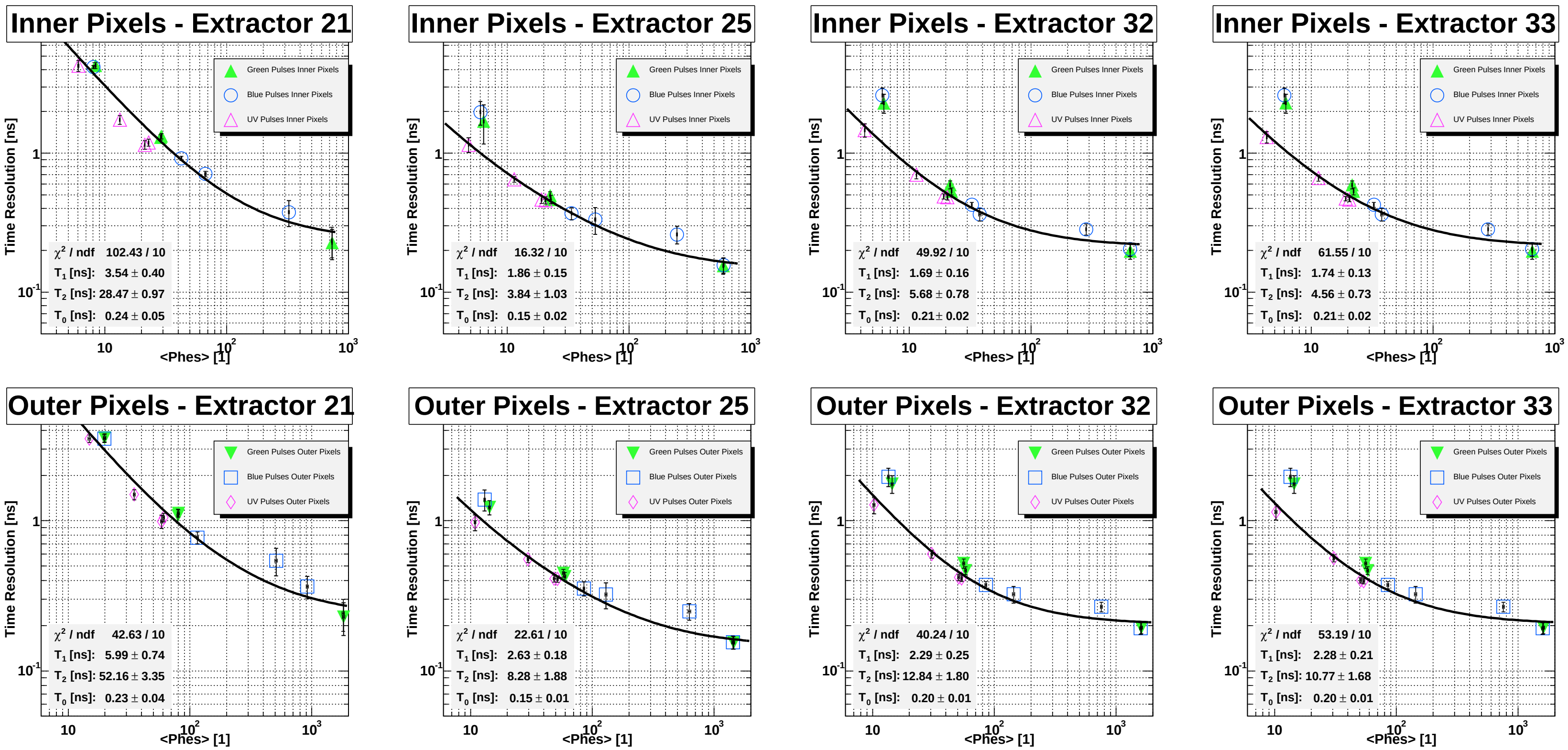

Figure 79: Reconstructed mean arrival time resolutions as a function of the extracted mean number of photo-electrons for the weighted sliding window with a window size of 8 slices (extractor #21, top left), the half-maximum searching spline (extractor #25, top right), the digital filter with correct pulse weights over 6 slices (extractor #30 and #32, bottom left) and the digital filter with UV calibration-pulse weights over 4 slices (extractor #31 and #33, bottom right). Error bars denote the spread (RMS) of time resolutions of the investigated channels. The marker colors show the applied pulser colour, except for the last (green) point where all three colors were used.

The above resolution seems to be already limited by the intrinsic resolution of the photomultipliers and the staggering of the mirrors in case of the MAGIC-I telescope.

8.6.1 Comparison with Results From the Monte Carlo Simulation

Comparing the found time resolution (eq. 53) with the results obtained from the Monte Carlo simulation (figures 28 and 29), one can see that the time resolutions are about 50–100% better in the simulation than in real conditions, except for the digital filter with 4 FADC slices which is much worse in the Monte Carlo simulation.

The first finding is understandable since the simulated light pulses had a much smaller intrinsic time spread of 1 ns whereas the calibration light pulses are a factor 2–3 broader. Also the intrinsic PMT transit time spread has not been simulated as well as the FADC clock noise jitter and other possible sources of time resolution degradation. Dividing the coefficient for A and B in equation 53 with the corresponding ratios yields more or less the correct time resolutions in the simulation, except for the missing offset.

We conclude therefore that the results on time resolution are consistent with the findings of this chapter and that equation 53 has to be considered rather an upper limit to the actual time resolution of cosmics pulses. The only time extractor with contradictory results (the digital filter with 4 FADC slices) has to be examined further, especially in the Monte Carlo simulation.

9 CPU Requirements

We tested the speed of the extractors by running them on an Intel Pentium IV, 2.4 GHz CPU machine at IFAE and measured the number of executed events per seconds. This was done using the CPU-time measure features which incorporates each task in MARS.

The results could easily differ by about 20% from one try to another (using the same extractor), but in general, the differences between the extractors are much bigger than the intrinsic fluctuation. Table 9 shows the obtained results. The numbers in this list have to be compared to the I/O speed of about 400 evts/sec. of the **MRead**-task which performs the reading (and de-compression) of the merpped root-files in MARS. Thus, for time being, every extractor being faster than this reference number does not limit the total event reconstruction speed. Only the integrating spline extractors lie below this limit and would need to be optimized further.

Measured Extraction Speed			
Nr.	Name	Events/sec. (CPU)	comments
1	Fixed Win. (4,4)	3500–4500	no time
2	Fixed Win. (4,6)	3500–4500	no time
3	Fixed Win. (6.6)	3200–4000	no time
4	Fixed Win. (8,8)	3200–4000	no time
5	Fixed W. (14,10)	2700–3300	no time
6	Fix. Win. Spline (4,4)	1700–2200	no time
7	Fix. Win. Spline (4,6)	1700–2200	no time
8	Fix. Win. Spline (6.6)	1700–2100	no time
9	Fix. Win. Spline (8,8)	1300–1800	no time
10	Fix. Win. Spl. (14,10)	600–1200	no time
11	Fix. Win. Peak S. (2,2)	2300–2900	no time
12	Fix. Win. Peak S. (4,4)	2300–2900	no time
13	Fix. Win. Peak S. (4.6)	2300–2900	no time
14	Fix. Win. Peak S. (6,6)	2300–2900	no time
15	Fix. Win. Peak S. (8,8)	2200–2800	no time
16	Fix. Win. Pk S. (14,10)	2000–2500	no time
17	Slid. Win. (2,2)	400–700	
18	Slid. Win. (4,4)	500–800	
19	Slid. Win. (4.6)	500–800	
20	Slid. Win. (6,6)	1000–1300	
21	Slid. Win. (8,8)	1100–1400	
22	Slid. W. (14,10)	1000–1800	
23	Spline Amplitude	700–1000	
24	Spline Int. (1,1.5)	300–500	
25	Spline Int. (2,3)	200–400	
26	Spline Int. (4,6)	150–200	to be optimized
27	Spline Int. (6,9)	80–120	to be optimized
28	Dig. Filt. (6,6)	700–900	
29	Dig. Filt. (4,4)	700–900	
34	Dig. Filt. Pk S.	500–600	

Table 9: The extraction speed measured for every extractor.

10 Results

Based on the previous investigations, we summarize the obtained results in table 10. The following criteria have been used to compare the extractors:

- Stability of the reconstructed charge in the calibration. Extractors with more than 5% of the pixels excluded from the calibration with any colour or intensity are considered as too unstable. Also extractors yielding more than 0.1% mis-reconstructed events are excluded. Moreover, the correct number of photo-electrons should be reconstructed at least for the standard calibration pulses (10 LEDs UV).
- The extractor should yield stable results against slight modifications of the pulse shape.
- The extractor must also yield the correct charges for the low-gain pulses on average.
- The reconstructed charge must be linear to the input signal charge for all signals above the image cleaning level and below the low-gain saturation level.
- The resolution of the reconstructed charge should not depend significantly on the signal amplitude, especially should never become comparable to the intrinsic Poissonian signal fluctuations.
- The resolution of the reconstructed charge should not exceed twice the resolution of the best extractor.
- The extractor should not have a charge bias bigger than its charge resolution.
- The time resolution should not be worse than twice the one obtainable with the best extractor.
- The number of mis-reconstructed times should not exceed 1% on average (including the FADC jumps).
- The needed CPU-time should not exceed the one required for reading the data into memory and writing it to disk.

Table 10 shows which extractors fulfill the above criteria. One can see that there are a handful extractors which are excluded by only one criterion:

- The sliding window extracting 8 slices in high- and low-gain which is only excluded by the poor resolution at very low intensities.
- The integrating spline over 2 FADC slices which still needs to be optimized somewhat for speed.

The digital filter passes all tests, where the extraction over 4 FADC slices yields still superior resolutions compared to the one over 6 FADC slices.

Nr.	Name	Stab. $\widehat{S}$ calib.	Stab. pulse shape	Stab. low-gain	Lin. $\widehat{S}$ size	Res. $\widehat{S}$ const.	Res. $\widehat{S}$	Bias $\widehat{S}$	Res. $\widehat{T}$	Stab. $\widehat{T}$	Speed
	Tested Characteristics										
1	Fix Win. (4,4)	**NO**	**NO**	**NO**	**NO**	**NO**	**NO**	–	n/a	n/a	**BEST**
2	Fix Win. (4,6)	**NO**	**NO**	**NO**	**NO**	**NO**	**NO**	–	n/a	n/a	**BEST**
3	Fix Win. (6.6)	OK	OK	**NO**	OK	OK	OK	–	n/a	n/a	OK
4	Fix Win. (8,8)	**NO**	OK	OK	**BEST**	**NO**	OK	–	n/a	n/a	OK
5	Fix W. (14,10)	**NO**	OK	OK	**BEST**	**NO**	OK	–	n/a	n/a	OK
6	FW. Spl. (4,4)	OK	**NO**	**NO**	**NO**	OK	**NO**	–	n/a	n/a	OK
7	FW. Spl. (4,6)	OK	**NO**	**NO**	**NO**	OK	**NO**	–	n/a	n/a	OK
8	FW. Spl. (6.6)	**NO**	OK	**NO**	**NO**	OK	OK	–	n/a	n/a	OK
9	FW. Spl. (8,8)	**NO**	OK	OK	OK	**NO**	OK	–	n/a	n/a	OK
10	FW. Spl (14,10)	**NO**	OK	OK	OK	**NO**	OK	–	n/a	n/a	OK
11	FW. Pk S. (2,2)	**NO**	**NO**	**NO**	**NO**	**NO**	**NO**	–	n/a	n/a	OK
12	FW. Pk S. (4,4)	OK	**NO**	**NO**	**NO**	**NO**	**NO**	–	n/a	n/a	OK
13	FW. Pk S. (4.6)	OK	**NO**	**NO**	**NO**	**NO**	**NO**	–	n/a	n/a	OK
14	FW. Pk S. (6,6)	OK	OK	**NO**	**NO**	OK	OK	–	n/a	n/a	OK
15	FW. Pk S. (8,8)	**NO**	OK	OK	OK	**NO**	OK	–	n/a	n/a	OK
16	FW Pk S (14,10)	**NO**	OK	OK	OK	**NO**	OK	–	n/a	n/a	OK
17	Slid. W. (2,2)	OK	**NO**	**NO**	**NO**	OK	**NO**	OK	**NO**	**NO**	OK
18	Slid. W. (4,4)	OK	OK	OK	**NO**	OK	OK	OK	**NO**	**NO**	OK
19	Slid. W. (4.6)	OK	OK	OK	OK	OK	OK	OK	OK	**NO**	OK
20	Slid. W. (6,6)	OK	OK	OK	OK	**NO**	OK	OK	**NO**	OK	**BEST**
21	Slid. W. (8,8)	OK	OK	OK	OK	**NO**	OK	OK	OK	OK	**BEST**
22	Slid. W. (14,10)	**NO**	OK	OK	OK	**NO**	**NO**	OK	**NO**	OK	**BEST**
23	Spline Ampl.	**NO**	NOT TESTED	OK	**NO**	**NO**	**NO**	**NO**	OK	**NO**	OK
24	Splne Int. (1,1.5)	OK	NOT TESTED	OK	**NO**	**NO**	**NO**	OK	**BEST**	OK	OK
25	Spline Int. (2,3)	**BEST**	NOT TESTED	OK	OK	OK	OK	OK	**BEST**	OK	**NO**
26	Spline Int. (4,6)	OK	OK	OK	OK	OK	OK	OK	**BEST**	OK	**NO**
27	Spline Int. (6,9)	OK	OK	OK	OK	**NO**	OK	**BEST**	**BEST**	OK	**NO**
28	Dig. Filt. (6,6)	OK	OK	OK	OK	OK	OK	OK	OK	OK	OK
29	Dig. Filt. (4,4)	OK	OK	OK	OK	OK	**BEST**	OK	**BEST**	OK	OK

Table 10: The tested characteristics for every extractor: Bias, Resolution ("Res."), stability ("Stab."), linearity ("Lin.") for both charge signal $\widehat{S}$ and time $\widehat{T}$, and speed. OK means that the extractor has passed the test, without being among the best. **NO** *means that the extractor has severely failed the test and should not be taken because of that reason.* **BEST** *means that the extractor(s) have come out as best of the particular test.*

11 Conclusions

In the past, many MAGIC analyses have been conducted using different signal extractors. We developed and tested the most important signal and time extraction algorithms in the standard MAGIC software framework MARS. Our findings are that using a right signal extractor is important since some of the investigated ones differ considerably in quality and can severely degrade the subsequent analyses. On the other hand, we have found that advanced signal reconstruction algorithms open a new window to lower analysis energy threshold and permit to use the time information of shower analyses.

In order to give a guideline for future usage of the tested signal extractors, we consider the following requirements to be of most importance:

- The calibration (including the F-Factor method) has to run stably and yield reliable results for all pixels.
- The extracted signal should be as linear as possible over the whole dynamic range, including especially the low-gain range.
- The combined resolution and bias should result in a lowest possible image cleaning threshold.
- The extracted time should yield the best possible resolution.

Following these requirements, we recommend to exclude in the future the following signal extraction algorithms:

- All fixed window extractors using a window size of up to 6 FADC slices, including the fixed window peak search algorithm.
- All sliding window extractors using a window size of up to 4 FADC slices.
- The amplitude extracting spline.

For a conservative and stable analysis, we recommend to use (except for the December 2004 and January 2005 data):

- The sliding window, using an extraction window size of 6–8 FADC slices for the high-gain and 8 FADC slices for the low-gain channel.

For the most demanding analyses, especially at low energies and using the timing information, we recommend:

- The spline algorithm, integrating from 0.5 FADC slices before the pulse maximum to 1.5 FADC slices after the pulse maximum and computing the position of the half-maximum at the rising edge of the pulse.

- The digital filter fitting the pulse over 4 or 6 FADC slices in the high-gain region and 6 FADC slices in the low-gain region.

Unfortunately, part of our recent data, taken in December 2004 and January 2005 had a severe problem with the pulse location within the recorded FADC slices. In the recorded samples, the low-gain pulse is situated so far to the right that a part of it reaches out of the recorded window. This poses severe problems to all extractors which integrate the entire low-gain pulse. We have seen that the spline extractor and the digital filter over 4 FADC slices are still capable to reconstruct the low-gain pulse properly for this partly corrupt data sample, although the linearity of the reconstructed signal might still be affected above signals of about 300 photo-electrons per pixel.

Special caution has to be made if the F-Factor method is applied for calibration with signal extractors which have an intensity-dependent resolution. This applies especially to the spline algorithms and the digital filter over a window size of 4 FADC slices.

References

[1] C. Baixeras et al., *Physics with a ground-based gamma-ray telescope of low energy threshold*, (2005), In preparation.

[2] A. Ostankov et al., *A study of the new hemispherical 6-dynodes PMT from electron tubes*, Nucl. Instrum. Meth. **A442** (2000) 117.

[3] E. Lorenz et al., *A fast, large dynamic range analog signal transfer system based on optical fibers*, Nucl. Instrum. Meth. **A461** (2001) 517.

[4] J. Cortina et al. (MAGIC Collab.), *The data acquisition of the MAGIC telescope*, Prepared for International Symposium: The Universe Viewed in Gamma Rays, Kashiwa, Chiba, Japan, 25-28 Sep 2002.

[5] J. A. Barrio, et al. (MAGIC Collab.), *The MAGIC Telescope – Design Study for the Construction of a 17 m Cherenkov Telescope for Gamma Astronomy above 10 GeV*, (1998), MPI-PhE 98-05.

[6] M. Gaug et al., *TDAS Analysis of The Calibration Data*, 2005, in progress.

[7] O. Blanch and A. Moralejo, *TDAS 0407 How to use the Camera simulation program 0.7*, 2004.

[8] T. Schweizer et al., *The optical calibration of the MAGIC telescope camera*, IEEE Trans. Nucl. Sci. **49** (2002) 2497.

[9] V. R. Chitnis and P. N. Bhat, *Possible discrimination between gamma rays and hadrons using Čerenkov photon timing measurements*, Astroparticle Physics **15** (2001) 29.

[10] T. Bretz and R. Wagner (MAGIC Collab.), *The MAGIC analysis and reconstruction software*, Proceedings of the 28^{th} ICRC, Tsukuba, Japan (2003).

[11] W.H.Press et al., *Numerical Recipes in C++*, Cambridge University Press, second edition, 2002.

[12] W. E. Cleland and E. G. Stern, *Signal processing considerations for liquid ionization calorimeters in a high rate environment*, Nucl. Instrum. Meth. **A338** (1994) 467.

[13] A. Papoulis, *Signal analysis*, McGraw-Hill, 1977.

[14] H. Bartko et al., *TDAS 0501 Prototype Tests of a Multiplexed Fiber-Optic Ultra Fast FADC Data Acquisition System for the MAGIC Telescope*, 2005.

[15] M. Shayduk, *Signal Extractors Comparison*, http://magic.physik.hu-berlin.de/protected/Results/ExtractorComp/index.html.

[16] M. Gaug, *TDAS0406 The Calibration System Hardware Manual*, 2004.

[17] M. Doro, *The Commissionning and Characterization of the Calibration System of the MAGIC Telescope*, Diploma thesis, Universitá di Padova, 2004, http://wwwmagic.mppmu.mpg.de/publications/theses/LaureaMDoro.ps.gz.

[18] D. Paneque, *The MAGIC Telescope: Development of new technologies and first observations*, PhD thesis, Technische Universität München, 2004, http://wwwmagic.mppmu.mpg.de/publications/theses/David_thesis.ps.gz.

[19] F. Goebel, private communication.